Ion Photon Entanglement with Barium

Thomas William Noel

A dissertation
submitted in partial fulfillment of the
requirements for the degree of

Doctor of Philosophy

University of Washington

2014

Reading Committee:

Boris Blinov, Chair

Subhadeep Gupta

Xiaodong Xu

Program Authorized to Offer Degree:
Department of Physics

University of Washington

Abstract

Ion Photon Entanglement with Barium

Thomas William Noel

Chair of the Supervisory Committee:
Associate Professor Boris Blinov
Department of Physics

Entanglement between a single trapped $^{138}\mathrm{Ba}^+$ and a single spontaneously emitted photon is demonstrated. The system is used to measure a CHSH Bell signal of 2.303(36), verifying the violation of the CHSH inequality by over eight standard deviations. The feasibility of using the system to perform a loophole free measurement of the violation of the Bell inequality is considered.

A pair of side projects are discussed. First, the robustness of ARP in the presence of noise in the driving field is investigated. And second, a ppm measurement of the Landé g factor of the $5D_{5/2}$ level of $^{138}\mathrm{Ba}^+$ is reported. The new ion trap that made all this work possible is introduced.

TABLE OF CONTENTS

LIST OF FIGURES

Figure Number Page

LIST OF TABLES

Table Number Page

ABBREVIATIONS

AOM Acousto-Optic Modulator. A device that uses Bragg scattering of light off of sound waves in a crystal to redirect and frequency shift laser beams.

APD Avalanche Photodiode. A photodiode in which a single photon causes avalanche breakdown of the diode resulting in a large current. APDs can achieve higher quantum efficiency than photon counting PMTs, but often suffer from higher dark count rates.

ARP Adiabatic Rapid Passage. A process wherein population is transferred between states of a system by introducing and adiabatically varying a Hamiltonian that couples the states.

CCD Charge Coupled Device. Type of camera that uses an array of photosensitive pixels and shift register pixel readout to capture images.

DDS Direct Digital Synthesizer. Sythesizer for creating arbitrary programmed waveforms using a single fixed frequency clock input and a digital to analog converter.

ECDL External Cavity Diode Laser. Adding an additional cavity external to the bare diode laser cavity will greatly reduce the laser linewidth. Often the cavity is formed from a diffraction order of a diffraction grating in order to provide coarse frequency tunability.

EMCCD Electron Multiplying CCD. CCD in which charges produced by light are amplified before being read out.

PDH Pound-Drever-Hall. Technique for locking a laser to a cavity, in which the laser is phase modulated and the signal reflected off of the cavity is monitored.

PMT	Photomultiplier Tube. A device that transduces light into an electrical signal. Uses the photo-electric effect to produce a free electron which in turn produces a cascade of many electrons after a series of accelerations into secondary dynode electrodes.
PPLN	Periodically Poled Lithium Niobate. A device used for SHG in which the orientation of a lithium niobate crystal is periodically flipped over the device length. When the poling period matches the second harmonic wavelength the newly created second harmonic light largely constructively interferes with the field that is already present and the intensity of the second harmonic will increase over the entire length of the device.
rf	radiofrequency. The part of the electromagnetic spectrum from (very roughly, sources differ) 1 kHz to 100 GHz. Here it will be used to refer to frequencies from 1 MHz to 1 GHz.
SHG	Second Harmonic Generation. Generation of radiation at twice the frequency of the input.
TEC	Thermo-Electric Cooler. A device that uses the Peltier effect to produce a temperature gradient. Used as the feedback element in temperature control servo loops.
VCO	Voltage Controlled Oscillator. A device which converts voltage to frequency, that is, the device produces a sinusoidal output with frequency depending (usually linearly) on an input dc voltage.

ACKNOWLEDGMENTS

First off, I would like to thank Professor Boris Blinov for being a great advisor. He claims we kicked him out of the lab, but he was always available when I needed him and was willing to give me plenty of space when I thought I didn't. Thanks also to Professors Deep Gupta and Xiaodong Xu, the other members of my dissertation reading committee, for being willing to read the mess that follows.

The physics department staff also deserve many thanks. In particular, the help of Hans Berns and Eric Lindahl in making printed circuit boards was invaluable, and Peter Hirtle of the UW Instrument Shop did all the difficult machining of the X-trap components.

I am greatly indebted to the quartet of graduate students who graduated shortly after I joined Boris's group. Without their hard work and the knowledge they passed on my accomplishments would have been impossible, so thank you to Matthew Dietrich, Adam Kleczewski, Nathan Kurz, and Gang "Rick" Shu. A troup of undergraduate students provided me equally with useful pieces of apparatus and opportunities to learn about teaching. I would particularly like to thank Andrea Katz, Shaw-Pin "Bing" Chen, Eric Josberger, Rebecca Schutzengel, Sean Nelson, Morgan Catha, and Matthew Bohman for their assistance.

Without the support and camaraderie of my labmates the last five years would have been much less enjoyable. Thank you to Carolyn Auchter, Chen-Kuan Chou, Tomasz Sakrejda, Spencer Williams and especially to Matthew Hoffman and John Wright as much for keeping life interesting and fun as for their indispensable help and mutual struggle in the lab.

I am enormously thankful to my parents for their guidance and their enduring confidence in me. Thanks to my big brother Jeff for never-ending science discussions of topics about which we usually knew almost nothing and again to our parents for putting up with us.

Finally, but foremost, thank you to my wife, Megan, for always being there for me.

Part I

THEORETICAL PRELIMINARIES

Chapter 1

ATOMIC PHYSICS

Broadly speaking, atomic theory seeks to answer three inter-related questions. First, how is the energy level structure of a bare atom determined? Second, how do atoms interact with external fields? And lastly, what are the interactions between atoms? In ion traps the final question has a straightforward answer, the dominant interaction between ions in the trap is Coulomb repulsion, which is strong enough that the motional states of all the ions in the trap are strongly coupled. This shared motional state forms the basis of most entangling gates for ions in the same trap. There is some interest in the study of the coupled motion of ions in traps for more fundamental reasons [16, 21, 41, 59], but this is far afield from the topic of this work so I will leave the discussion of direct ion-ion interactions at that.

1.1 Atomic Structure

Books discussing atomic structure abound [17, 18, 24, 45, 60], but I think there remains some utility in sketching here the important features as they relate to our species of interest, singly ionized barium. Singly ionized barium has only a single valence electron, so the story of its atomic structure is largely written by the properties of this electron alone. The spherically symmetric potential the valence electron finds itself in naturally gives rise to a decomposition of the Schrödinger equation into radial and angular parts. The radial part yields a set of wavefunctions labelled, in part, by the principal quantum number, n. In Ba^+, the difference in energy of the ground state, with $n = 6$, and the next principal quantum number, $n = 7$, is 236 nm or 1270 THz. If the atom truly had only a single electron, then, as in hydrogen, for a given principal quantum number the different angular momentum states of the electron would be degenerate. This results from the fact that, although the radial probability distributions differ for different angular momentum states, the expectation value of 1/r only depends on the principal quantum number. This is perhaps reasonable, though not obvious, from the plots of the radial wavefunction amplitude shown in the right plot of Fig. 1.1. However, in the presence of the inner shell electrons, the different radial

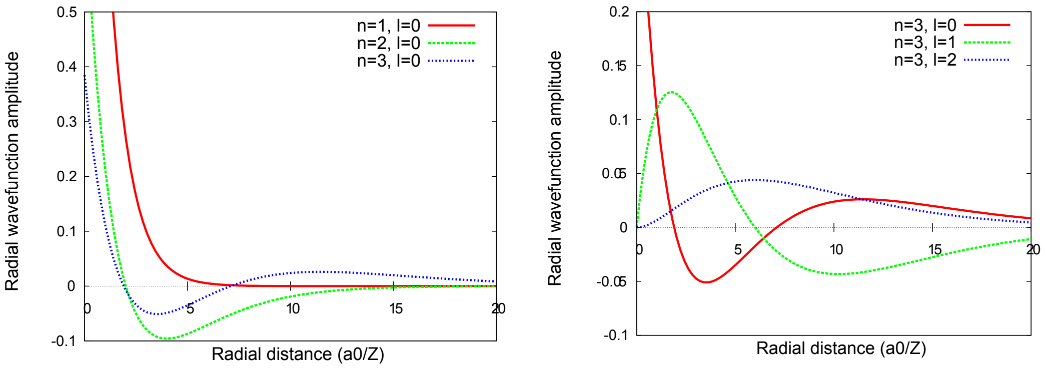

Figure 1.1: Hydrogenic radial wavefunctions. The first plot shows the first three radial wavefunctions without angular momentum, note that the average distance from the origin (and therefore the energy of the state) increases with principal quantum number, n. The second plot shows the three radial wavefunctions for $n = 3$. All have the same average value of $1/r$ and, therefore, the same energy.

probability distributions associated with different angular momentum states are screened from the nuclear charge differently resulting in energy splittings between states of the same principal quantum number but different orbital angular momenta. In Ba$^+$, this results in a splitting between the $n = 6$, $l = 0$ ground state and the $n = 6$, $l = 1$ state of roughly 630 THz. Also of great importance, as we will see later, this effect pushes the $n = 5$, $l = 2$ states above the energy of the ground state.

As yet we have made no mention of the fact that the valence electron has a spin and furthermore we have been considering wavefunctions resulting from a Schrödinger equation (non-relativistic) formalism. The next effects to mention, collectively known as “fine structure,” begin to address these details. With the provincial mindset that effects causing energy splittings are more interesting than effects causing uniform shifts of whole levels, I will highlight the spin-orbit contribution to fine structure and leave the “Darwin” and relativistic mass shifts by the wayside. Since the valence electron is moving in the presence of a non-uniform electric field, in its rest frame it will experience a magnetic field. It turns out that (since the electric field points radially on average) this magnetic field is proportional to the electron's orbital angular momentum, $\vec{l}$. Spin-orbit coupling arises from the interaction of the electron spin with this magnetic field, and its Hamiltonian has the form $H_{\mathrm{s-o}} = \alpha\vec{l}\cdot\vec{s}$. This produces a splitting between states with different values of the total valence electron angular momentum, $\vec{j} = \vec{l} + \vec{s}$. Perhaps now is a convenient time to introduce an energy level labelling notation that will be used throughout this work. The labelling tool is called the term symbol and looks like $n^{2s+1}L_j$, where n is the atomic state's principal quantum number, s its spin, L its orbital angular momentum, and j its total electronic angular momentum. In atoms with a single valence electron, like Ba$^+$, typically the $2s+1$ is dropped since $s = 1/2$ always. With this notation in hand, let's examine the numerical values of some fine structure splittings in Ba$^+$. The $5D_{5/2}$ level resides 24 THz above the $5D_{3/2}$ level and $6P_{3/2}$ resides 51 THz above $6P_{1/2}$. Finally, if the atom under consideration has nuclear spin, $I \neq 0$, then the coupling between the total electronic angular momentum and the nuclear spin splits the energies of "hyperfine" levels with different total atomic angular momentum $\vec{F} = \vec{I} + \vec{j}$. The Ba$^+$ isotope used in this work is ^{138}Ba$^+$ which has no nuclear spin and therefore no hyperfine structure. Another abundant isotope of barium is ^{137}Ba$^+$, which has $I = 3/2$ resulting in a ground state hyperfine splitting of 8.037 GHz [19, 7]. A summary of the structure of Ba$^+$ is presented in Fig. 1.1. [33]

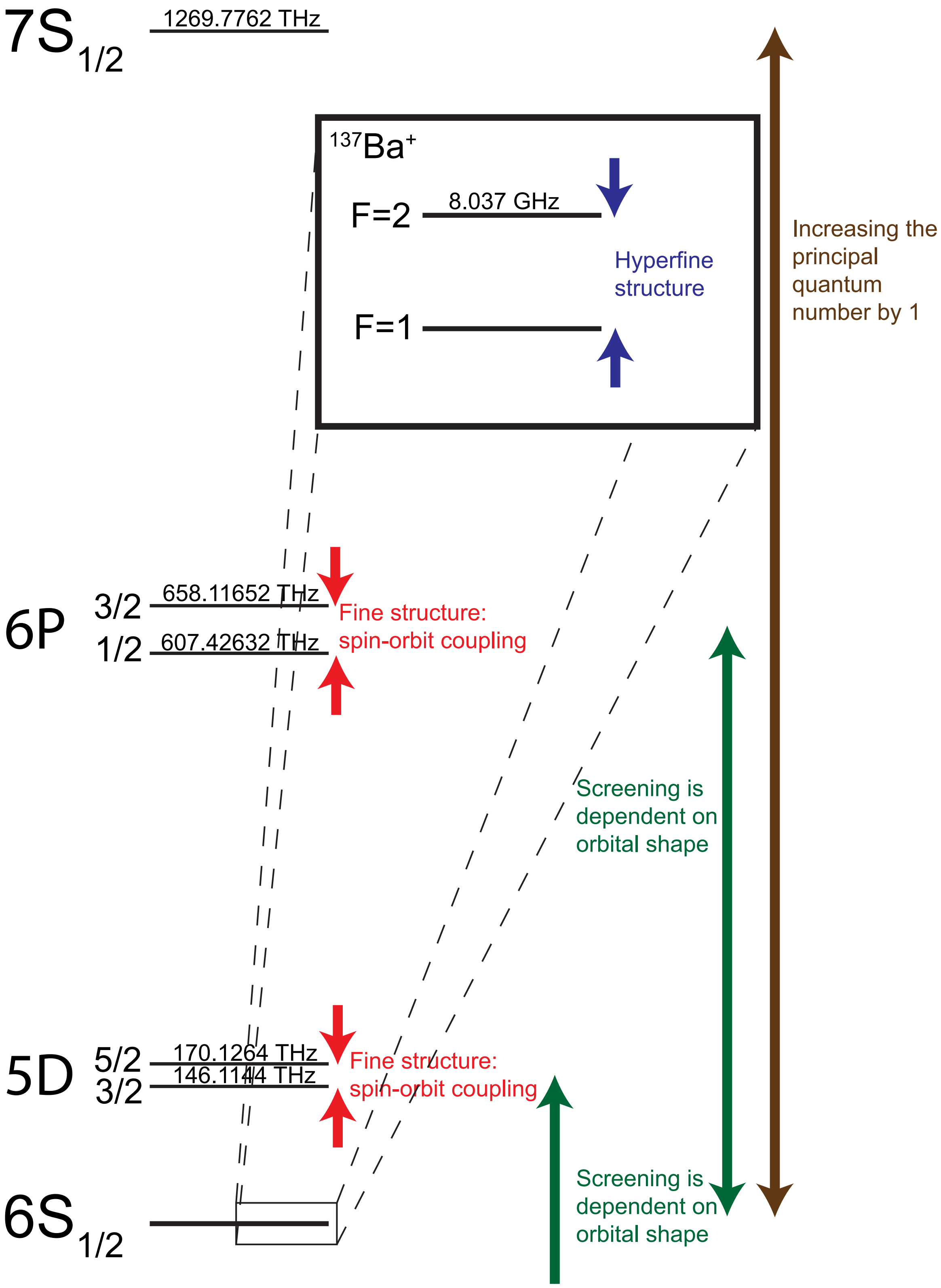

Figure 1.2: Summary of atomic structure of Ba^{+}. Figure is to scale, hyperfine structure inset is expanded by a factor of 5×10^{5}.

1.2 Interaction with a static magnetic field

The discussion of the interaction of atomic systems with external electromagnetic fields can be separated into consideration of static and oscillating fields. Static fields will perturb the energy levels of the atomic system and oscillating fields will both perturb the energy levels and drive atomic transitions. First let us consider the case of a static magnetic field.

In the absence of a magnetic field, any given atomic energy level consists of a set of $2j+1$ degenerate states, where j is the total angular momentum of the level. The magnetic moment of the atomic state is $\vec{\mu} = g_j \mu_B \vec{j}$, where g_j is the Landé g factor and μ_B is the Bohr magneton. This magnetic moment experiences the Hamiltonian $H = -\vec{\mu} \cdot \vec{B}$ in the presence of a magnetic field $\vec{B}$. Thus, in a magnetic field these states split according to the value of the projection of their angular momentum on to the direction of the field. Since I will spend a chapter describing my efforts to measure the Landé g factor of the $5D_{5/2}$ level of $^{138}\mathrm{Ba}^+$ later in this manuscript, I will spend a short time here describing the simple theory one would use to calculate a g factor. We will approach this by looking at the magnetic moment as I wrote it above and also as a sum of the magnetic moments due to the electron spin and orbital angular momentum separately (and if there were nuclear spin one would treat it analogously with the caveat that the nuclear magneton must be used rather than the Bohr magneton).

$$\langle H \rangle = \left\langle -g_j \mu_B \vec{j} \cdot \vec{B} \right\rangle = \left\langle -\mu_B (g_l \vec{l} + g_s \vec{s}) \cdot \vec{B} \right\rangle , \tag{1.1}$$

where g_l and g_s are the g factors associated with the electron's orbital and spin angular momentum, respectively. The left hand equation reduces simply (since m_j is a good quantum number, while m_l and m_s are not) to $-g_j \mu_B |\vec{B}| m_j$. The right hand side benefits from use of the Landé projection theorem:

$$\left\langle \alpha', j m_j' \right| v_q \left| \alpha, j m_j \right\rangle = \frac{\left\langle \alpha', j m_j' \middle| \vec{j} \cdot \vec{v} \middle| \alpha j m_j \right\rangle}{\hbar^2 j(j+1)} \left\langle \alpha', j m_j' \right| j_q \left| \alpha, j m_j \right\rangle , \tag{1.2}$$

where α' and α refer to a set of additional quantum numbers fully labeling the atomic states and v_q is the q^{th} spherical component of the vector operator $\vec{v}$. With the fact that $\vec{j} = \vec{l} + \vec{s}$

implying that $\vec{j}\cdot\vec{l} = (\vec{j}^2 + \vec{l}^2 - \vec{s}^2)/2$, we apply Eq. 1.2 with $v_q = l_z$ and find that

$$\langle l_z \rangle = \frac{\left\langle \vec{j}^2 + \vec{l}^2 - \vec{s}^2 \right\rangle}{2\hbar^2 j(j+1)} m_j. \tag{1.3}$$

Using this result we can rewrite the right hand side of Eq. 1.1 to be

$$-\frac{\mu_B \left|\vec{B}\right| m_j}{2j(j+1)} \left[g_l \Big(j(j+1) + l(l+1) - s(s+1) \Big) + g_s \Big(j(j+1) + s(s+1) - l(l+1) \Big) \right]. \tag{1.4}$$

Now we compare the two sides of Eq. 1.1, noting that $s = 1/2$, and read off that

$$g_j = \frac{1}{2j(j+1)} \left[g_l \Big(j(j+1) + l(l+1) - 3/4 \Big) + g_s \Big(j(j+1) - l(l+1) + 3/4 \Big) \right]. \tag{1.5}$$

Using $g_l = 1$, $g_s = 2$, and simplifying, we find the Landé formula the g factor:

$$g_j = 1 \pm \frac{1}{2l+1}, \tag{1.6}$$

for $j = l \pm 1/2$. Applying this formula to the $5D$ fine structure levels of $^{138}\mathrm{Ba}^+$, we find that the $5D_{5/2}$ and $5D_{3/2}$ levels have g factors of 1.2 and .8, respectively. And if we use the somewhat more accurate free electron g factor, $g_e = 2.002319...$[29], for g_s (this still ignores QED corrections regarding the non-vacuum environment of the valence electron) we find g factors of 1.200464... and .799536..., respectively. This gives a value that is quite close to the experimentally determined value described later in this manuscript, which is (spoiler alert), $g_{D_{5/2}} = 1.200371(4_{\mathrm{stat}})(6_{\mathrm{sys}})$ [31].

1.3 Interaction with oscillating external fields

In this work we are interested primarily in interactions that couple only two states at a time so we can restrict our attention to wavefunctions of the form

$$\Psi(t) = C_1(t)e^{-i\zeta_1(t)}\psi_1 + C_2(t)e^{-i\zeta_2(t)}\psi_2 \tag{1.7}$$

where the ψ_n are eigenfunctions of the bare atom Hamiltonian, H_0, satisfying $H_0\psi_n = \hbar\omega_n^0\psi_n$ and are assumed to be known. The energy of the bare atomic state, ψ_n, is given by $\hbar\omega_n^0$. Additionally, in Eq. 1.7 we have anticipated the usefulness of attaching phases, ζ_n, to the eigenfunctions. Note, however, that this is NOT assuming that the resulting probability amplitudes, C_n, are real. Rather, the choice of the ζ_n corresponds to a choice of the "picture" in which to view the dynamics. Taking the simplest choice, $\zeta_1 = \zeta_2 = 0$ defines the Schrödinger picture in which all the time dependence is contained in the probability amplitudes. The Dirac picture incorporates the dynamic phase associated with the unperturbed state energies into the ζ_n by choosing $\hbar\dot{\zeta}_n = \hbar\omega_n^0$. Shortly we will make a third choice where the ζ_n additionally capture part of the interaction dynamics.

We are interested in describing the dynamics resulting from the application of nearly resonant electric and magnetic fields, and so the Hamiltonians of interest will look something like

$$H(t) = H_0 + V(t) = \begin{bmatrix} \hbar\omega_1^0 & V_{12}(t) \\ V_{21}(t) & \hbar\omega_2^0 \end{bmatrix}, \tag{1.8}$$

where $V_{21}(t) = V_{12}^*(t)$ by Hermiticity, $V_{21}(t) = \frac{1}{2}\hbar\Omega e^{-i\omega t - i\phi}$ for the interactions of interest[1], and ω and ϕ are the frequency and phase of the driving field, respectively. The Rabi frequency, Ω, contains the details of the particular type of interaction that is being studied (electric dipole, magnetic dipole, electric quadrupole, etc.) and its calculation may be of considerable interest, however here we will assume it to be known in order to pursue the resulting dynamics. Plugging Eq. 1.7 and Eq. 1.8 into the Schrödinger equation, we find

$$i\frac{d}{dt}\begin{bmatrix} C_1(t) \\ C_2(t) \end{bmatrix} = \begin{bmatrix} \omega_1^0 - \dot{\zeta}_1(t) & \frac{1}{2}\Omega e^{-i(\zeta_2(t)-\zeta_1(t)-\omega t-\phi)} \\ \frac{1}{2}\Omega e^{i(\zeta_2(t)-\zeta_1(t)-\omega t-\phi)} & \hbar\omega_2^0 - \hbar\dot{\zeta}_2(t) \end{bmatrix} \begin{bmatrix} C_1(t) \\ C_2(t) \end{bmatrix}. \tag{1.9}$$

Now we will use our freedom in choosing the ζ_n to simplify the situation. In this case we can remove all the explicit time dependence from the equation by choosing

$$\begin{aligned} \zeta_1(t) &= \tfrac{1}{2}(\omega_1^0 + \omega_2^0 - \omega)t \\ \zeta_2(t) &= \tfrac{1}{2}(\omega_1^0 + \omega_2^0 + \omega)t + \phi. \end{aligned} \tag{1.10}$$

This simplifies Eq. 1.9 to

$$i\frac{d}{dt}\begin{bmatrix} C_1(t) \\ C_2(t) \end{bmatrix} = \frac{1}{2}\begin{bmatrix} -\delta & \Omega \\ \Omega & \delta \end{bmatrix} \begin{bmatrix} C_1(t) \\ C_2(t) \end{bmatrix}, \tag{1.11}$$

---

[1] This is the simplest case to consider analytically, but often a real oscillating potential, $V_{21}(t) \propto \cos(\omega t + \phi)$, is more appropriate. In this case, break the cosine into its complex exponential components, proceed as in the main text, and see the next footnote.

where[2] we have introduced the detuning, $\delta = (\omega_2^0 - \omega_1^0) - \omega$. This coupled set of first order differential equations can be easily solved by conversion into a pair of second order uncoupled differential equations. Given the initial condition that the atom is in the ground state, $C_1(0) = 1$ and $C_2(0) = 0$, we find the solution for the excited state population to be the familiar phenomenon of Rabi oscillation,

$$P_2(t) = |C_2(t)|^2 = (\frac{\Omega}{W})^2 \sin^2(Wt/2), \tag{1.12}$$

where the generalized Rabi frequency is given by $W = \sqrt{\Omega^2 + \delta^2}$. Note that the maximum population transfer is limited to $(\Omega/W)^2$ and so efficient transfer requires that the driving field be resonant with the atomic transition. When the driving field is off-resonant, the amplitude of the population oscillation diminishes while the frequency is enhanced. This behavior is shown for a few values of δ in Fig. 1.3. For a resonant driving field, the shortest time for which all population has been transferred to the excited state is called the π-time, $T_\pi = \pi/\Omega$. This term will arise frequently in the discussions of later chapters.

If we consider the same situation in a density matrix formulation we can derive a convenient packaging of Eq. 1.9 that is commonly referred to as the optical Bloch equations. Since we are considering a pure two-state system the density matrix can be written as

$$\rho = \begin{bmatrix} \rho_{11} & \rho_{12} \\ \rho_{21} & \rho_{22} \end{bmatrix} = \begin{bmatrix} |C_1|^2 & C_1 C_2^* \\ C_2 C_1^* & |C_2|^2 \end{bmatrix}. \tag{1.13}$$

After making a change of variables to the Bloch variables $u = \rho_{12} + \rho_{21}$, $v = (\rho_{12} - \rho_{21})/i$, and $w = \rho_{22} - \rho_{11}$ we can derive a new set of coupled differential equations for these variables using Eq. 1.9.

$$\begin{aligned} \dot{u} &= -\delta v \\ \dot{v} &= -\Omega w + \delta u \\ \dot{w} &= \Omega v \end{aligned} \tag{1.14}$$

---

[2] In the case of a real oscillating potential, at this point you should have the same equation given the replacement $\Omega \rightarrow \Omega(1 + e^{2i\omega t + 2i\phi})$ (and similarly for the complex conjugate of Ω) Now one would note that the behavior of interest happens at a much lower frequency than ω, and so integrates the equation over a period of the driving field oscillation. The “rotating-wave approximation” then states that the C_n do not change appreciably over this time interval and so can be taken out of the integration. Taking this approximation simplifies the situation to exactly that in the main text.

If we use the Bloch variables to define a Bloch vector, $\vec{R} = u\hat{x} + v\hat{y} + w\hat{z}$, and define an interaction vector, $\vec{W} = \Omega\hat{x} + \delta\hat{z}$, then we can further package the optical Bloch equations into a vector form:

$$\dot{\vec{R}} = \vec{W} \times \vec{R}. \tag{1.15}$$

Eq. 1.15 describes precessional motion of the unit vector $\vec{R}$ about the interaction vector. This is the motivation for the celebrated Bloch sphere representation of the dynamics of two-state systems, which finds extensive application in the field of quantum information. In addition to providing a convenient visualization tool, the optical Bloch equation route also yields a simple avenue to including damping due to the finite lifetime of the excited state. Rather than going to any lengths to justify the incorporation of the excited state lifetime into the optical Bloch equations, we treat the following as an intuitively plausible model

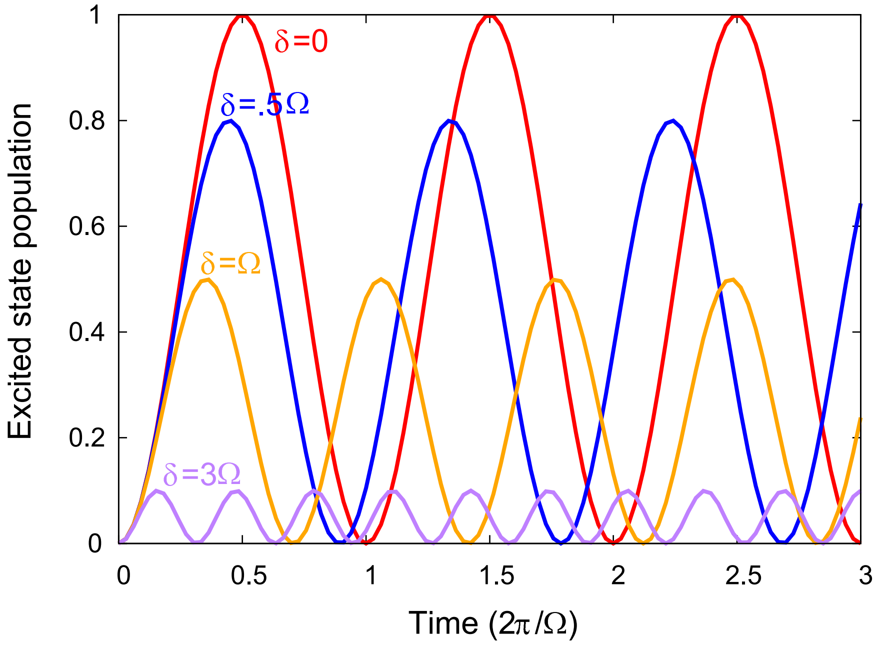

Figure 1.3: Rabi oscillation for a few values of the detuning, δ. As the detuning increases, the amplitude of the population oscillations decreases, but the oscillation frequency increases. If one wishes to do highly efficienct population transfer using constant frequency excitation one must stabilize the frequency and intensity of the driving field.

that is empirically verified.

$$\begin{aligned}\dot{u} &= -\delta v - \tfrac{\Gamma}{2}u \\ \dot{v} &= -\Omega w + \delta u - \tfrac{\Gamma}{2}v \\ \dot{w} &= \Omega v - \Gamma(w+1),\end{aligned} \tag{1.16}$$

where $\Gamma = 1/\tau$ and τ is the excited state lifetime. The useful consequence of these equations for the discussions to follow is to consider the behavior at times long compared to both $1/\Omega$ and $1/\Gamma$. Given a constant excitation and the presence of dissipation, we expect that at such long times the populations will have reached a steady state. We can solve for this steady state behavior by setting $\dot{u} = \dot{v} = \dot{w} = 0$. In this case we find the excited state population to be,

$$\rho_{22} = \frac{1+w}{2} = \frac{1}{2}\frac{\Omega^2/2}{\delta^2 + \Omega^2/2 + \Gamma^2/4}. \tag{1.17}$$

This implies the intuitively sensible result that in the presence of a very strong excitation ($\Omega \to \infty$) the steady state population of the excited and ground states will equalize at 1/2. This equation will also form the basis of the discussion of the scattering force and its relation to Doppler cooling in the following chapter.

The intention of this section was to introduce the behavior of atomic systems that we will make use of in later chapters. The discussion of Doppler cooling in Chapter 2 will make use of the results from the dissipative optical Bloch equations. The idea of Rabi oscillation will come up again and again throughout this work, as we make use of coherent excitation on a variety of transitions. Finally, the Bloch sphere representation of two-state dynamics will be a useful visualization tool to keep in mind as we go forward.

Chapter 2

RELEVANT TECHNIQUES

2.1 Ion Trapping

Ion traps come in two major varieties, the Penning trap and the Paul trap[1]. Each type attempts to solve the problem of stably localizing charged particles in free space. Naïvely one might expect that a charge could be localized using static electric fields alone, but inspection of Maxwell's equations in free space with static fields shows that this is not the case.

$$\Delta V = \frac{\partial^2 V}{\partial x^2} + \frac{\partial^2 V}{\partial y^2} + \frac{\partial^2 V}{\partial z^2} = 0 \tag{2.1}$$

A trapping potential (for a positive charge) would have positive curvature in every direction, ensuring that a particle with sufficiently low energy could not escape. However, the static Maxwell's equations demand that the sum of the curvatures of the potential in three orthogonal directions must vanish at every point in free space and so no such trapping potential can be formed. The "best" one might do with static potentials is to make a saddle surface with two positive curvature directions, but the charge will still be able to escape along the third direction. To solve this problem the Penning and Paul approaches follow different avenues. The Penning trap introduces a static magnetic field while the Paul trap allows the electric fields to oscillate. Since Paul traps are the solution we employ, I will only say a few words about Penning traps before moving on. Penning traps have a strong homogenous magnetic field along the axis of their cylindrical symmetry. The magnetic field provides localization in the radial direction via the Lorentz force. Trapping along the axis is provided by a static electric field generated by applying a dc voltage to a pair of endcap

---

[1] There is a third variety called the EBIT (electron beam ion trap). It is used to produce and trap highly charged ions. This is accomplished by employing an electron beam with extremely high current density both for ionization and to produce the radial trapping potential. Much interesting work can be done using EBITs so it is perhaps unfair to resign them to a footnote, however I choose to focus on traps that have long lifetimes here.

electrodes (or to tighten the dc quadrupole the voltage may be applied between a pair of endcaps and a central ring electrode). A schematic of such a trap is shown in Fig. 2.1 taken from an early review of Penning trap physics[10]. Both positive and negative charges with a wide range of masses can be easily trapped in a Penning trap simply by varying the size and polarity of the potential applied to the endcaps. This gives Penning traps the advantage of doing simple co-magnetometry by measuring the frequency of the cyclotron motion of trapped electrons. Thus all the most precise absolute measurements of atomic g-factors have been done in Penning traps [34, 35]. In addition to precision measurement, Penning traps are increasingly being considered for use in analog quantum simulation, since two- and three-dimensional ion crystals are ideal test-beds for Ising-type and other Hamiltonians [9, 54, 6].

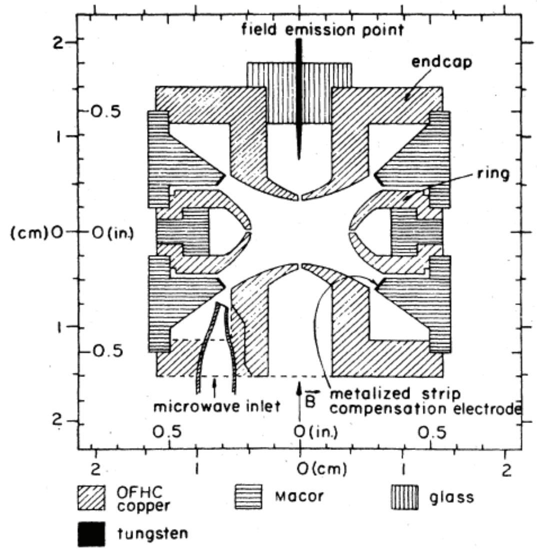

Figure 2.1: Penning trap cross-section. A tungsten electrode provides a source of electrons to be trapped. A dc voltage is applied between the endcap and central ring electrodes confining the electrons along the axis of the trap. A large magnetic field along the axis provides radial confinement.

2.2 *Paul traps*

Unlike the Penning trap, the Paul trap doesn't use a magnetic field as part of the trapping solution. Instead, a quadrupole electric potential configuration is allowed to oscillate at radio-frequency. Ideally, the electrodes used to create any potential configuration should be equipotential surfaces of the potential they intend to produce, and since the equipotentials of a quadrupole potential are hyperboloids the electrodes in a Paul trap would ideally be hyperbolic. However, it was quickly realized that the effort spent machining hyperbolic electrodes was wasted, since a variety of simpler electrode configurations will produce a dominantly quadrupolar potential. Thus even by the time that Dehmelt trapped the first single barium ion in 1980, they were using electrodes like those seen in Fig 2.2, which was borrowed from [48]. The variety of Paul trap that I have employed is called a linear Paul trap, and an archetypical example can be seen in Fig. 2.3, from [64]. The advantage of this design is that the null of the oscillating potential is extended in one dimension, instead of being confined to a single point as was the case in traps like those in Fig. 2.2. This allows a linear string of ions to be trapped on the rf null, which, we will see, is a necessary condition for minimizing motion driven at the rf trap frequency.

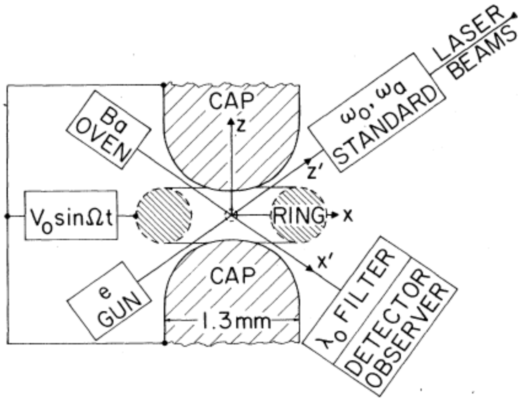

Figure 2.2: Schematic of the ion trap Dehmelt first used to trap barium ions. The central electrode is a torus and the endcaps are hemispheres. An rf oscillating potential is applied between the torus and endcaps.

Before we delve into the mathematical treatment of Paul traps, let's briefly gather some

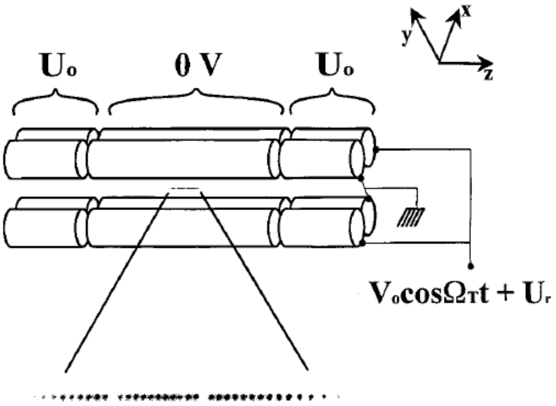

Figure 2.3: Linear Paul trap. An rf potential is applied to diagonally opposite rods, while the remaining rods are at rf ground. Each rod is segmented into three parts which are capacitively coupled so that they are connected at rf but open at dc. A dc potential is applied to each end of all four rods to provide confinement along the symmetry axis of the trap. An image of a linear string of ions is shown along the trap axis, note that the gaps between visible ions show that some “dark” ions have also been trapped.

intuition about the kind of behavior to expect. Consider the motion of a particle sliding on a frictionless saddle surface in the presence of gravity. On a static saddle, the particle will begin to accelerate down the maximum local gradient and will quickly make it very far away from the saddle center. Clearly, this is not a stable trap. To construct an analog for the Paul trap, we allow this saddle surface to “flap,” that is, allow the curvature along one direction to vary sinusoidally while the curvature along the orthogonal direction oscillates perfectly out of phase. On such a flapping saddle, before the particle slides very far away from the saddle center, the local gradient reverses, pushing the particle back toward the center. Furthermore, since the force the particle feels is proportional to its acceleration, the particle’s position lags behind its acceleration[2] (ideally by half a period) and so is farther from the trap center when the local gradient points back toward the trap center and is closer to the trap center when the gradient points away. Combined with the fact that the gradient increases in magnitude away from the trap center, this means that the particle feels a larger force back

---

[2] This is because position is two integrations away from acceleration and integrating a sinusoid twice yields the same sinusoid back, but 180 degrees out of phase. This argument uses the fact that the component of the particle motion driven directly by the oscillating potential will be at least roughly sinusoidal.

toward the center than the force it feels pushing it away. Thus we get a net, time-averaged restoring force and, therefore, a trap. This intuitive picture is a nearly faithful analogy for the forces a charged particle feels in a (2-dimensional) oscillating quadrupole electric field. Inspecting this intuitive analysis closely yields all the major features we will find from the mathematical treatment to follow. First there must be some driven motion at the "flapping" frequency, which we refer to as "micromotion." Second, since the driven motion results in a time-averaged restoring force, there must be some lower frequency oscillation about the trap center, which we will refer to as "secular" motion. Admittedly more tenuously, third, we might expect that there should be only some region in the relevant parameter space that will truly form a stable trap (since we saw that a static saddle did not form a stable trap). With this intuition in tow, let's take a look at a mathematical model for the Paul trap.

In a linear Paul trap, like that seen in Fig. 2.3, near the trap center the electric potential will have the form

$$\Phi_{rf}(x,y,z,t) = \alpha V_0 \cos \Omega_{\mathrm{rf}} t \left(\frac{x^2 - y^2}{2R_0^2} \right), \tag{2.2}$$

where V_0 is the amplitude and Ω_{rf} is the frequency of the rf voltage applied to the rods, R_0 is the minimum distance from the trap center to the rods, and α is a factor that accounts for the fact that the rod electrodes are not quadrupolar equipotential surfaces and other geometric properties [64]. The coordinate axes are defined like those in Fig. 2.3, with the z axis along the symmetry axis of the trap and the x and y axes through the center of the rods. Due to the dc potential applied to the end segments of the rods there is an additional electric potential, which, near the trap center, has the form

$$\Phi_{dc}(x,y,z) = \kappa U_0 \left(\frac{2z^2 - (x^2 + y^2)}{2z_0^2} \right), \tag{2.3}$$

where U_0 is the applied dc voltage, z_0 is the minimum projected distance along the z axis from the trap center to the dc electrodes, and κ is a geometric factor. Since both α and κ depend on the particular geometry of the trap (i.e. they depend on the diameter of the rods and the values of R_0 and z_0) our ability to use the discussion to follow to extract meaningful trap parameters (e.g. secular frequencies) from the known trap properties and the equations we will derive is somewhat limited. In practice to have confidence in predictions of trap parameters it is probably best to perform FEM since detailed analytical modeling of accurate trap geometries is difficult. That said, both α and κ are reportedly often on the order of one for typical trap geometries [56], however, applying the equation for the axial trap frequency to my trap implies that $\kappa_{\mathrm{x-trap}} \approx .02$ and FEM of a four rod trap with dc applied to washers encircling the rods implies an even smaller κ value[3]. With these caveats in mind, let us press on. The force the ion feels in the presence of the rf and dc potentials is given by $\vec{F} = -e\boldsymbol{\nabla}\Phi$ where e is the ion charge and $\Phi = \Phi_{rf} + \Phi_{dc}$. This breaks up nicely to give uncoupled equations of motion along the three directions.

$$\begin{aligned} \ddot{x} &= \Big(-\frac{e\alpha V_0 \cos\Omega_{\mathrm{rf}} t}{mR_0^2} + \frac{e\kappa U_0}{mz_0^2}\Big) x \\ \ddot{y} &= \Big(\frac{e\alpha V_0 \cos\Omega_{\mathrm{rf}} t}{mR_0^2} + \frac{e\kappa U_0}{mz_0^2}\Big) y \\ \ddot{z} &= -\frac{e\kappa U_0}{mz_0^2} z \end{aligned} \tag{2.4}$$

The z equation yields simple harmonic motion with frequency $\omega_z = (2e\kappa U_0/mz_0^2)^{1/2}$, where m is the mass of the ion. To solve for the transverse motion, we rescale the time variable to $\tau = \Omega_{\mathrm{rf}} t/2$, yielding the equations

$$\begin{aligned} \frac{d^2x}{d\tau^2} &= \Big(2q_x \cos 2\tau - a_x\Big) x \\ \frac{d^2y}{d\tau^2} &= \Big(2q_y \cos 2\tau - a_y\Big) y \end{aligned} \tag{2.5}$$

where $q_x = -q_y = -2\alpha e V_0/mR_0^2\Omega_{\mathrm{rf}}^2$ and $a_x = a_y = -4\kappa e U_0/mz_0^2\Omega_{\mathrm{rf}}^2$. These differential equations are instances of what is known as the Mathieu equation. It shows up in many other areas of physics, including topics as varied as vibrating elliptical drumheads and the Kapitza pendulum.[4] Since the equations of motion in the x and y directions are identical, we can simplify notation by restricting our attention to motion in the x direction. In the interest of finding analytic solutions that are both applicable to ion trapping and visualizable, we

---

[3] In both the traps mentioned here the reduction in κ is due to the presence of large grounded metal surfaces between the dc electrodes and the trap center. This effect is not particularly surprising, but is mentioned to exemplify the caution against taking too seriously any exact numerical predictions of the analysis to follow.

[4] The Kapitza pendulum is a rigid pendulum restricted to move in a plane under the influence of gravity, where the pivot is moved up and down sinusoidally. The notable feature of such a system is a stable equilibrium point with the pendulum bob pointing straight upward.

will make the typically valid approximations $a_x < q_x^2 << 1$.[5] When these inequalities are satisfied, we can expand solutions of the Mathieu equation in terms of a and q and drop all the higher order terms[64]. This procedure finds the solution to first order in q_x to be

$$x(t) = A\cos(\omega_x t + \phi)\Big(1 + \frac{q_x}{2}\cos\Omega_{\rm rf}t\Big), \tag{2.6}$$

where A and ϕ depend on initial conditions and $\omega_x = (a_x + q_x^2/2)^{1/2}\Omega_{\rm rf}/2$. Inspection of Eq. 2.6 shows that there is motion at two frequencies. The dominant motion at ω_x is the aforementioned "secular" motion. On top of this there is smaller amplitude (reduced by a factor of q_x) motion at the trap drive frequency, $\Omega_{\rm rf}$, called "micromotion." Fig. 2.4 shows trapped ion trajectories found by solving the Mathieu equation numerically and using the approximate analytic solution to second order in q_x. As we should expect, when a and q are small, agreement between the numerical method and the approximation can be quite good.

Often in addition to the intentional trapping fields, there exists some stray electric field at the trap center. Such a stray field will shift the equilibrium position of a trapped ion away from the null of the radiofrequency potential. This produces larger amplitude driven motion at the trap frequency, which is referred to as "excess" micromotion. In order to prevent excess micromotion, the electric field at the trap center must be carefully set to zero by applying voltage biases either to the trap rods themselves or to additional dedicated electrodes. Excess micromotion can also be produced by the presence of a phase difference between the radiofrequency voltages applied to each rod in a linear trap. Micromotion driven in this way can not be cancelled by the addition of voltage biases and so care should be taken to ensure that such a phase difference does not arise.

A final aspect of the Mathieu equation to consider is the condition for obtaining stable solutions. For a linear trap, like the one we consider here, we require that $a < 0$ in order to have stable trapping in the z direction, otherwise the (positively charged) ion would be drawn toward the endcaps and out of the trap. Furthermore, since the dc voltage U_0 on the endcaps creates an anti-trapping electric field in the radial direction, for a given amplitude of the radiofrequency voltage V_0 there is a maximum allowable dc voltage for stable trapping.

---

[5] In my trap, for typical applied voltages the parameters are $a \approx .002$ and $q^2 \approx .04$, so the set of inequalities $a << q^2 << 1$ is well satisfied.

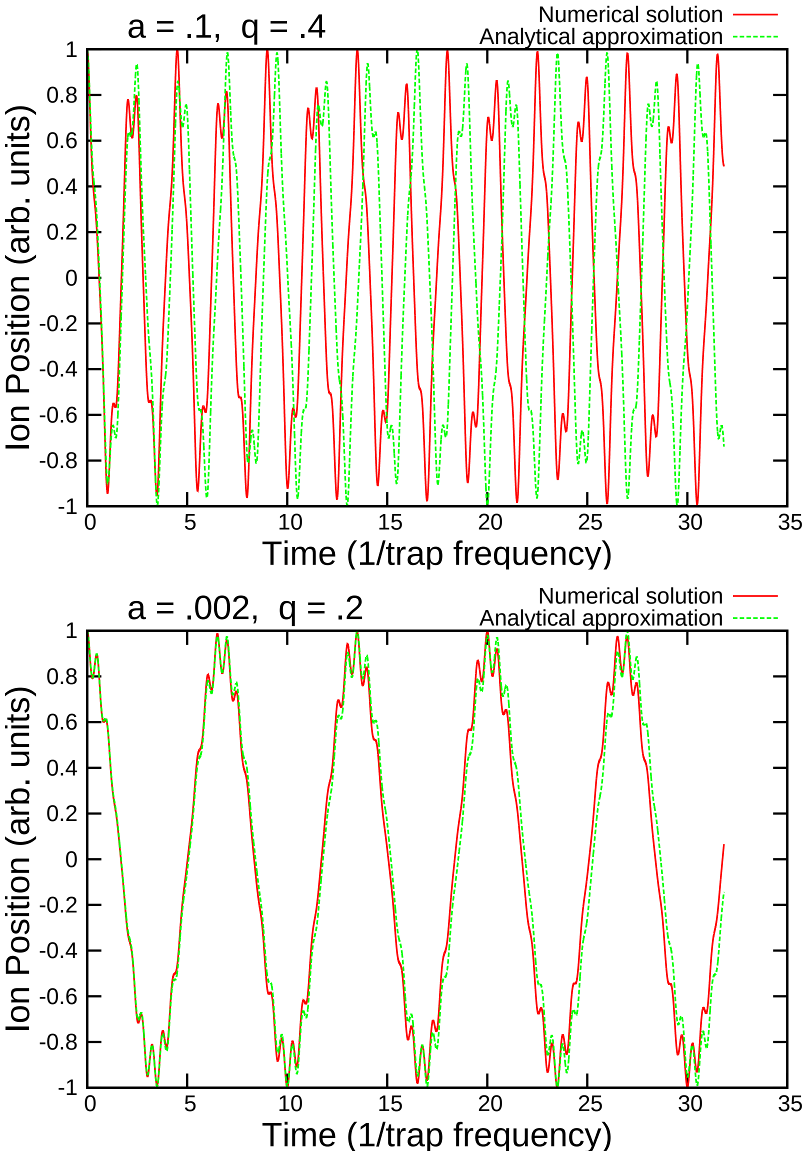

Figure 2.4: Comparison of numerical and analytical solutions of the Mathieu equation. If the values of a and q are too large, as in the top figure, agreement between numerical integration and the first terms of the analytical expansion of the solution of the Mathieu equation will be poor. Yet even in this case the truncated expansion gets the major features of secular motion and micromotion qualitatively correct. In the bottom figure, a and q take roughly the values of the trap to be described later in this work. The numerical solution and the analytical approximation agree on the secular frequency to better than 1%.

In terms of the Mathieu parameters, this means that for a given q, a can only be so large. Additionally, q is limited. For $a \approx 0$, the maximum value of q is about .908. Above this value the ion is accelerated back to the trap center too rapidly, and the amplitude of the radial motion grows with time. The interplay of these effects determines the shape of the stability region, shown in Fig. 2.5.

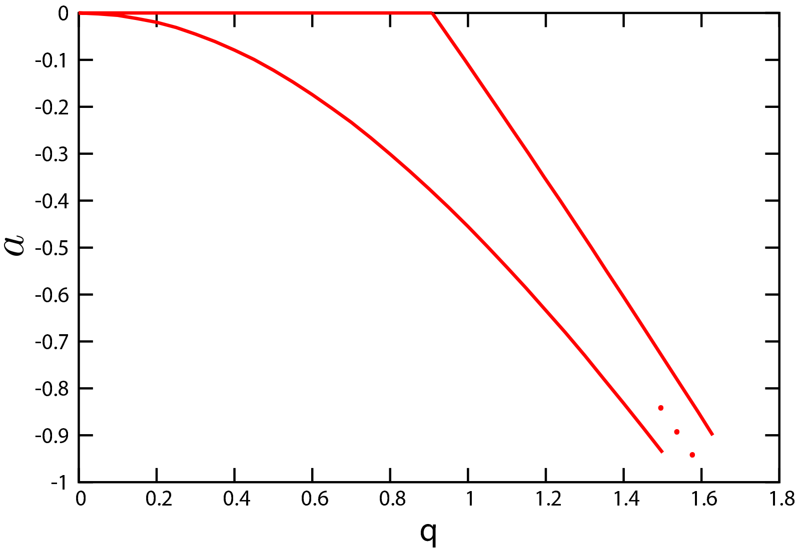

Figure 2.5: Stability region of the Mathieu equation. Given our assumptions, the only requirement for z stability is $a < 0$, so the stability region extends down along the direction marked with the ellipsis. In practice this part of the region is unlikely to be workable and will not be well described by small amplitude micromotion on top of secular motion.

2.3 Doppler Cooling

When a barium ion is initially trapped, it is likely to be at a temperature of several hundred kelvin at which point it will occupy a trap volume of nearly a cubic millimeter. This is not an ideal situation for performing precision experiments using, among other things, tightly focused laser beams. Some method of greatly reducing the amplitude of the ion's motion is desired. Although not the only option, the primary methods employ lasers to damp the ion motion. The method we employ is called "Doppler" cooling owing to the fact that it relies for its efficacy on the cooperation of resonant excitation and Doppler shifting of the laser frequency due to ion motion[63]. For simplicity we consider a two-level ion constrained to move in one-dimension in a classical harmonic trapping potential. The quantum treatment of the trap's harmonic potential, with its quantized motional states, and consideration of motion in three dimensions would make the discussion somewhat more complicated, but would not change the essential features. The fact that laser cooling in Ba^+ is done using two lasers addressing a Λ system of three levels has experimental implications [50, 44], but again does not change the essential features of a simple theoretical examination of Doppler cooling. Given these simplifications, if we apply a laser with frequency ω (and wavenumber $k = \omega/c$) and intensity I to a two-level atom with resonant frequency ω_a moving with velocity v toward the laser, then the scattering rate is given by

$$R_{\mathrm{scatt}} = \frac{\Gamma}{2}\frac{s}{1+s+(\frac{2(\delta-kv)}{\Gamma})^2}, \tag{2.7}$$

where $\Gamma = 1/\tau$, τ is the lifetime of the excited state, $s = I/I_{\mathrm{sat}}$ is the saturation parameter of the laser field, I_{sat} is the saturation intensity of the transition, and $\delta = \omega - \omega_a$. Since each photon carries a momentum $\hbar k$ this scattering rate implies a scattering force $F_{\mathrm{scatt}} = \hbar k R_{\mathrm{scatt}}$. Taylor expanding the scattering force to first order in the ion velocity about $v = 0$ we find

$$F_{\mathrm{scatt}} \approx \frac{\hbar k \Gamma s}{2}\Big(\frac{1}{1+s+4\delta^2/\Gamma^2}\Big)\Big(1+\frac{8kv\delta/\Gamma^2}{1+s+4\delta^2/\Gamma^2}\Big) \tag{2.8}$$

Furthermore, the presence of the trapping potential (assuming our 1-d motion is along the z-axis) implies a restoring force $F_{\mathrm{trap}} = -m\omega_z^2 z$, so that the full force on the ion can be written in the form $F_{\mathrm{tot}} \approx -m\omega_z^2(z - z_0) - \alpha v$ with

$$z_0 = \frac{1}{m\omega_z^2}\frac{\hbar k \Gamma s/2}{1+s+4\delta^2/\Gamma^2} \quad \text{and} \quad \alpha = -\frac{4\hbar k^2 s\delta/\Gamma}{(1+s+4\delta^2/\Gamma^2)^2}. \tag{2.9}$$

Thus we see that the laser provides both a damping force (for negative δ) and a small offset of the equilibrium position of the ion in the trap. By taking derivatives with respect to the laser parameters we can see that the damping force is maximized for $s = 2$ and $\delta = -\Gamma/2$. Plugging in the best s and δ and approximate numbers for trapped Ba^+ ($\Gamma = 125$ MHz, $k = 2\pi/493$ nm, $m = 138$ amu, and $\omega_z = 2\pi \times 500$ kHz) we get $z_0 \approx 20$ nm and $\alpha \approx 4 \times 10^-21$ kg/s $= 20$ Ba^+ mass/ms. A more intuitive way to look at α is to consider the damping time of small oscillations about the equilibrium position, which is given by $t_{\text{damp}} = m/\alpha \approx 50$ μs. So if the ion is perturbed by collisions with the background gas the resulting oscillations will damp out exponentially with a damping time of about 50 μs. Another way to think about α is in terms of a cooling rate $\dot{E}_{\text{cool}} = F_{\text{scatt}}v = -\alpha v^2$. If this were the only effect around we would predict that the kinetic energy of the trapped ion should go to zero, however the fluctuations in the atom velocity due to the recoil impulses from absorption and emission of photons maintain the ion velocity at a non-zero equilibrium value. These recoils lead to a (here, one dimensional) random walk in the ion velocity, which implies that the mean square ion velocity increases by $(\hbar k/m)^2 R_{\text{scatt}} t$ in a time t. Setting this heating process equal to the cooling found above, we find an equilibrium mean square velocity

$$\overline{v^2} = \frac{\hbar^2 k^2 R_{\text{scatt}}}{2m\alpha} = \frac{\hbar\Gamma^2}{4m\delta}(1 + s + 4\delta^2/\Gamma^2). \tag{2.10}$$

Making the equipartition theorem motivated association that the temperature is given by $k_B T = m\overline{v^2}$ and plugging in the values of s and δ that maximize α, we find the Doppler temperature to be $T_D = 2\hbar\Gamma/k_B$. For Ba$^+$, this gives a temperature of 2 mK.

Chapter 3

BELL INEQUALITIES

Any discussion of Bell inequalities begins by mentioning the Einstein-Podolsky-Rosen (EPR) “paradox” [23]. The paradox consists of the observation of the non-local-realistic nature of quantum mechanics together with the intuition that Nature could not possibly behave in such a way. The resolution of this paradox suggested by EPR is that quantum mechanics is not a complete theory, in the sense that a deeper underlying local-realistic theory with additional predictive power must exist. At the time, this was thought to be more or less a philosophical argument since most physicists did not believe that sufficiently precise measurements on individual quantum particles could be practical or that a realizable experiment to discern the presence of such an underlying theory was possible even in principle. These doubts were shattered in 1964, when John Bell proved the existence of a test which could invalidate ALL POSSIBLE local realistic theories in one go [5]. His test consisted of a set of inequalities that must be obeyed by any possible local realistic theory, but which will be violated for highly entangled quantum states. A few years later Clauser-Horne-Shimony-Holt (CHSH) improved on the theorem of Bell by deriving a similar inequality that lends itself more directly to experimental realization [15]. This chapter will glance at the arguments of EPR, then provide a derivation of the CHSH inequality, and finally conclude with a discussion of loopholes in existing Bell inequality tests.

3.1 Einstein-Podolsky-Rosen

I think the arguments made by EPR are of interest, and they are certainly relevant to the long term goal of my project (performing a loophole-free Bell inequality test) so I will flesh them out in a little detail. In the EPR paper, the authors use an entangled state (although they do not use that term) of two systems that are not interacting to show that quantum mechanics is incomplete (given their assumptions about how Nature should behave). They use two particle position/momentum wavefunctions to make their case, but the argument is made somewhat simpler and connections to later discussions of Bell inequalites more direct if we consider instead entangled spin states. Consider a singlet state of two spins,

$$|\Psi_{\mathrm{I,II}}\rangle = \frac{1}{\sqrt{2}}\left(|\uparrow, z\rangle_{\mathrm{I}}\,|\downarrow, z\rangle_{\mathrm{II}} - |\downarrow, z\rangle_{\mathrm{I}}\,|\uparrow, z\rangle_{\mathrm{II}}\right), \tag{3.1}$$

where $|\uparrow, z\rangle$ is the eigenstate of the projection of the spin operator along the z direction with eigenvalue $+\hbar/2$ and $|\downarrow, z\rangle$ is the corresponding eigenstate with eigenvalue $-\hbar/2$. Now if we measure the spin of particle I along z we may find a result of either $\pm\hbar/2$ with equal probability, but in either case we will receive certain knowledge of the z spin of particle II. If particle I is measured to have z spin $+\hbar/2$, then particle II will have z spin $-\hbar/2$ and if particle I is measured to have z spin $-\hbar/2$, then particle II will have z spin $+\hbar/2$. Thus, even in the case of total isolation of the two particles so that no interaction between the spins is possible, measuring the state of particle I provides the experimenter with certain knowledge of particle II. Furthermore, given common conventions, we have that

$$|\uparrow, z\rangle = \frac{1}{\sqrt{2}}\left(|\uparrow, x\rangle + |\downarrow, x\rangle\right) \quad \text{and} \quad |\downarrow, z\rangle = \frac{1}{\sqrt{2}}\left(|\uparrow, x\rangle - |\downarrow, x\rangle\right) \tag{3.2}$$

and so our entangled state can also be written as

$$|\Psi_{\mathrm{I,II}}\rangle = \frac{1}{\sqrt{2}}\left(|\downarrow, x\rangle_{\mathrm{I}}\,|\uparrow, x\rangle_{\mathrm{II}} - |\uparrow, x\rangle_{\mathrm{I}}\,|\downarrow, x\rangle_{\mathrm{II}}\right). \tag{3.3}$$

Therefore, we find a similar situation upon measuring the spin of particle I along the x direction (which we knew we must since the singlet state has zero total spin and must therefore be spherically symmetric). Either measurement outcome for particle I tells us the x spin of particle II with certainty. EPR took this situation to mean that BOTH the x spin AND the z spin of particle II must be “elements of physical reality” and therefore should be predictable by a complete physical theory. After all (by their reasoning) by doing a measurement that can not have possibly affected particle II (since the particles may be outside of causal contact) we would be able to predict the spin of particle II along both x and z. Since quantum mechanics is intrinsically unable to simultaneously predict both spin directions (such a prediction is manifestly forbidden by the uncertainty principle), EPR conclude that quantum mechanics must be an incomplete theory. They admit that there is a glimmer of a hole in their argument but resolve that other alternatives are too abhorrent to consider [23],

> One could object to this conclusion [that quantum-mechanical descriptions are incomplete] on the grounds that our criterion of reality is not sufficiently restrictive. Indeed, one would not arrive at our conclusion if one insisted that two or more physical quantities can be regarded as simultaneous elements of reality *only when they can be simultaneously measured or predicted.* On this point of view, since either one or the other, but not both simultaneously, of the quantites P and Q [the x and z spin of particle II] can be predicted, they are not simultaneously real. This makes the reality of P and Q depend on the process of measurement carried out on the first system, which does not disturb the second system in any way. No reasonable definition of reality could be expected to permit this.

The bracketed comments are inserted by me, but the emphasis is that of the original authors. And so EPR admit that there is an alternative to their conclusion that quantum mechanics is incomplete, but it would require that Nature disobey either the principle of locality or the principle of realism (or both). Locality is the idea that sufficiently separated systems can not interact with one another. This is commonly made specific by saying that no influence may travel faster than the speed of light in a vacuum. The principle of realism is hinted at in the quoted paragraph from the EPR paper. It says that observable quantities must have real values independent of the measurement of those quantities. If we take seriously the idea of quantum states we must surely rid ourselves of either the notion of realism or that of locality. As I said before, the question of local realism and the completeness of quantum mechanics was long thought to be largely philosophical. The predictions of quantum mechanics appeared to agree with experiments so most physicists let such questions languish. Then in 1964 [5], Bell showed that the predictions of quantum mechanics and the predictions of any local-realistic theory that could purport to complete quantum mechanics must be inconsistent. That is, he derived a set of inequalities that must be satisfied by any local-realistic theory, but which can be violated by quantum mechanical states. Here I will reproduce instead the inequality derived by CHSH since it is the inequality we apply to our experimental results [15, 4]. The derivation of the CHSH inequality has exactly the same flavor as the original derivation due to Bell.

3.2 CHSH inequality

The derivation of the CHSH inequality begins by considering an ensemble of correlated pairs of particles such as one might produce in an experiment, where one member of each pair is measured in apparatus I_a and the other is measured in apparatus II_b where a and b are adjustable apparatus parameters determining exactly what measurement that apparatus will make. Each apparatus makes a two-valued measurement the results of which are normalized to ± 1, and the results of the measurements are labeled $A(a)$ and $B(b)$. Now suppose that the correlation between A and B is contained in information localized in the individual particles as befits a local realistic framework, we will label this information by a set of "hidden variables" labeled by λ. The principle of realism then dictates that the measurement outcomes are deterministic functions of these hidden variables, $A(a, \lambda)$ and $B(b, \lambda)$. The state of the ensemble as a whole can be described by a probability distribution on the hidden variables, $\rho(\lambda)$. One further assumption must be made at this point, which is that the probability distribution describing the ensemble of particles to be measured does not depend on the type of measurement that will be performed on them. Specifically, that is, $\rho(\lambda)$ does not depend on a or b. Now we will define a correlation function

$$P(a, b) = \int_{\Gamma} A(a, \lambda) B(b, \lambda) \rho(\lambda) \mathrm{d}\lambda, \tag{3.4}$$

where Γ is the full space of all hidden variables λ. We then make a number of observations about the behavior of these correlation functions. In the formulae to follow, the first inequality is due to the triangle inequality. The remaining steps rely on the fact that the measurement outcomes are always ± 1 so that $1/B = B$ and $|AB| = 1$ and the fact that ρ

is a probability distribution so that $\int_\Gamma \rho(\lambda)\mathrm{d}\lambda = 1$. Thus we have,

$$\begin{aligned}\left|P(a,b) - P(a,b')\right| &\leq \int_\Gamma \left|A(a,\lambda)B(b,\lambda) - A(a,\lambda)B(b',\lambda)\right| \rho(\lambda)\mathrm{d}\lambda \\ &= \int_\Gamma |A(a,\lambda)B(b,\lambda)| \, (1 - B(b,\lambda)B(b',\lambda))\rho(\lambda)\mathrm{d}\lambda \\ &= \int_\Gamma (1 - B(b,\lambda)B(b',\lambda))\rho(\lambda)\mathrm{d}\lambda \\ &= 1 - \int_\Gamma B(b,\lambda)B(b',\lambda)\rho(\lambda)\mathrm{d}\lambda.\end{aligned} \tag{3.5}$$

Now we want to consider a situation with a known large correlation between the particles for a given set of apparatus parameters. Suppose, therefore, that $P(a',b) = 1-\delta$, where we have in mind that δ will be small for a system that will yield an interesting experiment, but where we only require that $0 \leq \delta \leq 1$. We then divide the space of hidden variables into two subspaces $\Gamma_\pm$ such that $\Gamma = \Gamma_+ \cup \Gamma_-$ defined by $\Gamma_\pm = \{\lambda | A(a',\lambda) = \pm B(b,\lambda)\}$. We can also write $P(a',b)$ as

$$\begin{aligned}P(a',b) &= \int_\Gamma A(a',\lambda)B(b,\lambda)\rho(\lambda)\mathrm{d}\lambda \\ &= \int_{\Gamma_+} A(a',\lambda)^2\rho(\lambda)\mathrm{d}\lambda - \int_{\Gamma_-} A(a',\lambda)^2\rho(\lambda)\mathrm{d}\lambda \\ &= \int_{\Gamma_+} \rho(\lambda)\mathrm{d}\lambda - \int_{\Gamma_-} \rho(\lambda)\mathrm{d}\lambda \equiv x_+ - x_-.\end{aligned} \tag{3.6}$$

Since $x_+ + x_- = 1$ and $x_+ - x_- = 1-\delta$, it follows that $x_- = \delta/2$. Returning to Eq. 3.5, we investigate the integral over a product of B's, given our new "known" correlation between $A(a',\lambda)$ and $B(b,\lambda)$. Relating the integral to a fourth correlation, $P(a',b')$, we find,

$$\begin{aligned}\int_\Gamma B(b,\lambda)B(b',\lambda)\rho(\lambda)\mathrm{d}\lambda &= \int_{\Gamma_+} A(a',\lambda)B(b',\lambda)\rho(\lambda)\mathrm{d}\lambda - \int_{\Gamma_-} A(a',\lambda)B(b',\lambda)\rho(\lambda)\mathrm{d}\lambda \\ &= \int_\Gamma A(a',\lambda)B(b',\lambda)\rho(\lambda)\mathrm{d}\lambda - 2\int_{\Gamma_-} A(a',\lambda)B(b',\lambda)\rho(\lambda)\mathrm{d}\lambda \\ &\geq P(a',b') - 2\int_{\Gamma_-} \left|A(a',\lambda)B(b',\lambda)\right| \rho(\lambda)\mathrm{d}\lambda \\ &= P(a',b') - \delta.\end{aligned} \tag{3.7}$$

Now we have three main pieces that we will put together to find the main result.

- $P(a',b) = 1-\delta$

- $|P(a,b) - P(a,b')| \leq 1 - \int_\Gamma B(b,\lambda)B(b',\lambda)\rho(\lambda)\mathrm{d}\lambda$
- $\int_\Gamma B(b,\lambda)B(b',\lambda)\rho(\lambda)\mathrm{d}\lambda \geq P(a',b') - \delta$

Finally we find that,

$$S(a,a',b,b') \equiv \left|P(a,b) - P(a,b')\right| + P(a',b) + P(a',b') \leq 2, \tag{3.8}$$

for correlations between measurements in any local realistic theory. In quantum mechanics, however, we will see that this inequality need not hold for some two particle entangled states. Consider a pure ensemble of pairs of spins in the singlet state given by Eq. 3.1. Spin I (II) is directed at a rotatable Stern-Gerlach apparatus also labeled by I (II), which can be set to two different angles a and a' (b and b'). When the Stern-Gerlach apparata are set to angles a and b, we find that the correlation function $P(a,b)$ to be given by,

$$P(a,b) = \left\langle \Psi \middle| U_I^\dagger(a) S_{z,I} U_I(a) U_{II}^\dagger(b) S_{z,II} U_{II}(b) \middle| \Psi \right\rangle = -\cos(a-b), \tag{3.9}$$

where $|\Psi\rangle$, again, is given by Eq. 3.1, $S_{z,i}$ is the z direction spin operator of the i^{th} spin, and $U(a)$ is the spin-1/2 operator for rotation through an angle a (and $U^\dagger$ is its Hermitian conjugate). Therefore the CHSH Bell signal for the singlet state is

$$S(a,a',b,b') = \left|\cos(a-b) - \cos(a-b')\right| - \cos(a'-b) - \cos(a'-b'). \tag{3.10}$$

S is not bounded by two, and so it is clear that quantum mechanical systems can violate the Bell inequality. Fig. 3.1 shows a plot of the Bell signal as a function of the apparatus parameters b and b' assuming that $(a,a') = (0,\pi/2)$. The green area is the parameter space for which violation of the CHSH Bell inequality is predicted. Maximal violation occurs for $(b,b') = (\pi/4, 3\pi/4)$ when $S = 2\sqrt{2}$. This framework gives the experimenter a straightforward route to investigating whether Nature obeys the tenets of local realism or if a non-local realistic theory like quantum mechanics must be used. In order to make use of the framework, the experimenter must have access to an ensemble of pairs of entangled pseudo-spins and the ability to perform rotations and projective state measurements on the pseudo-spins. The first such experiment used the entanglement in the polarization states of pairs of photons produced in an atomic cascade of calcium [25]. Many additional experiments

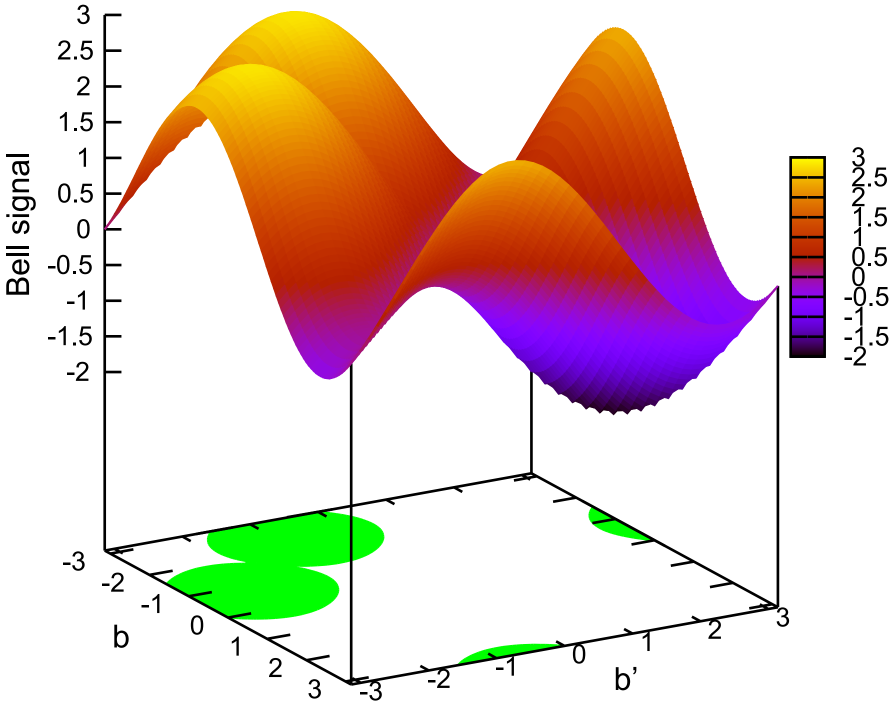

Figure 3.1: Plot of the Bell signal for a singlet spin state assuming $(a, a') = (0, \pi/2)$. The green area shows the parameter space that satisfies $S \geq 2$, so in that region the CHSH inequality will be violated for a singlet state.

have confirmed the violation of Bell's inequalities in a variety of systems including photons [3, 51], protons [39], kaons [8], trapped ions [57, 46], nitrogen vacancies in diamond [53, 52], and superconducting qubits [2].

Proponents of hidden variable theories (or perhaps physicists interested in making Bell inequality violation results absolutely iron-clad) have proposed a variety of loopholes to these tests based on the assumptions made in the derivations of Bell inequalities and the analysis of experimental results. Two of these loopholes are of primary interest for investigations made in trapped ion systems. These are commonly referred to as the "locality" and "detection" (or "fair-sampling") loopholes. The locality loophole suggests that in experiments the detection events of the two particles must be performed with a spacelike spacetime separation. This will prevent an unknown hidden variable field from transmitting information between the particles allowing them to mimic entanglement based quantum correlations. Strictly speaking, the choice of apparatus parameter (a vs. a' and b vs. b') is included in the "detection event" so that all operations from the choice of apparatus parameter through readout of the particle state must be concluded simultaneously in less than the time it takes for light to travel from one measurement apparatus to the other. The detection loophole suggests that if only a subset of the prepared entangled pairs are measured then there may be correlation between the loss mechanism and the particle states that makes the measured subset appear to violate a Bell inequality while the entire ensemble would not [22]. In order to close the detection loophole a sufficient fraction of the prepared entangled pairs must be measured. Since the measurement fidelity for ions can easily be made close to unity, the detection loophole does not pose as significant a challenge for trapped ion experiments as does the locality loophole.

In 2003, Simon and Irvine made a proposal to leverage the high-fidelity detection of trapped ion systems combined with the utility of photons as flying qubits in order to close both the locality and detection loopholes simultaneously in a single experiment [61]. The proposal suggests that a pair of ion-photon entanglements be projected into ion-ion entanglement by performing a Bell state measurement on the two photons. Then the ions to be entangled need not be in the same trap, but rather can be in traps separated by a long distance and the photons can be transmitted between the traps by optical fiber. The details of one half of this experiment (the production of the ion-photon entangled pairs) will be described in Section 8, however here I will only describe the loophole free Bell inequality violation test schematically. Since the entanglement produced by the proposal is between a pair of ions the detection loophole can be easily closed given a sufficiently long duration for integration of detected fluorescence. The locality loophole limits the time available for detection to $T_{\text{det}} < L/c$, where L is the distance between the pair of entangled ions. Fig. 3.2, based on a figure from [61], shows a spacetime diagram of the experimental setup highlighting some of the timing constraints, which are discussed in the figure's caption.

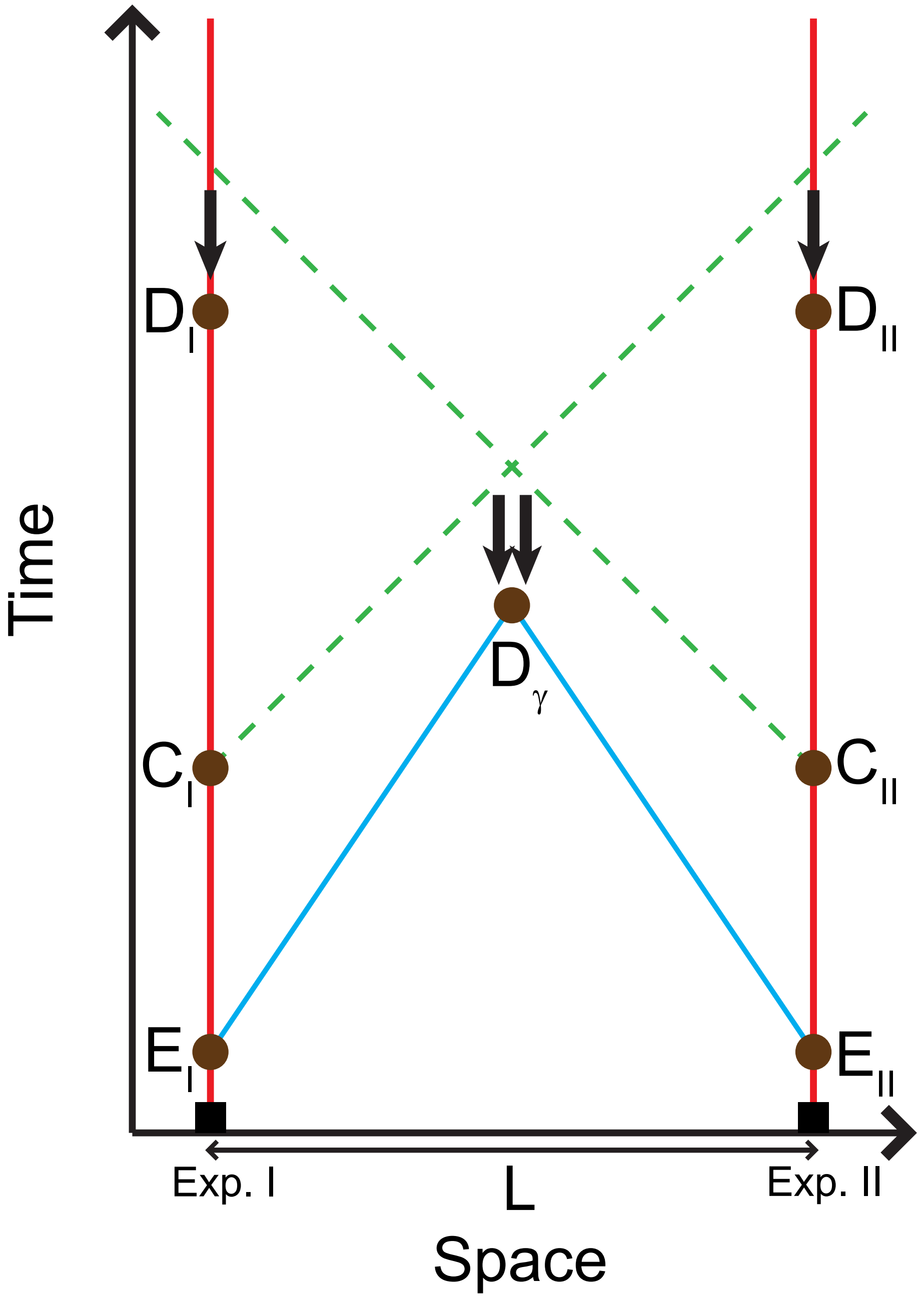

Figure 3.2: Spacetime diagram showing timing considerations for a loophole-free Bell inequality violation test. Experiment I and Experiment II are separated by a spatial distance of L and have their world-lines drawn in red. Several events are shown as brown circles, these are E_i (excitation of the ions), D_γ (Bell state detection of the emitted photons), C_i (choice of ion measurement parameter), and D_i (the time at which the measurement of the ion state is completed). The photons travel to the Bell state analyzer via optical fiber, shown by the blue lines, so they travel more slowly than c and thus the slope of the blue lines is greater than one. Two relevant light cones are shown as green dashed lines. C_I mustn't be allowed to affect either the bell state detection or the detection of the second ion, thus both D_γ and D_II must be outside of the forward light cone of C_I. A similar relation holds for C_II with respect to D_γ and D_I. These requirements are indicated by black arrows.

Part II

EXPERIMENTAL APPARATUS

Chapter 4

X-TRAP

The first trap I used was a four rod linear trap similar to the one shown in Fig. 2.3 in the section on Paul traps and has been extensively discussed in [20, 37]. It differed from the design shown in the figure in that there were needles for application of the dc voltage required for trapping along the trap axis. Also, the opposite pairs of rods were electrically connected inside of the trap[1], which made it impossible to bias the rods for micromotion compensation. Toward the end of the life of the trap we became interested in being able to drive transitions between Zeeman states of the same energy level, especially between $m = +1/2$ and $m = -1/2$ in the ground state. Early efforts to drive these rf transitions using coils of wire outside the vacuum chamber proved unsuccessful. To address these issues I built a new trap with dedicated electrodes for micromotion compensation and application of rf magnetic fields for driving Zeeman transitions. We were interested in using a new design, so I looked into the advantages of using blade shaped electrodes instead of rods [28]. The major advantage is that the blade tips can be brought nearer to the ion position for a given unobstructed solid angle (for light collection and laser addressing) and rod radius. Since the secular frequencies are inversely related to the ion-electrode separation, bringing the electrodes closer to the trap center makes the trap tighter. Of course the same benefit can be gotten in a four rod trap by shrinking the radius of the rods and reducing the separation between them, but maintaining the mechanical stability of the trap limits this option.

I drafted a 3D design of the trap electrodes and spacers using Solidworks, and some images based on that model are shown in Fig. 4.1. Peter Hirtle of the UW physics instrument shop machined the trap components. The electrodes are made from stainless steel

---

[1] If the rods are connected inside the trap, they can be cleaned of Ba deposition by running current through them.

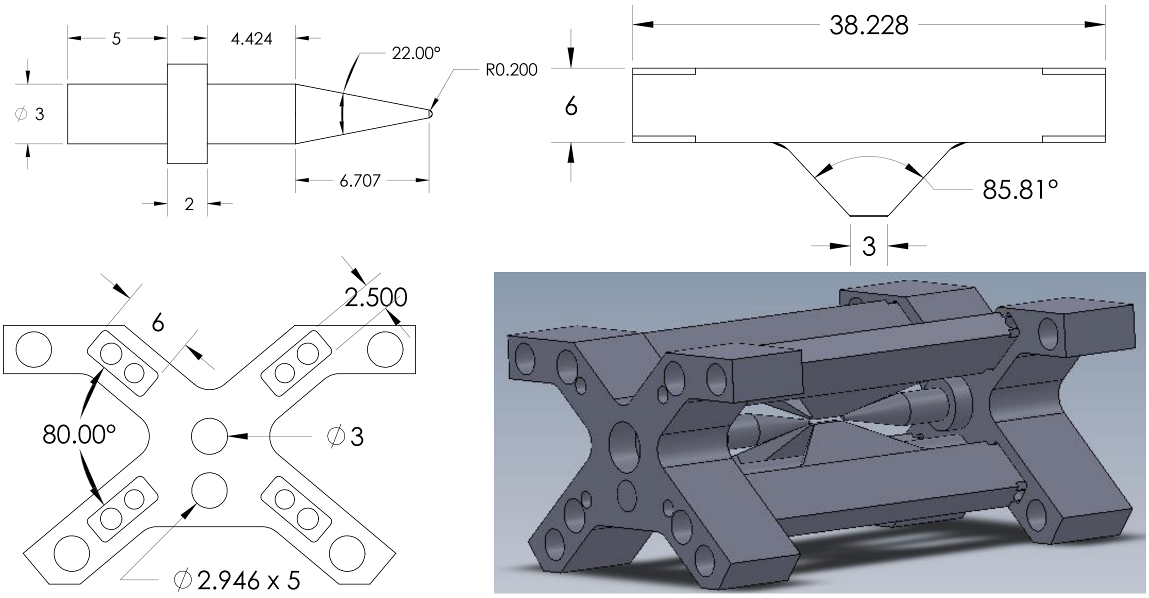

Figure 4.1: Solidworks drafting of the X-trap. Top left shows an endcap electrode, top right a blade electrode, bottom left the insulating spacer, and bottom right a 3D rendering of the trap assembly. All length dimensions are in millimeters. The blade and spacer drawings are to scale with each other and the endcap drawing is expanded by a factor of 1.75 with respect to that scale. The "extra" holes in the spacer are used to mount electrodes dedicated to compensation of micromotion and for attaching the trap assembly to groove grabbers for vacuum chamber mounting. Upon assembly, the separation between the endcaps is 3.6 mm and the separation between opposite blades is 0.8 mm.

and the spacer from a machinable glass-ceramic called MACOR®. The radial electrodes were machined, in part, by wire-cut electrical discharge machining, whereas the spacer and endcaps were made with more standard milling and turning techniques. Photographs of the bare assembled trap and the trap installed in the vacuum chamber can be seen in Fig. 4.2

The rf voltage produced by an HP8640 signal generator is amplified and matched to the frequency of a homemade quarter-wave helical resonator with $Q \approx 400$, which is used to couple the voltage on to the blade electrodes through a vacuum feed-through. The helical resonator steps up the amplitude of the voltage that is applied to the trap, provides some filtering of non-resonant frequencies, and matches to the (largely capacitive) impedance of the trap. High voltage dc is applied to the endcaps and compensation electrodes through a separate feed-through. The combination of these voltages forms a stable trap along the null of the rf potential, as described in Chapter 2. The trap is installed in a spherical octagon UHV chamber[2] (as shown in Fig. 4.2), which has seven viewports, in addition to the aforementioned pair of electrical feedthroughs. Six viewports are arrayed around the diameter of the spherical octagon and are used for directing laser beams through the trapping region. The seventh viewport is mounted to a recessed flange above the trap so that the external glass surface is only about 1.3 cm above the ion position. This would allow optics to be brought close to the trap to maximize the collection of fluorescence from the trapped ions. More will be said about this shortly. The bottom flange of the spherical octagon connects the trap chamber to the rest of the vacuum system. This system includes a 20 l/s Varian Star-Cell ion pump and a titanium sublimation pump, which together bring the system to a pressure lower than the 4×10^{-11} torr that is the minimum measurable level for the attached ion gauge[3].

For most of the work described in this dissertation the ion imaging system was as follows. Fluorescence from the trapped ions is collected by a long working distance microscope objective[4]. The light from the objective is imaged on to a pinhole, which provides spatial filtering of light scattered off the trap electrodes. A 25 mm doublet subsequently re-images the light on to either a Hamamatsu photon counting PMT or an Andor Luca EMCCD camera. The camera is primarily used for diagnostics (ion number counting, gross ion temperature estimation, simple micromotion compensation, etc.) and the PMT is used for quick determination of the fluorescence level coming from the trapped ion(s), which, we will see, can provide a high fidelity measurement of the internal state of the ion(s). Additionally, a 493 nm transmissive interference filter can be placed in the imaging beam line in order to greatly reduce the PMT background and also to provide a convenient means

---

[2] Kimbal physics part number MCF450-SphOct-E2A8

[3] Since the ion gauge is located nearer to the pumps than the trap chamber it is likely that the pressure is somewhat higher near the trap. However, collisions of sufficient momentum transfer to delocalize the trapped ions happen rarely as diagnosed by viewing the ions on a camera so the pressure is unlikely to be much higher.

[4] Mitutoyo M Plan Apo 10x, .28 NA, working distance 33.5 mm, clear input aperture 24 mm diameter, transmits 90% at 493 nm

of distinguishing background PMT counts from fluorescence counts. With the interference filter in place a negligible amount of scatter from the 650 nm repump laser will transmit to the PMT. Thus if the PMT signal is due to background (room light, 493 nm laser scatter, PMT dark counts), turning off the 650 nm laser must not change the signal. However, when the 650 nm laser is shuttered the ion will rapidly be pumped into the long-lived $5D_{3/2}$ state and so will cease scattering light from the 493 nm laser. So the fraction of the PMT signal that is due to ion fluorescence will disappear when the 650 nm laser is turned off.

Trapping barium ions, requires a source of barium ions, which, in turn, requires a source of neutral barium. Chunks of metallic barium are shaved into an alumina tube which is mounted via a MACOR® spacer to a third feedthrough below the trap. A tungsten wire is coiled around the alumina tube and connected to feedthrough pins on either end. Passing a current through the tungsten wire heats the barium in the tube causing some atoms to evaporate. A small fraction of these atoms are directed along a path so that they pass through the trap volume. A Solidworks depiction of this system is shown in Fig. 4.3.

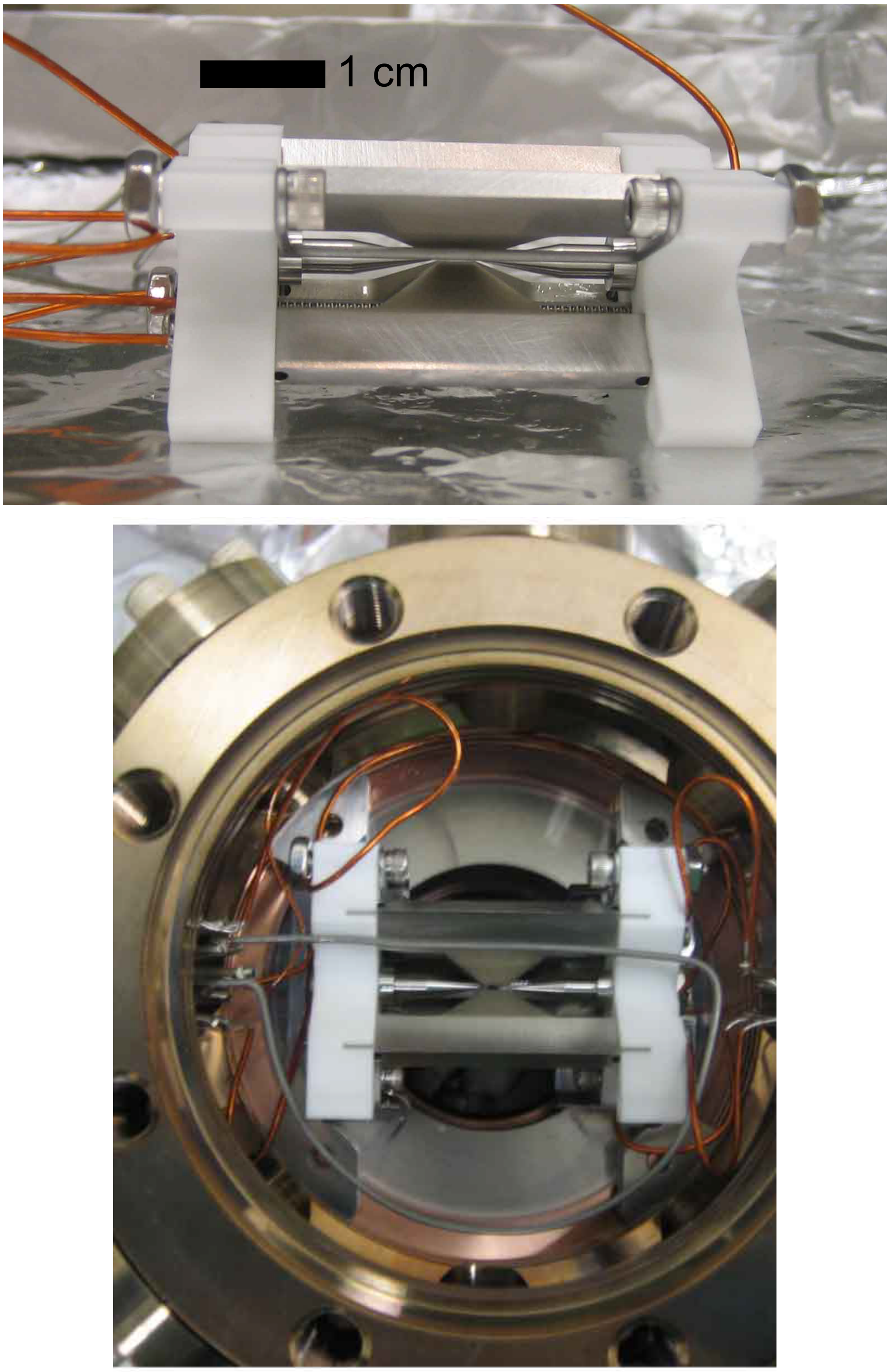

Figure 4.2: The spacer and electrode design allows the trap to be easily assembled with standard #0, #2, and #4 vented screws. In the upper image the horizontal micromotion compensation electrode obscures the view of the trap center. The vertical micromotion compensation electrode is the threaded rod running beneath the trap. A hole is drilled in the vertical compensation electrode to allow neutral barium flux to enter the trap from below. A sheet metal shield sits below the trap to minimize coating of the trap electrodes by the barium flux. The wire running above the trap in the lower image is the electrode dedicated to driving Zeeman transitions. The feed-through on the right makes the connections to the blade electrodes, while all other connections are routed to the feed-through on the left. The insulating spacers are attached to groove-grabbers, which are attached, in turn, to the vacuum chamber.

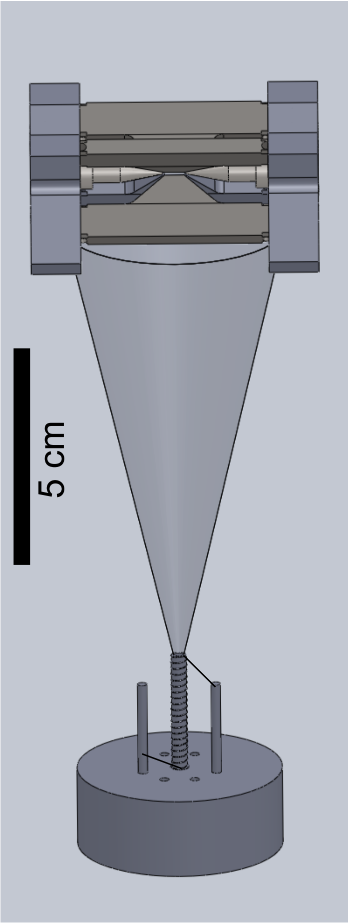

Figure 4.3: Barium oven assembly and trap. The oven is an alumina tube containing chunks of metallic barium. A tungsten wire is wrapped around the oven and attached to feedthrough pins. When current flows through the wire the oven heats up and evaporates barium atoms depicted by the (far too narrow) gray cone extending up from the oven opening. This barium flux is collimated by a sheet metal shield (not shown) and passes through the trap.

Chapter 5

LASER SYSTEMS AND APPARATUS CHARACTERIZATION

This chapter will take a meandering look at the aspects of a simple diagnostic experiment: measuring the temperature of a trapped ion. The chapter has two main goals, which will hopefully be accomplished simultaneously. First, we will introduce all the laser systems necessary for our experiments with $^{138}\mathrm{Ba}^{+}$ and, second, we will get a first look at the methodology of trapped ion experimentation, specifically the way in which a long lived “shelved” state is used to obtain information about the internal state of $^{138}\mathrm{Ba}^{+}$ following some set of interactions. First, before we discuss the laser systems, let us say a few words about temperature as it relates to trapped ions. Temperature is typically a collective parameter of a large ensemble of particles in thermal equilibrium and so does not apply terribly well to our system of a single isolated ion. Nevertheless, given that the trapping potential is well approximated by a three dimensional harmonic oscillator, we may think of temperature as being manifested as a mixed motional state characterized by an average motional quantum number, $\bar{n}$, in each direction. We then identify the ion temperature by $T \approx \bar{n}_i \hbar\omega_i / k_B$, where ω_i is the trap frequency in the i^{th} direction. Thus if we want to measure ion temperature what we will really be attempting to measure is $\bar{n}$, and we will need some mechanism for interacting with the ion’s motional state. Such a mechanism is given to us by addressing a transition which is much narrower than the trap frequencies, so that the motional sidebands of the transition are well resolved from the carrier. The 1.76 μm transition between $6S_{1/2}$ and $5D_{5/2}$ is such a transition in $^{138}\mathrm{Ba}^{+}$. But now we are getting ahead of ourselves, taking a step back, if we want to perform an experiment on trapped $^{138}\mathrm{Ba}^{+}$, first we must trap $^{138}\mathrm{Ba}^{+}$. The trap and source of neutral barium were discussed in the previous chapter, so the first thing to describe here is ionization of the neutral barium flux.

For ionization we use a pair of lasers. First a homebuilt ECDL in Littrow configuration (all of the ECDLs used in this work are homebuilt and Littrow) at 791 nm excites an intercombination line in neutral barium, and then a pulsed nitrogen laser at 337 nm kicks the excited electron into the continuum. The 791 nm laser is side-of-the-fringe locked to a ∼10 cm long temperature-stabilized, superinvar-spaced optical cavity with a linewidth of about 100 MHz. Fig. 5.1 shows the temperature stability of the cavity and is representative of the temperature stability of all our optical cavities. The lock provides short term stability on the order of a few megahertz and long-term drifts of about 10-20 MHz/hr. I won't cover the side-of-the-fringe lock electronics here since they were not designed by me, but some description can be found in Matt Hoffman's lab book. A brief description of the temperature control circuit can be found in Appendix A. This ionization scheme has the advantage of isotope selectivity. The neutral barium transition at 791 nm is much narrower than the isotope shift between different isotopes of barium, so by tuning the frequency of the 791 nm laser any isotope of barium can be selectively excited and subsequently ionized. Since the experiments described here exclusively use the most abundant isotope, ^{138}Ba, isotope selectivity is convenient but not critical. When attempting to trap a lone ^{137}Ba^{+}, isotope selectivity is crucial.

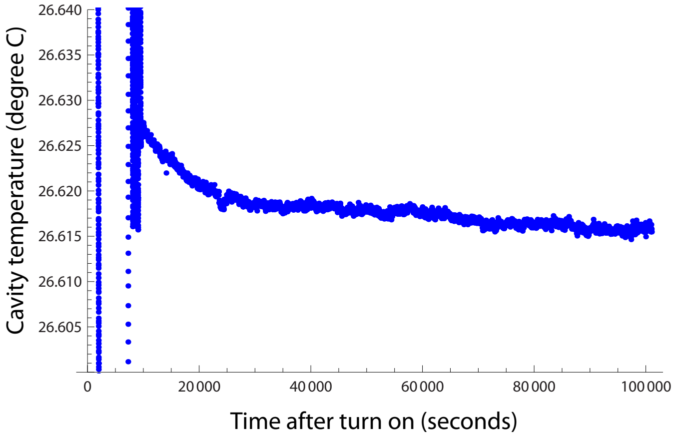

Figure 5.1: Temperature stability of the 791 nm cavity. The system is underdamped, so there is an initial ring down to the set point when the controller is first turned on. Then once the set point is reached the hour-long standard deviation of data points is about .3 mK with a drift of about .2 mK/hr. This data was taken over a weekend when the lab was empty, the drifts observed while the lab is occupied are somewhat worse.

Once a barium atom is ionized it suddenly feels the trapping potential around it and if its kinetic energy is less than that required to escape the trap it will remain trapped, executing large complicated orbits about the trap center. Doppler cooling acts to reduce the velocity of the trapped barium ion, but initially it isn't very efficient due to the small overlap of the ion trajectory with the volume of the cooling laser beams. The cooling lasers are focused to a waist of roughly 25 μm near the trap center, compared with the initially almost millimeter sized extent of the ion motion. Thus the ion may take tens of seconds after initially being ionized to cool sufficiently that it spends enough time in the cooling lasers to be detected. If one is trying to trap single ions this effect limits the ionization rate one can use. If the ionization rate is too high, the first ion is likely to gain a partner before it is cool enought to scatter enough photons to be visible on the PMT.

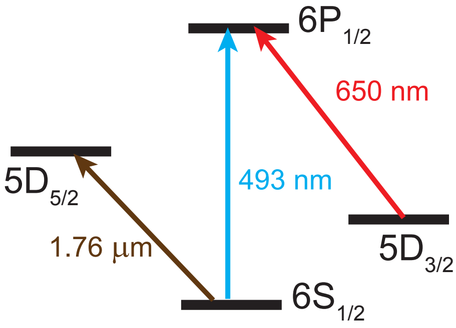

Figure 5.2: Relevant level structure of ^{138}Ba^{+}. Doppler cooling is done on the 493 nm and 650 nm transitions. State readout is accomplished by shelving the valence electron to the $5D_{5/2}$ level. Not to scale.

Doppler cooling is primarily done on the $6S_{1/2}$-$6P_{1/2}$ transition at 493 nm, but since the $6P_{1/2}$ level has a branching ratio of about .25 for decay to the $5D_{3/2}$ level ($\tau \sim$ 80s [67]) a 650 nm repump laser is necessary. The 493 nm beam is derived by frequency doubling the output of an ECDL at 986 nm in a waveguide PPLN crystal. The 650 nm laser is another ECDL. Both cooling lasers are locked to cavities similar to the one described above for the 791 nm laser. The 986 nm laser also uses a side-of-the-fringe locking scheme, while the 650 nm laser uses a scheme based on lock-in detection of a frequency modulation signal applied to the laser by an AOM, which is described in Appendix B. These laser systems and others are shown in the apparatus schematic in Fig. 5.3. The Doppler cooling limit, as discussed in Chapter 2, for the $6S_{1/2}$-$6P_{1/2}$ transition is roughly $\hbar/\tau \approx 1$mK. However, the presence (and simultaneous addressing) of the $5D_{3/2}$-$6P_{1/2}$ transition means that this Doppler limit is only a ballpark estimate of the minimum temperature one should expect. So now we have a trapped, crystallized, fairly cold ^{138}Ba^{+}, from which we will detect several thousand fluorescence photons per second on a PMT when the ion is in the cooling cycle. This is a first hint of how we might learn something about the internal state of the ion: if we see a large number of PMT counts above the background level, then the ion must be in the cooling cycle.

However, before we more fully pursue the question of state readout, let's consider the question of state initialization. A common technique for state initialization in atomic systems is called optical pumping wherein a set of applied fields drives population out of all populated states but one, which is referred to as the "dark" state since, by design, it will not scatter any light. If there is any decay path into the dark state, then eventually all population must build up there. In ^{138}Ba^{+}, we use such a scheme to prepare the ion in a particular Zeeman state of the $6S_{1/2}$ level. Shining 650 nm light on the ion depopulates all the $5D_{3/2}$ states which would prepare the ion in a mixture of the two $6S_{1/2}$ Zeeman states. If we additionally apply a circularly polarized 493 nm beam along the quantization axis, we may selectively depopulate either of the ground Zeeman states, since such light will only drive σ ($\Delta m = 1$) transitions. Thus, by applying the 650 nm repump and well polarized 493 nm light we may initialize the ion in either ground state, where the particular Zeeman state is selected by the handedness of the 493 nm beam's polarization. This technique relies for its fidelity on the purity of the polarization of the 493 nm beam, which hereafter will be referred to as the optical pumping beam, and the beam's colinearity with the magnetic field at the position of the ion. Birefringence in the viewports, the quality of the polarizer and $\lambda/4$ waveplate used to generate the circularly polarized beam, and the difficulty of precise alignment of beam direction and magnetic field limit the efficiency of this form of optical pumping to about .96(2) without intensive effort, which is to say, some 4% of the population remains in the "bright" $6S_{1/2}$ Zeeman state. Now we have trapped, crystallized, cold ^{138}Ba^{+} initialized into a particular ground Zeeman state. It is time to consider state

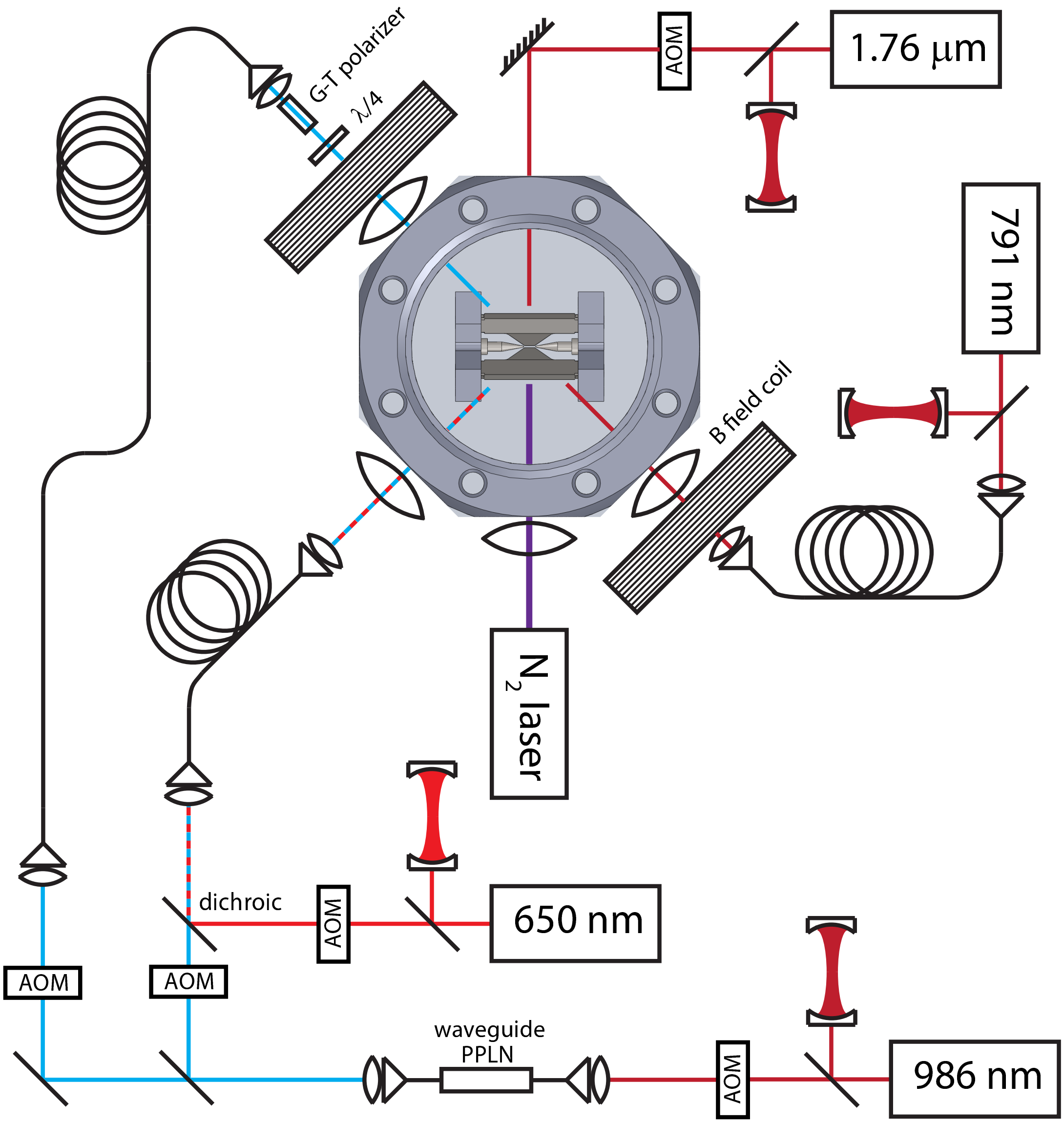

Figure 5.3: Schematic diagram of laser systems and trap addressing. Although the angular deflection is suppressed in the diagram, all AOMs shown are for switching and so the zeroth order out of each AOM is blocked while the first diffracted order continues to propagate through to the ion.

readout.

State readout uses the fact that the $5D_{5/2}$ "shelved" level is long-lived ($\tau_{5D_{5/2}} \approx 30$s

[43]) and disjoint from the cooling cycle. Thus if the ion somehow ends up in that level, the PMT counts from the ion will cease even in the presence of the cooling lasers. A fiber laser at 1.76 μm gives us a method of transferring population to the shelved state. The fiber laser is locked to a Zerodur spaced optical cavity by the PDH technique and has a resulting linewidth on the order of 100 Hz. This laser and its locking system are described in detail in the dissertation of Matt Dietrich [20]. This narrow linewidth allows for selective coherent excitation of population from a single ground state to a single state in the $5D_{5/2}$ level, as shown by the Rabi oscillations in Fig. 5.4. The figure shows oscillation between the

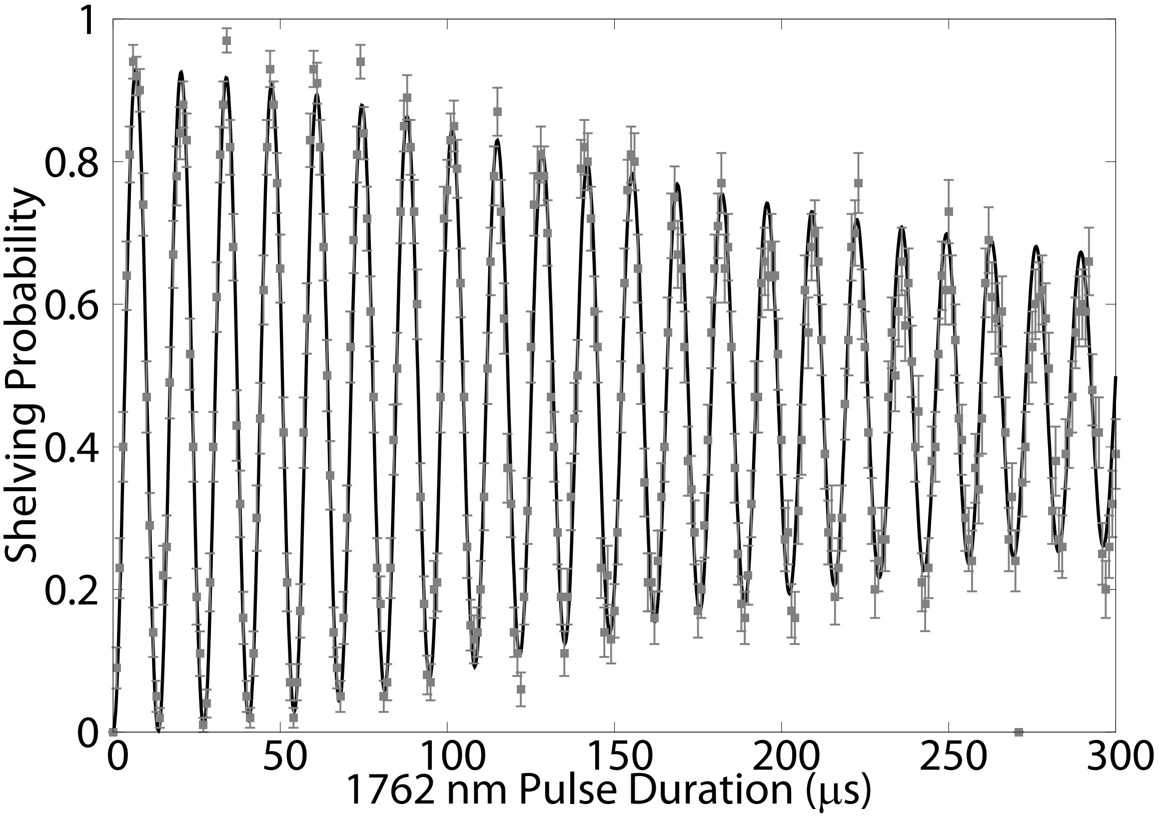

Figure 5.4: Rabi oscillation between $6S_{1/2}(m = -1/2)$ and $5D_{5/2}(m = -5/2)$ states. The probability that the ion is found to be dark after a given duration of application of the 1.76 μm laser. Population flops back and forth coherently between the ground and shelved states. The maximum excitation probability is limited primarily by optical pumping efficiency and the decay in contrast is due to ion temperature as will be discussed in the main text. The Rabi frequency here is $2\pi\times$ 74 kHz. Errorbars are statistical based on the binomial distribution with 100 runs per point.

$6S_{1/2}(m=-1/2)$ and $5D_{5/2}(m=-5/2)$ with a Rabi frequency of $\Omega = 2\pi \times 74$ kHz and a π-time (the time it takes for full population transfer between the states) of $T_\pi = \pi/\Omega = 6.7\mu$s. Thus to determine the population in the $m=-1/2$ ground state after some known set of operations, we may simply turn on the 1.76 μm laser for 6.7 μs and measure the probability that the ion is dark. The full experimental sequence for acquisition of the data shown in Fig. 5.4 is as follows, with the assumption that a detailed frequency scan has already been performed so that we know the frequency of the intended 1.76 μm transition. Typically the experimental repitition rate is roughly 10-20 Hz.

(a) Doppler cool

(b) Optically pump to the $6S_{1/2}(m=-1/2)$ state

(c) Apply the 1.76 μm laser on resonance with the $6S_{1/2}(m=-1/2)$ to $5D_{5/2}(m=-5/2)$ transition for a time T

(d) Turn on cooling lasers and record the fluorescence state of the ion

(e) Deshelve ion, if necessary

(f) Repeat (a-e) with the same T 100 times to build up statistics

(g) Vary T and repeat (a-f) to trace out the Rabi oscillation curve

In practice, using π-pulses for state readout has a number of disadvantages. This will be discussed in some detail in Chapter 6, where we present our investigation of using adiabatic rapid passage (ARP) for state readout. Briefly, ARP has the advantage of being robust against a number of possible experimental imperfections, including insensitivity to laser frequency and intensity, magnetic field drifts, ion temperature, and the precise values of excitation parameters. For these reasons, we employ ARP for shelving when our goal is to read out the ground state of the ion. However, the insensitivity of ARP to ion temperature renders it of little use for our purposes in this chapter, so we will delay further discussion until Chapter 6.

5.1 *Ion temperature measurement*

In order to measure the ion temperature after Doppler cooling, we make use of the temperature dependence of excitation on the $6S_{1/2}$-$5D_{5/2}$ transition. Since both the laser linewidth and the transition linewidth ($\tau_{5D_{5/2}} \approx 30$s and broadening due to magnetic field noise is less than a kilohertz on millisecond timescales) are much smaller than the trap's axial and secular frequencies, it is possible to use the 1.76 μm laser to resolve the sidebands of the $6S_{1/2}$-$5D_{5/2}$ transition. The resolved sidebands due to axial motion in the trap are shown in Fig. 5.5. The data in the figure is acquired by a procedure very similar to that detailed for the Rabi oscillation data, except that the frequency of the 1.76 μm laser is varied and the pulse duration is held constant. In this way we trace out the 1.76 μm transition resonance as well as the axial frequency sidebands. Given the simple harmonic oscillator picture of the ion motion, the sideband transitions correspond to changing not only the ion's elec-

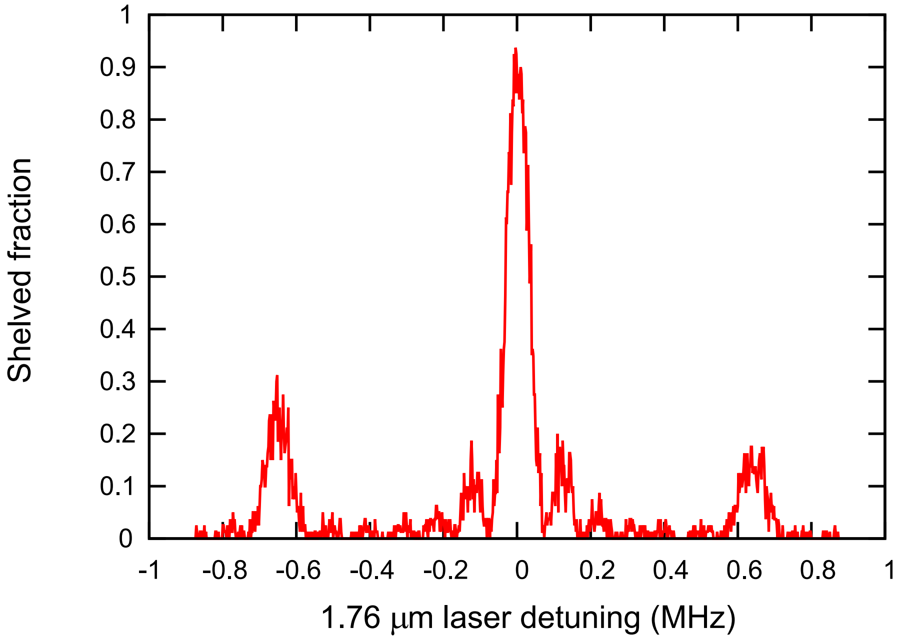

Figure 5.5: 1.76 μm laser frequency scan, showing carrier and axial sidebands. The substructure in the carrier (and sidebands, perhaps) is due to coherent excitation by a duration slightly shorter than a π-pulse. From this spectroscopy we can read off that the axial trap frequency is about 650 kHz.

tronic state, but also its number of motional quanta. By tuning the 1.76 μm laser above a carrier resonance by 650 kHz, the frequency of oscillation of the ion's motion along the trap axis when Fig. 5.5 was taken, we would not only excite the ion's electronic state to the $5D_{5/2}$ level, but also introduce an additional quantum of motion to its motional state. And if we tune the laser an equal detuning below resonance we would remove a quantum of motion. Fig. 5.5 shows the sideband resonances associated with changing the electronic and motional state of the ion. There are two methods by which we can use excitation to the $5D_{5/2}$ level to obtain information about the ion temperature. First, the ratio of the amplitudes of excitation of the red and blue sidebands or the ratio of the amplitude of either sideband to the carrier contains information about the ion temperature. Second, the frequency of excitation on the carrier from the ground state with n motional quanta to the $5D_{5/2}$ level with n motional quanta is slightly different than the same transition from $n+1$ to $n+1$. The temperature of the ion is manifested as a distribution of different values of n, so there will be many (order of $\bar{n}$) slightly different excitation frequencies contributing to Rabi oscillations. This will appear as a decay of the contrast of the Rabi oscillation as the different frequencies become more and more out of phase. By fitting the decay we can extract information about the ion temperature.

The Rabi frequency connecting motional level n to motional level $n+s$, is given by [63, 40]

$$\Omega_{n,n+s} = \Omega_0 e^{-\eta^2/2} \eta^{|s|} \sqrt{\frac{n_<!}{n_>!}} L_{n_<}^{|s|}(\eta^2). \tag{5.1}$$

where Ω_0 is the Rabi frequency on the $n=0$ carrier transition, η is the Lamb-Dicke parameter, $n_<(n_>)$ is the lesser (greater) of n and $n+s$, and $L_n^\alpha(x)$ is the associated Laguerre polynomial given by

$$L_n^\alpha(x) = \sum_{j=0}^{n} (-1)^j \binom{n+\alpha}{n-j} \frac{x^j}{j!}. \tag{5.2}$$

The Lamb-Dicke parameter describes the relative sizes of the radiation wavelength and the spread of the ion's motional wavefunction; it is given by $\eta = k\sqrt{\hbar/2m\omega}$, where k is the wavenumber of the driving field, m is the ion mass, and ω is the motional (axial or secular) frequency of the ion in the trap. Since we are primarily interested in either carrier or first order sideband transitions and since η is a small parameter for the 1.76 μm transition given typical trap frequencies, we can make some simplifications to Eq. 5.1. For carrier transitions,

$$\Omega_{n,n} \approx \Omega_0 \left(1 - (n + \frac{1}{2})\eta^2 + (\frac{1}{4}n^2 + \frac{3}{4}n + \frac{1}{8})\eta^4 + \cdots\right) \tag{5.3}$$

and for first order blue sidebands,

$$\Omega_{n,n+1} \approx \Omega_0 \eta \sqrt{n+1} \left(1 - \frac{1}{2}(n+1)\eta^2 + \cdots\right). \tag{5.4}$$

Unless $\bar{n}$ is very large (nearly $1/\eta^2$) you won't need to go to higher terms and for the precision we are looking for we typically don't even include the terms of order η^3 or higher. The first method of getting at $\bar{n}$ mentioned above is to look at the ratio of the Rabi frequency on the carrier and the first order sideband. This ratio, for a given starting n, is given by

$$\zeta \equiv \frac{\Omega_{n,n+1}}{\Omega_{n,n}} \approx \eta\sqrt{n+1}(1 + n\eta^2/2). \tag{5.5}$$

A rough idea of $\bar{n}$ can then be found by making the substitution $n = \bar{n}$ on the right hand side of the equation above and using measured values of of the Rabi frequencies and the Lamb-Dicke parameter. Using the data in Fig. 5.5, we can use this idea to extract a rough estimate of the ion temperature when the data was taken. We can read off that the axial frequency is about 650 kHz, which implies a Lamb-Dicke parameter for the 1.76 μm laser of $\eta = .027$. Using a Rabi model for the excitation, we find the ratio of the sideband Rabi frequency to that of the carrier, in terms of the peak amplitudes A_{sb} and A_{c} and the efficiency of optical pumping F, to be $\zeta = \arcsin\sqrt{A_{\text{sb}}/F}/\arcsin\sqrt{A_{\text{c}}/F}$. From the plot we read off that $A_{\text{sb}} = .14$ and $A_{\text{c}} = .88$ and typically the optical pumping efficiency is about $F \approx .96$. Using these numbers we find the ratio of the Rabi frequencies to be $\zeta \approx .31$, which corresponds to a mean thermal phonon occupation number of $\bar{n} \approx 120$ in the axial mode. This $\bar{n}$, in turn, implies a temperature of roughly $T \approx \bar{n}\hbar\omega_z/k_B \approx 4$ mK.

The astute reader may raise the objection that the ratio of Rabi frequencies of the red and blue sidebands should be about $\bar{n}/(\bar{n}+1)$, which, given an $\bar{n}$ of about one hundred, should be indistinguishable from one[1]. Looking at the data in Fig. 5.5 however, one immediately

---

[1] In the scenario where the mean phonon occupation number is very small, the $\bar{n}/(\bar{n}+1)$ ratio of the sideband frequencies provides the best method of determining $\bar{n}$.

notices a difference between the amplitudes of the two sidebands. The explanation of this is that taking such a highly detailed frequency scan as is shown in the figure takes nearly an hour. If care is not taken to correct for drifts in the lock points of cooling lasers, they will drift sufficiently to change the Doppler cooled ion temperature by a few millikelvin. Improved temperature control of the cavities used for locking the cooling lasers would mitigate this issue.

The second method for measuring ion temperature mentioned earlier relies on fitting the decay of Rabi oscillations on the carrier transition like that shown in Fig. 5.4. Again, since $\Omega_{n,n}$ has a weak dependence on n the probability of driving the transition is an incoherent sum of sinusoidal functions with slightly different frequencies resulting in an envelope on Rabi oscillations that depends on $\bar{n}$. Mathematically this looks like, assuming the field is resonant,

$$P_{5D_{5/2}} = \frac{1}{2}\left(1 - \sum_{n=0}^{\infty} p_n \cos\left(2\Omega_{n,n} t\right)\right), \tag{5.6}$$

where $\Omega_{n,n}$ is given by Eq. 5.3 and the weighting is given by a thermal distribution so that

$$p_n = \frac{1}{\bar{n}+1}\left(\frac{\bar{n}}{\bar{n}+1}\right)^n. \tag{5.7}$$

For typical $\bar{n}$, the first 500 or 1000 terms in the sum are necessary to give a good fit (and at that point using additional terms no longer changes the best fit value of $\bar{n}$). This procedure assumes that the laser used to drive the transition is aligned with only a single mode of oscillation of the ion, which generally is not true. Usually lasers are directed either perpendicular to the axis of the trap or at 45 degrees to the axis. When the laser is at 45 degrees to the axis and when the axial frequency is much smaller than the radial secular frequencies (the typical case of linear Paul traps), the Lamb-Dicke parameter associated with the axial motion will be larger than that for the radial motion and the decay envelope will be dominated by contributions from axial motion. If the laser is pointed nearly along the radial direction, on the other hand, assuming that the two radial secular frequencies are nearly equal, then this procedure will once again work well using the Lamb-Dicke parameter for radial motion. The data in Fig. 5.4 was taken with the 1.76 μm laser pointed perpendicular to the trap axis. The radial secular frequencies were both roughly $\omega_{x,y} \approx 1.7$ MHz (the two directions differ by only a couple hundred kilohertz), corresponding to a Lamb-Dicke parameter of roughly $\eta = .017$. Fits to Eq. 5.6 find that $\bar{n} \approx 50$, which corresponds to a temperature of $T \approx 4$ mK.

In summary, using Doppler cooling with a pair of lasers at 493 nm and 650 nm we can cool single Ba$^+$ to millikelvin temperatures. Optical pumping with polarized light allows for ion state initialization with an efficiency of roughly 96%. By selectively shelving a single ground state to the $5D_{5/2}$ level and measuring the fluorescence from an ion we can perform state measurements. As discussed in the last chapter, we can drive transitions between Zeeman states by applying an rf current to a wire near the trap. These capabilities will allow us to perform a variety of experiments, which will be the subject of the remaining chapters.

Part III

RESULTS

Chapter 6

ADIABATIC RAPID PASSAGE

In this chapter we discuss our efforts to employ an adiabatic technique called adiabatic rapid passage (ARP) for driving state selective shelving transitions from the $6S_{1/2}$ level to the $5D_{5/2}$ level. Our efforts lead us to consider how the transfer efficiency of ARP is modified by noise in the driving field. However, first let's motivate consideration of ARP by contrasting it a simpler alternative: constant frequency excitation. Excitation of an atomic resonance by a field with a constant amplitude and frequency leads to the familiar phenomenon of Rabi oscillation (as covered in Chapter 1) wherein population is transferred sinusoidally back and forth between the two connected atomic levels as described by

$$P_1(t) = (\frac{\Omega}{W})^2 \sin^2 Wt/2, \tag{6.1}$$

where P_1 is the population in the excited state (labeled by 1), Ω is the resonant Rabi frequency, and W is the generalized Rabi frequency given by $W = \sqrt{\Omega^2 + (\omega - \omega_a)^2}$, in which ω_a is the frequency of the atomic resonance and ω is the frequency of the driving field. The atom is assumed to be in the ground state at time $t = 0$. For our purposes in this chapter, we note two features of this excitation method. First, maximal excitation is limited to $P_{1,\mathrm{max}} = (\Omega/W)^2$, so unless the resonance condition is met precisely, unit population transfer to the excited state is impossible. Second, since the Rabi frequency is proportional to the driving field amplitude, the degree of excitation for a given pulse duration depends on the intensity of the field as shown in Fig 6.1. Practically speaking, then, if one wishes to use resonant excitation for highly efficient population transfer one must control both the frequency and amplitude of the driving field precisely.

In order to make excitation robust against experimental imperfections, a host of adiabatic techniques have been developed and used in a variety of fields [66, 42, 62, 12, 55, 27]. The adiabatic technique to be discussed here is oxymoronically called adiabatic rapid passage. I say that the name is an oxymoron because adiabatic implies that the process is a

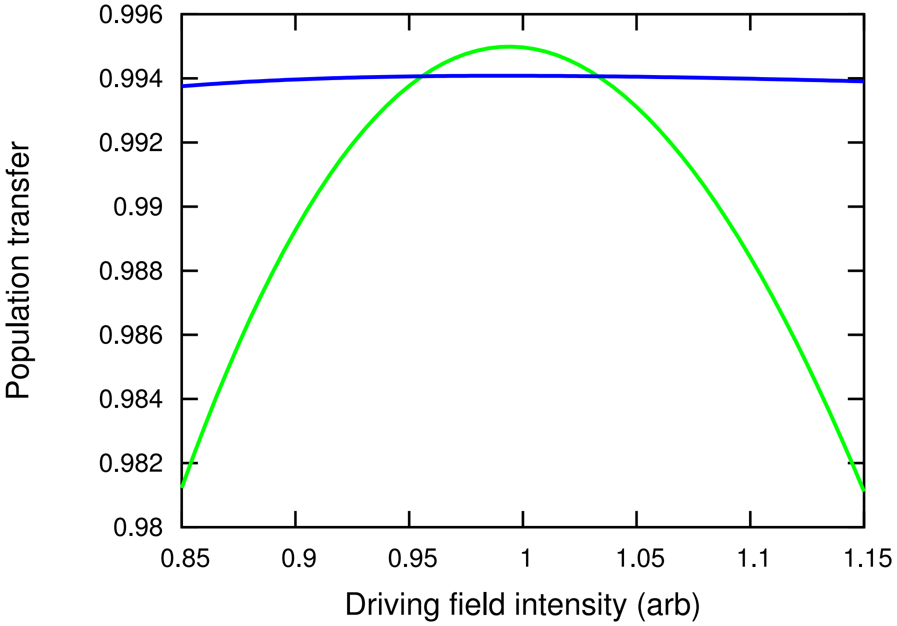

Figure 6.1: Comparison of the power dependence of constant frequency excitation versus excitation by ARP. The constant frequency excitation curve is shown in green and is based on the model including ion temperature that was introduced in a prior section. The population transfer plotted results from a constant excitation time corresponding to a π-pulse for an intensity of roughly 1. The blue curve is the population transfer resulting from ARP according to the Lacour model that will be discussed in the main text. Parameters in both models were chosen so that the maximum population transfer was roughly equal. The behavior as a function of intensity (near the maximum population transfer) doesn't depend strongly on the specific parameters chosen in either model, so the plot faithfully indicates the difference one can expect from constant frequency excitation versus an adiabatic technique.

slow one, and so the technique's name could be glossed as slow rapid passage. Really the "adiabatic" and "rapid" parts of the name are being compared to different timescales. The process is adiabatic with respect to the timescale of dynamics associated with the Hamiltonian in question, which is to say, slow compared to the Rabi frequency (we'll make this more concrete in a moment). However, the process is rapid with respect to some other timescale of interest, perhaps the time of flight of an atom through some region of space, the lifetime of an excited state, or the coherence time of the system. The idea behind ARP is to adiabatically deform the ion-laser Hamiltonian such that an ion in the ground state is tranferred to the excited state. Consider, once again, the Hamiltonian for the interaction of a laser with a two-level ion in the rotating wave approximation and in the basis of unperturbed ion states, Ψ_0 and Ψ_1,

$$H(t) = \frac{\hbar}{2} \begin{pmatrix} -\Delta(t) & \Omega(t) \\ \Omega(t) & \Delta(t) \end{pmatrix}, \tag{6.2}$$

where we have assumed that the Rabi frequency is real, and are allowing the Rabi frequency and detuning, ($\Delta = \omega_a - \omega$), to be functions of time [60, 62]. Now it will prove useful to introduce a new set of basis states which are the instantaneous eigenstates of $H(t)$ and are referred to as the adiabatic states, Φ_+ and Φ_-. They are defined as follows

$$\Phi_+(t) = \sin\theta(t)\Psi_0 + \cos\theta(t)\Psi_1 \tag{6.3}$$

$$\Phi_-(t) = \cos\theta(t)\Psi_0 - \sin\theta(t)\Psi_1, \tag{6.4}$$

where $\theta(t) = \frac{1}{2}\arctan\Omega(t)/\Delta(t)$, and their energies are

$$E_\pm(t) = \pm\frac{1}{2}\hbar W, \tag{6.5}$$

where W is again given by $\sqrt{\Omega^2(t) + \Delta^2(t)}$. For reference, I note that the definition of θ implies that

$$\sin\theta = \sqrt{\frac{W-\Delta}{2W}} \quad \text{and} \quad \cos\theta = \sqrt{\frac{W+\Delta}{2W}}. \tag{6.6}$$

First, we will employ the adiabatic theorem to avoid calculating the dynamics due to the changing Hamiltonian directly. The adiabatic theorem states that if a system is in an eigenstate of its Hamiltonian, then when changes are made to the Hamiltonian slowly (so that there is no coupling between the adiabatic states) the system will remain in the corresponding eigenstate of the changing Hamiltonian. More explicitly, in general if

$$\left| \left\langle \dot{\Phi}_+(t) \middle| \Phi_- \right\rangle \right| \ll |E_+ - E_-| \tag{6.7}$$

then the system will remain in the adiabatic state in which it began. In our case this requirement means that

$$\frac{1}{2}\left|\Delta\dot{\Omega} - \Omega\dot{\Delta}\right| \ll W^3 \tag{6.8}$$

Thus if we start with an ion in the ground state, Ψ_0, with the laser detuning negative and large with respect to the Rabi frequency, then θ will initially be roughly $\pi/2$ and the state of the system will be Φ_+. Then when we sweep the laser detuning slowly across the resonance until it is positive and large with respect to the Rabi frequency ($\theta \rightarrow 0$), the system will remain in Φ_+ and the ion state will have been transferred to the excited state Ψ_1 (because when $\theta = 0$, $\Phi_+ = \Psi_1$). This behavior makes intuitive sense when considered on the Bloch sphere. The initial condition that the ion is in the ground state means that the Bloch vector initially points at the south pole of the Bloch sphere. Since the detuning is intially negative and much larger in magnitude than the Rabi frequency, the interaction vector will also point nearly at the south pole. The solution to the optical Bloch equations tells us that the Bloch vector will precess around the interaction vector, and, as long as the detuning is changed slowly enough, this solution will be valid here as well. Therefore as the detuning changes from a large negative value to a large positive one, the interaction vector will creep slowly up past the equator toward the north pole and the Bloch vector will follow it finally coming to rest pointing at the north pole. Thus the frequency sweep will transfer the population to the excited state.

We would like a model of the ARP process that will make quantitative predictions about the population transferred as a function of the laser parameters. The Landau-Zener model is the simplest such model. It assumes that the Rabi frequency is constant and the laser detuning is swept at a constant rate, $\dot{\Delta} = \alpha$, from $\Delta = -\infty$ to $\Delta = +\infty$. Given these assumptions, the probability that the adiabatic passage is successful can be shown to be [69, 65]

$$P_{1,\mathrm{L-Z}} = 1 - \exp -\frac{\pi\Omega^2}{\alpha}. \tag{6.9}$$

So, provided that the frequency sweep rate is much smaller than the square of the Rabi frequency, the probability of a diabatic coupling is vanishingly small. This model has some obvious limitations in terms of practical applicability to experiment. While the lifetime of the metastable excited states in Ba$^+$are long lived, they won't survive the infinite duration of the Landau-Zener sweep. And while the available bandwidth of the 1.76 μm laser is large, it will have trouble reaching a detuning of infinity. However, the model will do a good job as long as the initial and final detunings are large compared to the Rabi frequency. This is usually not a difficult situation to arrange, since the practical limitation is that the frequency sweep shouldn't pass over any other spectral features and the nearest spectral features, the axial and secular frequency sidebands, are typically located at a detuning of at least several hundred kilohertz while our typical Rabi frequency is only about 100 kHz. If the nearest spectral features encroach on the transition of interest, the adiabaticity of the process can be saved by reducing the intensity of the laser at the expense of the speed of the ARP sweep. A variety of analytic solutions for other chirped pulse models exist. The Allen-Eberly model uses a hyperbolic secant time dependence for the Rabi frequency and a hyperbolic tangent time dependence for the detuning [1, 30]. A second limitation of the Landau-Zener model is that it does not account for dephasing. Consideration of dephasing makes the trade-off between adiabaticity and sweep rate less clear. Intuitively, if the driving field suffers from phase instability then a very slow sweep, while great for adiabaticity, will give the laser field plenty of time to grow out of phase with the ion resulting in incoherent and inefficient excitation. A model due to Lacour *et al.* [38] adds a dephasing rate, Γ, to the same pulse parameters as in the Landau-Zener model. With the inclusion of dephasing the probability of successful adiabatic passage becomes

$$P_{1,\mathrm{Lacour}} = \frac{1}{2}(1 - e^{-\pi\Gamma\Omega/\alpha}) + e^{-\pi\Gamma\Omega/\alpha} P_{1,\mathrm{L-Z}} \tag{6.10}$$

where $P_{1,\mathrm{L-Z}}$ is given by Eq. 6.9. When Γ goes to zero, we recover the Landau-Zener formula, but for non-zero Γ the transfer probability is limited to .5 for very slow sweeps. This is because, although the changes made to the Hamiltonian are fully adiabatic, the excitation is incoherent when the laser spends much longer than $1/\Gamma$ near resonance. Fig. 6.2 shows the transfer probability in the Lacour model as a function of the sweep rate for a variety of values of Γ/Ω. The figure shows that as the sweep rate becomes large, the transfer probability suffers as a result of non-adiabatic coupling

As was hinted at before, we are interested in employing ARP sweeps with the 1.76 μm laser for highly efficient population transfer from the ground state to the $5D_{5/2}$ level and the data presented here was previously presented in [49]. As discussed in Section 5, the 1.76 μm laser output is split into two beams. The first beam is sent to a cavity for frequency

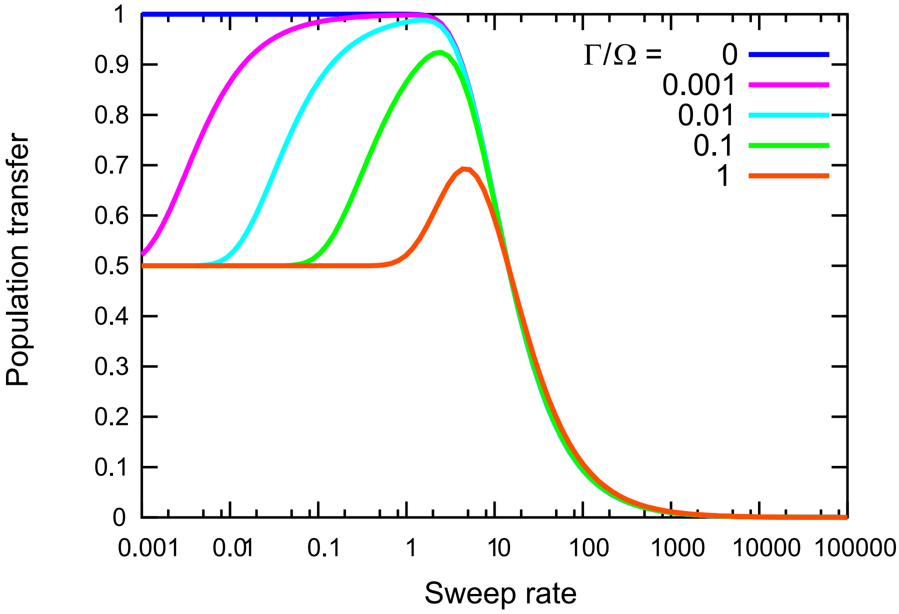

Figure 6.2: ARP population transfer as a function of sweep rate for a variety of ratios of dephasing rate to Rabi frequency. The Rabi frequency is set to 1 and the dephasing rate is varied in decades from 0.001 to 1. Additionally the zero dephasing, bare Landau-Zener result is plotted. In order to get a transfer probability of .99, the driving field must satisfy $\Gamma/\Omega \lesssim 0.001$.

stabilization and the second is sent through an AOM and to the ion. By adjusting the amplitude of rf to the AOM we can choose the laser intensity seen by the ion and by adjusting the rf frequency we can precisely tune the laser frequency. Furthermore, by applying chirped rf to the AOM we can write a frequency sweep onto the laser that will drive ARP. Initially we used an SRS DS345 sythesizer to generate the frequency sweeps necessary for ARP, but the minimum sweep duration it was capable of producing was 1 ms. This proved too long to fully probe the relevant parameter space of ARP for our system, so we switched to using a programmable DDS[1] capable of producing frequency sweeps of less than one microsecond in duration. The experimental sequence for investigation of ARP was as follows.

---

[1] Analog Devices 9910

(a) Doppler cooling

(b) Optically pump the ion to one of the ground states

(c) Apply an ARP sweep

(d) Turn on cooling lasers and check for fluorescence and record result

(e) Repeat (a-d) several times to build up statistics

(f) Change sweep parameters and repeat (a-e)

In this way we took the data that appears in Figs. 6.3, 6.4, and 6.5. Fig. 6.3 is a compilation of many data sets taken with a variety of sweep widths (the difference in frequency between the end and beginning of the ARP pulse) and sweep durations plotted as a function of the sweep rate, α. All are taken with roughly the same Rabi frequency, although, since the data was acquired over several weeks and without a complete set of accompanying measurements of the Rabi frequency, there is likely some ($\sim$10%) spread in the Rabi frequencies. All were taken with the frequency sweep centered on the atomic resonance. Note that the results confirm the prediction of both the Landau-Zener and Lacour models, that the population transfer due to ARP should depend only on the sweep rate, rather than on the sweep width or duration independently. The solid fit is to the Lacour model, Eq. 6.10, but with an overall scaling factor, F, to account for the imperfect optical pumping efficiency. The fit uses F, Ω, and Γ as free parameters and has a reduced χ^2 value of 1.5. The best fit values are $F = 0.96$, $\Omega = 2\pi \times 35$ kHz, and $\Gamma = 2\pi \times 110$ Hz. We identify Γ with the coherence time of the 1.76 μm laser. Assuming a Lorentzian laser noise spectrum, we can calculate the FWHM laser linewidth to be $\Delta_{\mathrm{FWHM}} = \Gamma/\pi \approx 35$ Hz. This bound on the laser linewidth is much better than that we had been able to derive from constant frequency excitation, since the decay in contrast of Rabi oscillations on the 1.76 μm transition is dominantly caused by the finite temperature on the ion rather than laser noise. Fig. 6.3, also includes a dotted line fit of the data with $\alpha > 2$ MHz/ms to the Landau-Zener formula. Note that laser noise results in dramatically reduced population transfer for slow sweeps where the

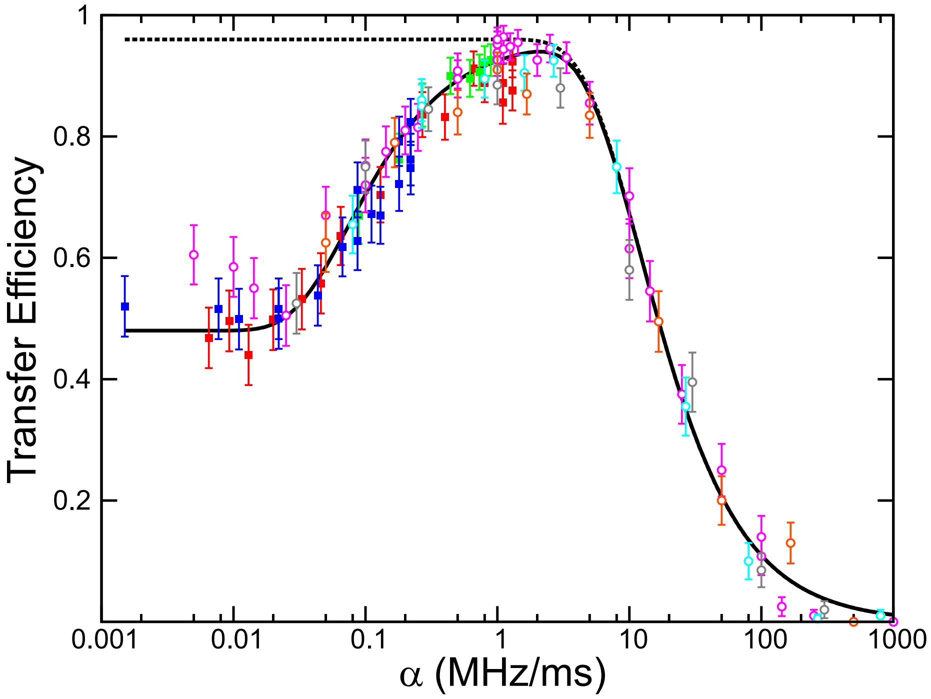

Figure 6.3: ARP transfer efficiency plotted as a function of the sweep rate. The solid square data points were taken with frequency sweeps provided by a DS345 Stanford Research Systems function generator. The open circle data points were taken using our homebuilt FPGA controlled DDS. The colors of the various data points correspond to different data sets, which were taken with a variety of sweep widths between 0.2 MHz and 1.2 MHz. The solid curve is a fit to the Lacour *et al.* model [38], while the dashed line is a fit to the data with $\alpha > 2$ using Landau-Zener theory [69]. The errorbars are statistical.

Landau-Zener formula would predict perfect population transfer. Given our system's laser linewidth and Rabi frequency, we find roughly optimal performance for sweep rates between .5 and 3 MHz/ms.

Some investigation of the dependence of ARP on Rabi frequency is shown in Fig. 6.4. Once again, it shows ARP transfer efficiency plotted against sweep rate, but now for a pair of Rabi frequencies. The Rabi frequency was measured by driving and fitting resonant Rabi oscillations before taking the ARP data. The two Rabi frequencies are $2\pi \times 43$ kHz and $2\pi \times 19$ kHz so the laser intensity differed by more than a factor of four between the two cases, yet the transfer efficiency near the plateau of maximum transfer efficiency at

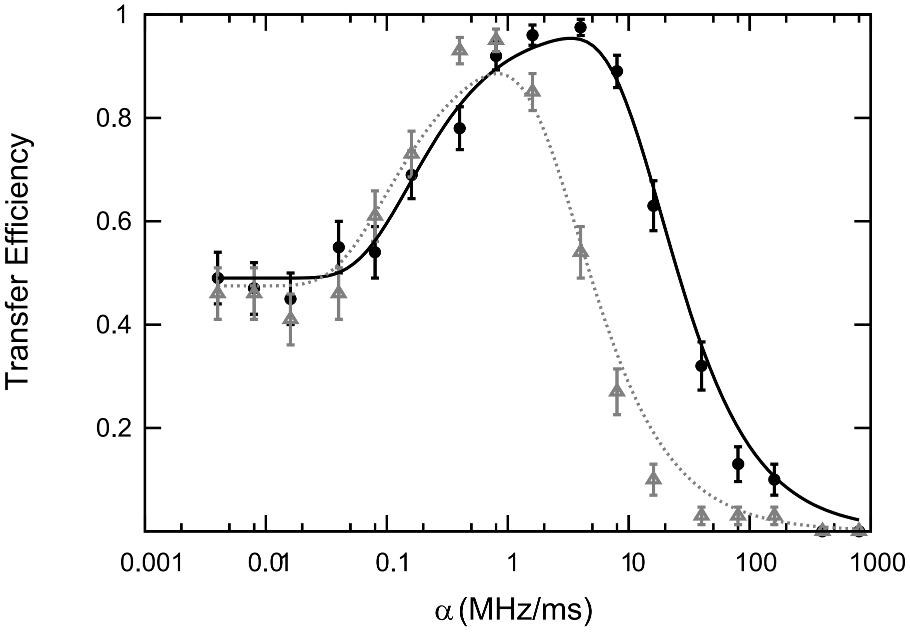

Figure 6.4: ARP transfer efficiency plotted as a function of sweep rate for a pair of quite different Rabi frequencies. The black circle (gray triangle) data points correspond to a Rabi frequency of $2\pi \times 43$ kHz ($2\pi \times 19$ kHz). The curves are fits to the Lacour model, with only F and Γ as free parameters. The black fit finds $F = 0.98$ and $\Gamma = 180$ Hz, while the gray fit finds $F = 0.95$ and $\Gamma = 260$ Hz. The errorbars are statistical.

$\alpha = 1$ MHz/ms barely changes. It is this insensitivity to laser intensity that makes ARP so robust against intensity noise and drifts in laser intensity that would be unacceptable when using π-pulses for population transfer. This robustness is useful for trapped ion experiments, but is even more important for atomic beam experiments where the intensity of a focused laser may vary widely across the profile of the atomic beam.

As was suggested earlier, the sweep width of an ARP pulse is limited by the detuning of the nearest spectral feature. For us this nearest spectral feature is the motional sideband associated with motion along the trap axis. For our typical trap parameters this frequency is hundreds of kilohertz, however, in labs that have worked to make extremely tight traps this frequency can be several megahertz. At the time of acquisition of the data presented in this chapter, the axial frequency was about 650 kHz. Fig. 6.5 is a composite figure that attempts to show multiple features associated with the sweep width of the ARP pulse. The

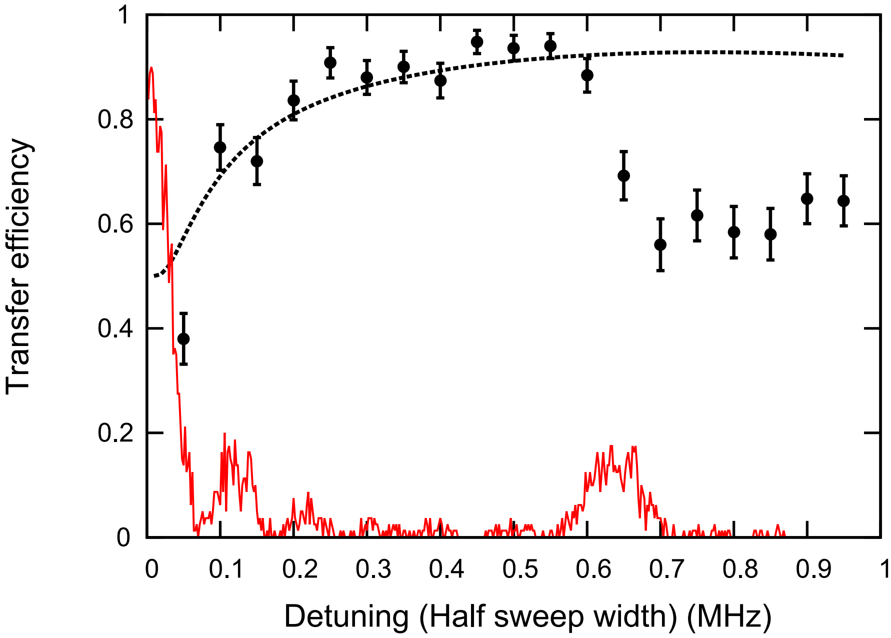

Figure 6.5: Effect of ARP transfer efficiency on sweep width in the presence of additional spectral features. The figure shows two different types of data overlaid. The red data is the excitation probability resulting from constant frequency excitation for a duration roughly corresponding to a π-pulse on resonance as a function of the detuning of the excitation. The substructure in the main resonant feature is due to coherent excitation and is well-modelled by Eq. 6.1. The secondary spectral feature at 650 kHz detuning is the sideband due to the motional frequency of the ion along the axis of the trap. Overlaid on this are a set of transfer probabilities due to ARP pulses, which are plotted at the frequency corresponding to half of the ARP sweep width. All ARP pulses have the same duration. Since all the ARP pulses also are centered on the resonance, the frequency at which the points are plotted also corresponds to the maximum detuning reached by the ARP pulse before it was turned off. Finally, the dashed line is a fit of the ARP data with half sweep width less than 600 kHz to the Lacour model. The figure shows the result of starting and stopping ARP sweeps too close to resonance and the effect of sweeping over additional spectral features as discussed in the main text.

data in red shows the result of constant frequency excitation with a pulse duration that is slightly less than a π-pulse when resonant. The probability that the ion was tranferred to the $D_{5/2}$ level as a result of the constant frequency excitation is plotted as a function of the detuning. On top of this are a set of black data points which are the probability of successful ARP. All ARP sweeps were centered on the atomic resonance and applied for a constant duration, but are plotted at the maximum frequency that the sweep reached, or, said another way, they are plotted at a detuning corresponding to half of the sweep width. The black dashed line corresponds to a fit to the Lacour model of the data with half sweep width less than 600 kHz, without any inclusion of the effect of the axial sideband. The first feature to note is the marked decline in ARP transfer when the sweep width is very narrow. This is the combined result of the non-adiabaticity of the ARP pulse and the reduction of transfer efficiency predicted by the Lacour model due to decreasing α. Since the duration of the ARP sweeps is constant across the plot, one might expect those very short sweeps to be the most adiabatic. After all, they will be the points with the minimum sweep rate. However, the more important feature is the non-adiabaticity associated with the sharp rising and falling edges of the sweep amplitude. For all data presented in this chapter we drive ARP roughly with intensity square pulses (the intensity profile is the result of sharply turning on and off the rf to an AOM, so there will be only some slight pulse rounding due to the switching behavior of the AOM itself). Thus if the sweep originates and terminates within a few Rabi frequencies of the resonance, those parts of the sweep will not be adiabatic and the models we are using (which assume infinite detuning sweeps) will not apply. The second feature to note is the reduction in ARP transfer efficiency when the sweep begins to cross the axial sidebands. The dashed line fit to the Lacour model is included to show that this decline is not due to the decreasing adiabaticity as the sweep widths increase. Rather the decline is due to the influence of the additional spectral features. This section may be leaving you feeling swindled by earlier claims that ARP transfer efficiency should not depend on the sweep width (provided sweep rate is held constant), but concentrating on the data points between 200 and 600 kHz will confirm the validity of the claim with the caveats discussed here.

In conclusion, ARP can be a useful tool for efficient population transfer given that the driving field has a high degree of coherence. Roughly we can suggest that in order to attain a transfer efficiency of 99%, the driving field must satisfy $\Omega/\Gamma \gtrsim 10^3$. Given that our system meets this rough requirement, ARP provides a nice means of desensitizing our state readout procedure from a variety of experimental imperfections. ARP transfer efficiency can be stable for days at a time without needing to tweak the excitation parameters. It is insensitive to laser frequency drifts on the order of tens to hundreds of kilohertz, as well as drifts (and noise) in laser intensity and changes in ion temperature. Given that many of our experiments are triggered to a single phase of the ac line and are thus limited to repitition rates of 60 Hz, the reduction of speed implied by using ARP rather than π-pulses for excitation is not a limiting factor. Furthermore, investigation of ARP provided a means of measuring the linewidth of the 1.76 μm laser. Fits to the Lacour model suggest that the dephasing time of the system is a few hundred hertz, allowing us to estimate that the linewidth of the 1.76 μm laser is $\approx$100 Hz.

Chapter 7

LANDÉ $g_{D_{5/2}}$ MEASUREMENT

When we added the dedicated electrode for applying rf magnetic fields, our intention was to enable rotations of the ground state Zeeman qubit. It turned out to additionally enable a much more sensitive measurement of the Landé g factor of the $5D_{5/2}$ state, since we could now directly drive transitions between Zeeman states rather than relying on extracting the g factor from measurements of 1.76 μm transition frequencies. The linewidths of the Zeeman transitions are limited by the stability of the local magnetic field, which turned out to be more unstable than one would expect due to unbalanced currents in the power lines that supply power to the electric buses passing the building. Even so, a much improved g factor measurement was both possible and useful, since it would facilitate the measurement of the hyperfine intervals of the $5D_{5/2}$ level in $^{137}\mathrm{Ba}^{+}$, a project being conducted here by Matt Hoffman. Matt's initial measurements (by rf spectroscopy in a different trap) found a value for the $5D_{5/2}$ g factor that differed from previous measurements (Kurz *et al.* [36]) by about 1%, a much greater discrepancy than the statistical error on either measurement. This discrepancy piqued my interest to get involved and culminated in a joint measurement by Matt and I [31]. Further consternation ensued when my initial measurements agreed with neither Matt's new measurement nor the previous measurement in Kurz *et al.*, although my measurement came much closer to the Kurz *et al.* value. The resolution involved dealing with a large ac Zeeman systematic in Matt's trap and the removal of outlying points in the Kurz *et al.* value, when every value came to agree with mine. From here I will primarily discuss the measurements made in my trap, but much of the discussion will follow that found in [31].

We used radiofrequency spectroscopic measurements of the Zeeman splittings in the ground and $5D_{5/2}$ levels to extract the $5D_{5/2}$ g factor. The experimental sequence for the measurement of the $5D_{5/2}$ Zeeman splitting was as follows.

(a) Doppler cool the ion on the 493 nm and 650 nm transitions for approximately 20 ms

(b) Use the optical pumping beam to pump the ion into the $6S_{1/2}$ $(m = -1/2)$ sublevel in roughly 10 μs

(c) Extinguish the 493 nm and 650 nm beams, and drive the ion to the $5D_{5/2}$ $(m = -5/2)$ sublevel using an ARP sweep with the 1.76 μm laser

(d) Apply a constant frequency pulse of rf magnetic field, triggered on a specific phase of the 60 Hz ac voltage is then applied (the importance of this line trigger will be discussed later in the section on systematics)

(e) Sweep the 1.76 μm laser again.

(f) Turn on the cooling lasers and record the fluorescence state of the ion. If a transition between the $5D_{5/2}$ Zeeman sublevels was driven by the rf pulse, the ion would remain in the $5D_{5/2}$ state and would be dark. However, if no transition occurred, the ion would be returned to the $6S_{1/2}$ state and appear bright.

(g) Deshelve the ion if necessary

(h) Repeat (a-g) several (usually 50-100) times to build up statistics

(i) Vary the frequency of the applied rf magnetic field and repeat (a-h) until a resonance frequency, $f_{D_{5/2}}$, is found

In a similar way, but with need for only a single ARP sweep, the Zeeman transition frequency of the ground state, $f_{S_{1/2}}$, is measured.

In Fig. 7.1, we show the results of rf spectroscopy in the ground and $5D_{5/2}$ levels. The figure shows the probability of finding the ion to be dark after a procedure like that described in the previous paragraph plotted against the frequency of the applied rf magnetic field. The curves are fits to a standard Rabi oscillation formula:

$$P_{\mathrm{dark}} = \alpha + \beta \frac{\Omega^2}{W^2} \sin^2 \left[W \frac{t}{2} \right] \tag{7.1}$$

where $W^2 = \Omega^2 + (2\pi(f - f_0))^2$. The four fit parameters are two scaling factors, α and β, which account for imperfect transfer efficiency with the 1.76 μm laser and imperfect optical pumping, the Rabi frequency of the transition, Ω, and the resonance frequency, f_0. This fit function is appropriate for coherent excitation with a square pulse, although fitting to a Lorentzian or Gaussian profile yields a fitted resonance frequency that agrees within the statistical uncertainty.

To calculate the Landé g factor of the $5D_{5/2}$ state, $f_{S_{1/2}}$ and $f_{D_{5/2}}$ must be measured in quick succession to counter the effects of fluctuations in the ambient magnetic field. As discussed in the first chapter, the resonance frequency of Zeeman transitions in each level is given by:

$$f_i = \frac{1}{h} g_i \mu_B B \tag{7.2}$$

where h is Planck's constant, μ_B is the Bohr magneton, and B is the magnitude of the magnetic field seen by the ion. Given measured resonance frequencies, $g_{D_{5/2}}$ can be calculated from:

$$g_{D_{5/2}} = g_{S_{1/2}} \frac{f_{D_{5/2}}}{f_{S_{1/2}}}, \tag{7.3}$$

assuming that the magnetic field remains constant over the duration of the experiment. The experimentally measured value of $g_{S_{1/2}}$ is 2.002 490 6(11) [34]. Since we lack any means of co-magnetometry in the Paul trap, we rely on this Penning trap measurement to extract an absolute value for the $5D_{5/2}$ g factor. Given magnetic shielding and careful consideration of other systematics, we could perhaps vastly improve our measurement of the ratio of $g_{S_{1/2}}$ to $g_{D_{5/2}}$, but we would be unable to say anything more precise about either g factor independently.

Using Eq. 7.3, each pair of Zeeman resonance measurements allows us to calculate the $5D_{5/2}$ g factor. The results of all measurements done in both my trap and Matt's trap are shown in Fig. 7.2. The points are shown with a combined statistical and systematic uncertainty. The statistical uncertainties come from the fitting procedure and ultimately from the binomial uncertainty on each data point in data like that shown in Fig. 7.1. Systematic uncertainties will be discussed shortly. Also included in the figure is a black horizontal line at the weighted mean value of $g_{D_{5/2}} = 1.200\ 372$ and the gray band is a combined 1-σ confidence interval.

7.1 Systematic effects

As in any precision measurement (depending on your point of view a ppm measurement may or not deserve the title), consideration of systematic effects is crucial. The fact that the spectroscopy done here is on magnetically sensitive transitions points to what will likely be the dominant systematic effect: drifts in the magnetic field seen by the ion. In addition to drifts in the field, we consider the effects of 60 Hz power line related magnetic fields, magnetic field gradients in the trap, and ac Zeeman related effects.

Since the power line current drawn by every piece of lab equipment oscillates in phase at 60 Hz, we expect that the ion should see some magnetic field at that frequency. To measure the size of this 60 Hz field, I measured the ground state splitting as a function of the delay from a line trigger. The result of this measurement is shown in Fig. 7.3. The fitted amplitude is about 7 kHz peak to peak which corresponds to a 60 Hz magnetic field of about 2.5 mG peak to peak. Because many pieces of electronics have been shuffled around in the vicinity of the trap since this measurement was done, it is unlikely that the current 60 Hz magnetic field is still 2.5 mG, but it is also unlikely to be very much different. This is much too large an effect to be ignored, for instance if the ac phase at which the $6S_{1/2}$ and $5D_{5/2}$ resonances were measured were very different then the magnetic field at which they were measured could be different by up to 2.5 mG, whereas the precision on our measurement corresponds to a field sensitivity on the order of 10 μG. To ensure that 60 Hz magnetic fields would not contaminate our results we set the timing of both resonance measurements to occur at the maximum of the ac field by using a line trigger and a programmed delay. Still one could worry that the changing field (and jitter in the line trigger) could lead to a broadening of the resonance features. Given the amplitude of the 60 Hz field and the fact that we used 300 and 500 μs rf pulses to interrogate the Zeeman transitions, we can expect a broadening of the transition resonances of only about 20 Hz. The jitter in the line trigger is about 10 μs, which implies a broadening of less than one hertz.

If the ion's position changes, then the presence of a magnetic field gradient could affect the accuracy of the g factor measurement. There is no reason to think that the ion's position should change, and less reason to think that it should change systematically between measurements of the ground and D level splittings. Nonetheless, we took care to measure the local magnetic field gradient (along the trap axis) at the ion and monitored the position of the ion before and after each data run. The magnetic field gradient at the ion postion was measured to be 1.4 nT/μm, while the ion moved by less than one micron (better precision that this is difficult to claim by monitoring the ion position with our imaging system) from run to run. Thus the effect of magnetic field gradients can be safely claimed to introduce a systematic uncertainty in our g factor measurement of less than 10 ppm, and likely is quite a lot less.

The presence of the rf oscillating field that produces the trapping potential can contaminate the g factor measurements through the ac Zeeman effect. This can arise either directly from interaction with oscillating magnetic fields due to currents in the trap electrodes or from micromotion along a magnetic field gradient, which will also produce an effective oscillating magnetic field at the trap frequency. Either possibility will depend on the trapping potential, so that if the trap strength is changed the degree of frequency shift due to the ac Zeeman effect should change too. In order to ensure that our results were not skewed by this effect, we took data at a pair of trap voltages differing by more than a factor of two. The values of the g factor derived at each trap voltage are indistinguishable, as shown in Fig. 7.2 (the different colors correspond to data taken with different trap voltages). Thus we can place a limit on the systematic uncertainty due to the ac Zeeman effect at 1 ppm.

Detuned laser fields can introduce small shifts in the Zeeman splittings through the vector ac Stark effect. The tiny levels of leakage light of all our laser beams combined with their detunings leads us to estimate that the vector ac Stark effect adds a systematic uncertainty below the 1 ppm level.

Finally, the major source of uncertainty comes from fluctuation in the ambient magnetic field on the timescale of the time it takes to do the resonance measurements. The largest source of magnetic field fluctuations turned out to be from the current drawn by electric buses passing the building that houses our laboratory. To get a handle on the effect of magnetic field fluctuations, I measured the ground state splitting repeatedly for a while after having taken the data that would go into my portion of the g factor measurement. The result of these repeated measurements are shown in Fig. 7.4. We can use the standard deviation of the measurements in Fig. 7.4 (and other similar data) to derive a better estimate of the uncertainty on each individual resonance frequency measurement and then propagate that uncertainty on to the calculated g factor value. This implies that the uncertainty on each indivicual measurement of the $5D_{5/2}$ g factor value is more like 40 ppm. However, since the fluctuations appear to be random without a significant drift, different measurements will have uncorrelated error and so the overall uncertainty due to magnetic field flucutations can be reduced by making multiple measurements. These systematic uncertainties are summarized in Table 7.1. After consideration of all these systematic effects we are finally able to report that the g_J-factor of the $5D_{5/2}$ level is $1.200\ 371(4)_{\text{stat}}(7)_{\text{sys}}$.

Error Source	$\Delta g_{D_{5/2}}$ Matt	$\Delta g_{D_{5/2}}$ Tom
B Fluctuations	1.3×10^{-5}	4.6×10^{-5}
B Gradient	1×10^{-5}	1×10^{-5}
ac Zeeman Effect	10^{-6}	10^{-6}
ac Stark Effect	$< 10^{-6}$	$< 10^{-6}$
60Hz Jitter	10^{-7}	$< 10^{-7}$
Total	1.6×10^{-5}	4.7×10^{-5}

Table 7.1: A summary of systematic error estimates for our experimental apparatuses.

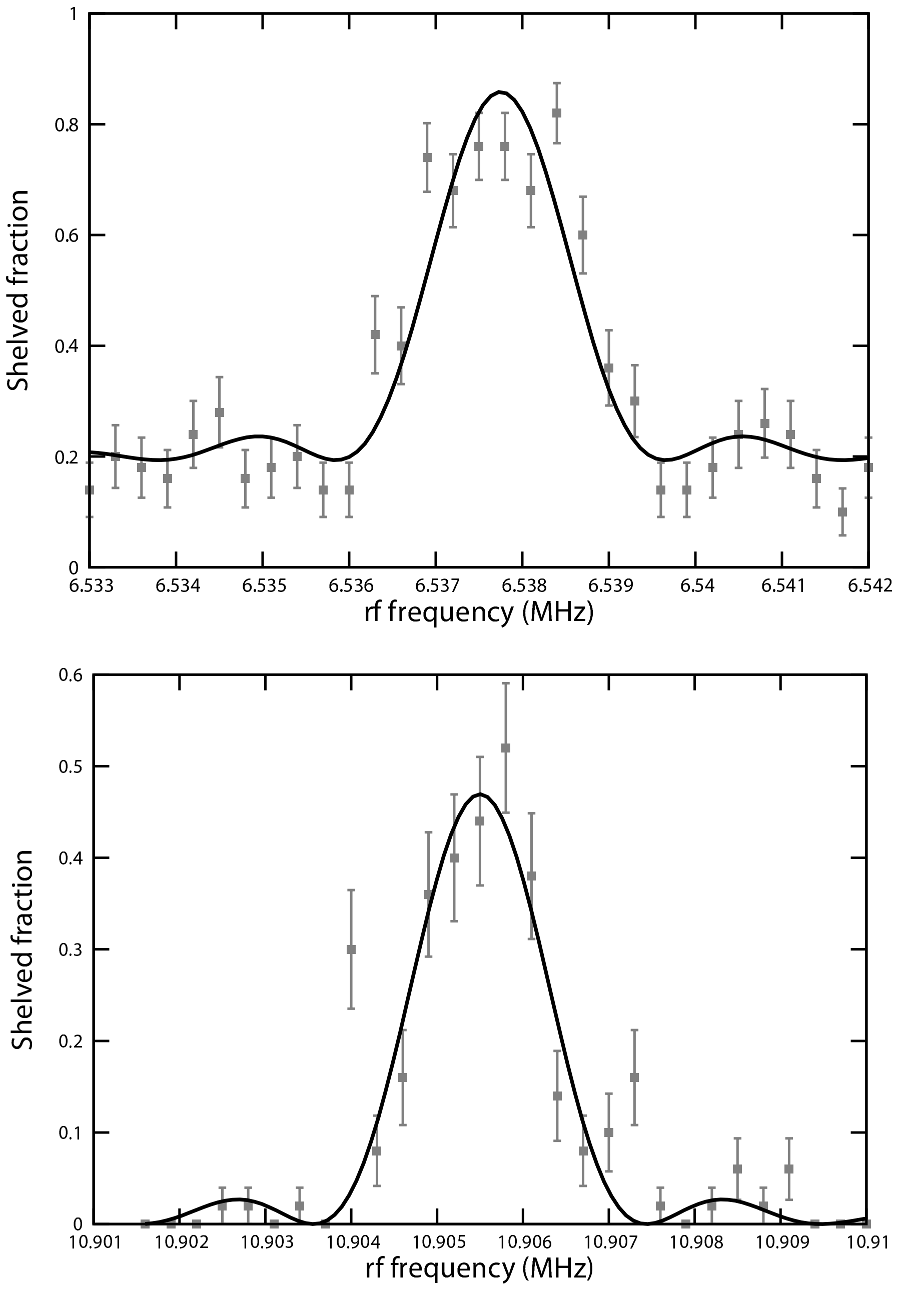

Figure 7.1: rf spectroscopy of Zeeman transitions in the $6S_{1/2}$ and $5D_{5/2}$ levels. The shelved fraction of the ions is plotted against the frequency of the applied rf magnetic field. The upper plot shows the $5D_{5/2}$ resonance, and the bottom shows the $6S_{1/2}$ resonance. Statistical error bars are shown, calculated from a binomial distribution based on 50 trials at each frequency. A least-squares fit function based on Eq. 7.1 is overlaid. The fitted values of the resonance frequencies are 6.537 75(7) MHz with a reduced χ^2 of 1.7 for the upper plot and 10.905 57(9) MHz with a reduced χ^2 of 2.2 for the lower plot.

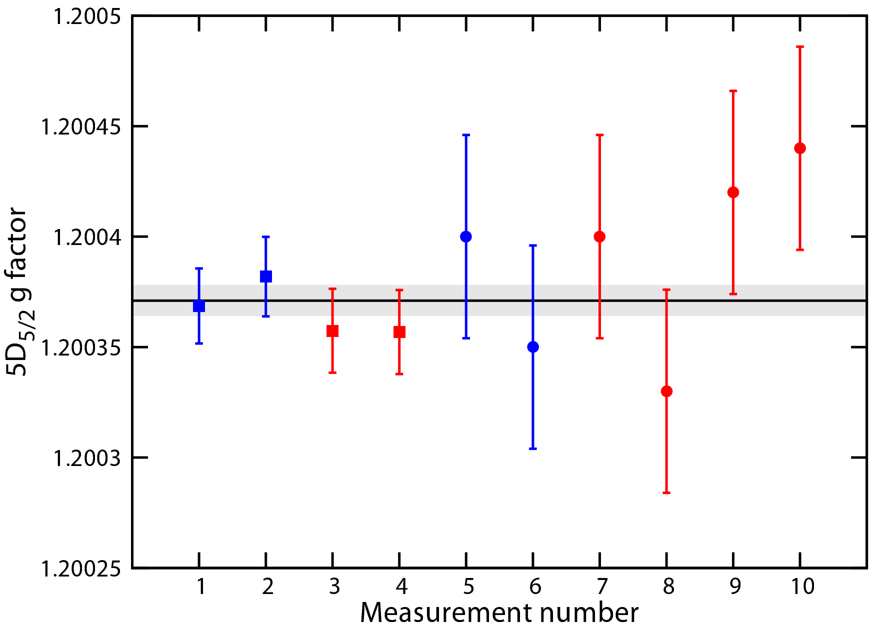

Figure 7.2: Summary of measurements of the Landé g factor of $5D_{5/2}$. The 10 measurements of $g_{D_{5/2}}$ are shown with squares for the Matt's apparatus, and circles for mine. The blue and red colors indicate different trap depths, which should manifest an ac-Zeeman effect as will be discussed in the section on systematics. The error bars represent calculated 1-σ total uncertainties (statistical and systematic). It should be noted that the mean values measured in each apparatus agree with each other within 1-σ. A solid line represents the weighted mean of all of the measurements done in both apparatuses, with a 1-σ confidence interval.

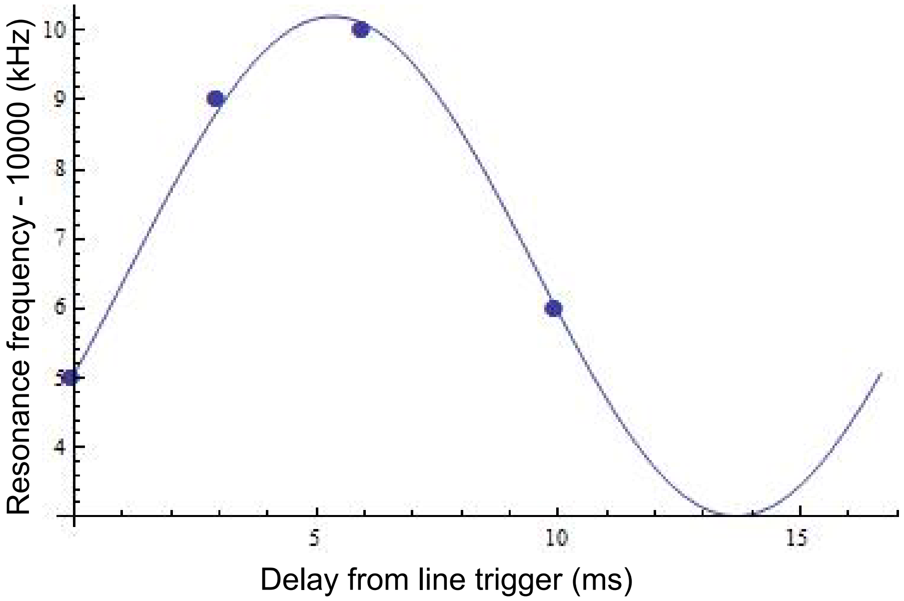

Figure 7.3: Measurement of the 60 Hz ac line related magnetic field seen by the ion. Offset in kHz of the ground state splitting from 10 MHz is plotted against the phase of the 60 Hz ac line at which the splitting was measured. The fit is to a 60 Hz sinusoid and finds that the 60 Hz magnetic field seen by the ion is roughly 2.5 mG peak to peak.

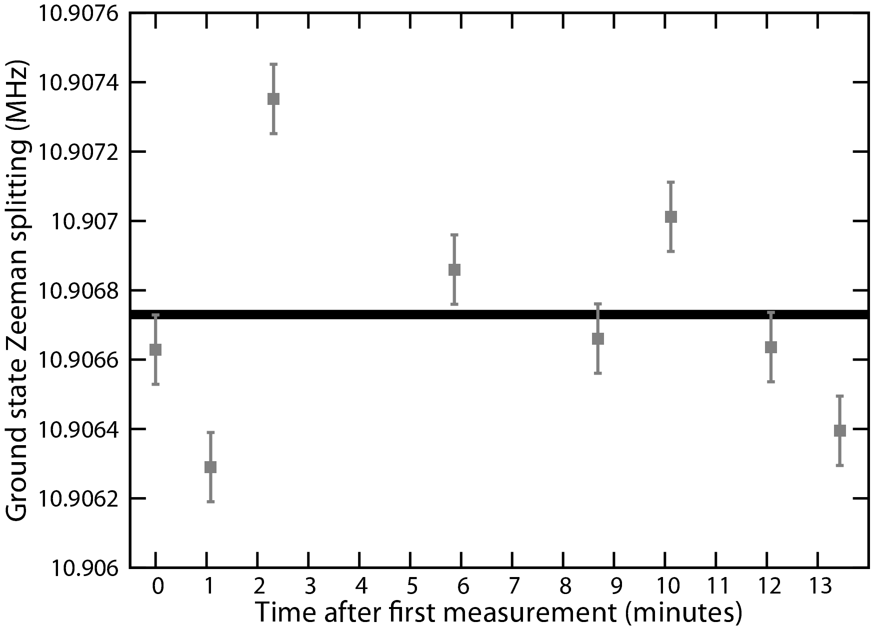

Figure 7.4: Repeated measurements of the ground state Zeeman splitting. The spread in the measurements is a bit larger than the statistical uncertainty on each measurements would suggest, implying that there is some real fluctuation in the ambient field on this timescale.

Chapter 8

ION-PHOTON ENTANGLEMENT

Chapter 3 examined the theoretical background for a Bell measurement, and here we will discuss our experimental efforts to demonstrate ion-photon entanglement and measure Bell inequality violation. As was mentioned in Chapter 3, in order to measure the CHSH Bell signal one must have access to an ensemble of pairs of entangled pseudo-spins and the ability to measure them in multiple bases. In our experiment, entangled states of single $^{138}\mathrm{Ba}^{+}$ and single photons spontaneously emitted by the ion will be prepared. Specifically the entanglement will be between the polarization state of the photons and the resulting ground state of the ion after the photon has been emitted. The photon polarization can be measured in different bases simply by inserting a $\lambda/2$ wave plate before a polarizing beamsplitter and detecting the photon at the two output ports of the beamsplitter with a pair of PMTs. The ion state can be measured, as has been discussed previously, by selectively shelving one of the ground states to the $5D_{5/2}$ level and measuring the fluorescence state of the ion. Ion measurement basis rotations can be effected by applying an rf magnetic field to the ion that is resonant with the ground state splitting. This field is applied by driving an rf current through a wire placed near the trap. A schematic representation of the apparatus that shows these features can be found in Fig. 8.1. Now that we have seen that we have the general features necessary to measure the CHSH Bell signal, let's first discuss what measurements we will need to make, consider the experimental procedure necessary to make those measurements, and finally take a look at some results. The experimental results discussed here are reported in [4] and follow in the footsteps of a long line of related theoretical inquiry and experiments showing Bell inequality violation in a variety of systems [3, 26, 51, 39, 8, 57, 46, 52, 2, 11].

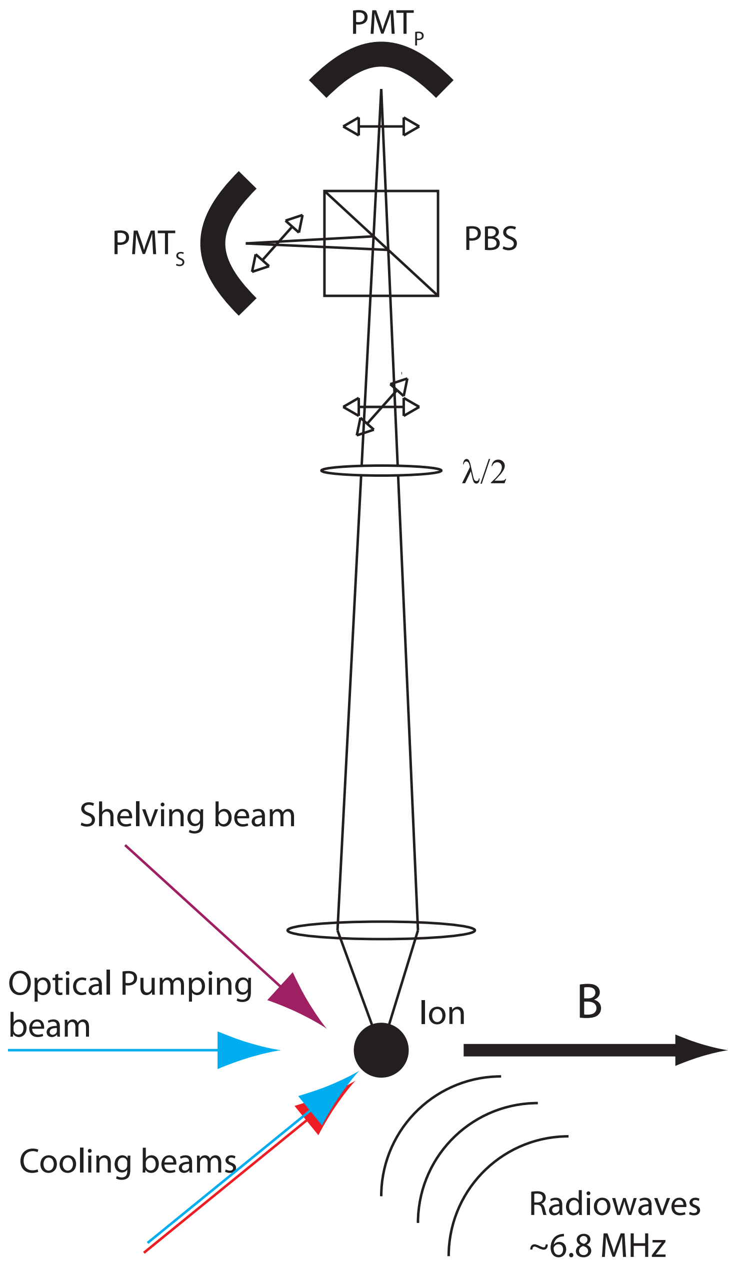

Figure 8.1: Schematic representation of the apparatus necessary for our ion-photon entanglement experiment. Cooling beams at 493 nm and 650 nm are incident on the ion. A second 493 nm beam is circularly polarized and directed along the ion's quantization axis in order to drive only $\Delta m = 1$ transitions for optical pumping. Finally, a laser at 1.76 μm drives transitions to the $5D_{5/2}$ shelved level. An rf magnetic field at the ground state splitting (here 6.82 MHz) can be applied to drive transitions between the ground states. Spontaneously emitted photons from the ion are collected with an objective lens and sent through a $\lambda/2$ wave plate on their way to a polarizing beamsplitter. A pair of PMTs (labeled by the photon polarization they will detect) are situated at the output ports of the beamsplitter.

Let's consider exactly what measurements we need to make in order to demonstrate that we have produced an entangled ion-photon state. A simple measure of the entanglement fidelity of a system of two psuedo-spins is the overlap of the state with any of the maximally entangled Bell states. To facilitate the following discussion I will use the following key for labeling the ion and photon states, with the physical qubit states on the left, computational basis shorthand labels in the center, and corresponding measurement outcome[1] on the right.

$$\begin{array}{rcccl} \left|6S_{1/2}(m=-1/2)\right\rangle & \leftrightarrow & \left|0\right\rangle_{\text{ion}} & \leftrightarrow & \left|\text{dark}\right\rangle \\ \left|6S_{1/2}(m=+1/2)\right\rangle & \leftrightarrow & \left|1\right\rangle_{\text{ion}} & \leftrightarrow & \left|\text{bright}\right\rangle \\ \left|\pi \text{ polarization}\right\rangle & \leftrightarrow & \left|0\right\rangle_{\text{photon}} & \leftrightarrow & \left|\text{P}\right\rangle \\ \left|\sigma \text{ polarization}\right\rangle & \leftrightarrow & \left|1\right\rangle_{\text{photon}} & \leftrightarrow & \left|\text{S}\right\rangle \end{array} \tag{8.1}$$

Given this key, the entangled state we prepare will look most similar to the $\left|\Phi^+\right\rangle$ Bell state:

$$\left|\Phi^+\right\rangle = (\left|0\right\rangle_{\text{ion}}\left|0\right\rangle_{\text{photon}} + \left|1\right\rangle_{\text{ion}}\left|1\right\rangle_{\text{photon}})/\sqrt{2}. \tag{8.2}$$

Since we collect only a small solid angle ($\Delta\Omega/4\pi \sim .02$) perpendicular to the quantization axis, the π and σ polarized spontaneously emitted photons that we collect will be linearly polarized and orthogonal to a good approximation, although there will be twice as many π-polarized photons along that direction[2]. Therefore the ideal ion-photon entangled state that we will produce is

$$\left|\Psi\right\rangle = \frac{1}{\sqrt{3}}\left|0\right\rangle_{\text{ion}}\left|0\right\rangle_{\text{photon}} + \sqrt{\frac{2}{3}}\left|1\right\rangle_{\text{ion}}\left|1\right\rangle_{\text{photon}}. \tag{8.3}$$

This gives the maximum possible entanglement fidelity we could measure to be

$$\begin{aligned} F &= \left|\left\langle\Psi\right|\left.\Phi^+\right\rangle\right|^2 \\ &= \left|\Big(\frac{\left\langle 0\right|_{\text{ion}}\left\langle 0\right|_{\text{photon}}}{\sqrt{3}} + \frac{\left\langle 1\right|_{\text{ion}}\left\langle 1\right|_{\text{photon}}\sqrt{2}}{\sqrt{3}}\Big)\Big(\frac{\left|0\right\rangle_{\text{ion}}\left|0\right\rangle_{\text{photon}}}{\sqrt{2}} + \frac{\left|1\right\rangle_{\text{ion}}\left|1\right\rangle_{\text{photon}}}{\sqrt{2}}\Big)\right|^2 = .97. \end{aligned} \tag{8.4}$$

---

[1] The ion measurement outcome listed in the key is the fluorescence state of the ion after shelving given no ion measurement basis rotation. For the photon, we list the output port of the beamsplitter taken by π or σ polarized emitted photons given the $\lambda/2$ setting for maximum ion-photon state correlation. Note that there is a large degree of arbitrariness to this key. In particular, the choice of computational basis labelling is completely arbitrary and, since there are periodic $\lambda/2$ settings that give nearly the same ion-photon correlations the roles of S and P could be switched by using a different wave plate setting. Furthermore, we could choose to shelve the $m = +1/2$ ground state (although we didn't for the data shown here) and so the roles of "dark" and "bright" could also be reversed.

[2] This is because of the dipole radiation patterns: $\left|\sigma^-\right\rangle = (e^{-i\phi}/\sqrt{2})(\cos(\theta)\left|\hat{\theta}\right\rangle - i\left|\hat{\phi}\right\rangle)$ and $\left|\pi\right\rangle = -\sin(\theta)\left|\hat{\theta}\right\rangle$. So perpendicular to the quantization axis ($\theta = \pi/2$), the polarizations are linear and orthogonal, and have a difference in intensity of a factor of 2.

However, there are a variety of experimental imperfections that will reduce the fidelity, as we will discuss shortly, and so we must describe the ion-photon state by a density matrix rather than as a known pure state ket. We will use the computational basis, $\{|00\rangle, |01\rangle, |10\rangle, |11\rangle\}$, to describe the ion-photon density matrix, ρ. In this basis, the entanglement fidelity looks like

$$F = \left\langle \Phi^+ \right| \rho \left| \Phi^+ \right\rangle = \frac{1}{2}(\rho_{11} + \rho_{44} + \rho_{14} + \rho_{41}). \tag{8.5}$$

The diagonal terms, ρ_{11} and ρ_{44}, are state populations easily measured via ion-photon state correlation probabilities, whereas the off-diagonal coherences require a little extra work. To be precise, ρ_{ii} ($i \in \{1, 2, 3, 4\}$) is the probability of measuring the ion to be in the state corresponding to i multiplied by the conditional probability of detecting the photon in the state corresponding to i given that the ion is in the state corresponding to i. We can immediately set an upper bound on the fidelity by noting that $2\sqrt{\rho_{11}\rho_{44}} \geq \rho_{14} + \rho_{41}$, which implies that the fidelity is bounded by

$$F \leq \frac{1}{2}(\sqrt{\rho_{11}} + \sqrt{\rho_{44}})^2. \tag{8.6}$$

However, a lower bound on the fidelity would be more experimentally interesting and so we must find a different way of looking at ρ_{14} and ρ_{41}. The coherences can be determined by rotating the states of both the ion and the photon and once again measuring the populations. If the ion and photon states are each rotated through a polar angle of $\pi/2$ on the Bloch sphere, the rotated density matrix will be given by $\tilde{\rho} = R(\frac{\pi}{2})\rho R^\dagger(\frac{\pi}{2})$ and by inspection we find that

$$\begin{aligned} \rho_{14} + \rho_{41} &= \tilde{\rho}_{11} + \tilde{\rho}_{44} - \tilde{\rho}_{22} - \tilde{\rho}_{33} - \rho_{23} - \rho_{32} \\ &\geq \tilde{\rho}_{11} + \tilde{\rho}_{44} - \tilde{\rho}_{22} - \tilde{\rho}_{33} - 2\sqrt{\rho_{22}\rho_{33}}, \end{aligned} \tag{8.7}$$

where we used a similar inequality to that used above. It follows that we get a lower bound on the fidelity of the entangled state in terms of the populations of the original and rotated density matrices,

$$F \geq \frac{1}{2}(\rho_{11} + \rho_{44} - 2\sqrt{\rho_{22}\rho_{33}} + \tilde{\rho}_{11} + \tilde{\rho}_{44} - \tilde{\rho}_{22} - \tilde{\rho}_{33}). \tag{8.8}$$

So in order to put a bound on the fidelity of the entangled state, we must measure the populations of the ion-photon density matrix (which are given by conditional probabilities as detailed above) in an unrotated basis and after rotating both the ion and photon states by $\pi/2$.

The experimental sequence for the production and measurement of the entangled ion-photon state consists of a fast loop whose purpose is to produce a single spontaneously emitted photon and ion state measurement steps which only occur in the event that the spontaneously emitted photon was detected. This is necessary since the probability to detect the photon in any given cycle of the experiment is very low due primarily to the small solid angle of fluorescence collection (2%), but also to a variety of other losses. By far the slowest step in the experimental sequence is the detection of the ion state, so for the experiment to procede as rapidly as possible we want to avoid doing ion state detection unless it is useful. The sequence, also shown in cartoon form in Fig. 8.2, is as follows:

(a) Doppler cooling

(b) Initialize the ion state by first optically pumping the ion to the $6S_{1/2}(m = -1/2)$ state and then applying a π-pulse of rf magnetic field resonant with the ground state splitting to transfer the ion to the $6S_{1/2}(m = +1/2)$ state

(c) Apply a short (20 ns) pulse of light from the optical pumping beam to weakly excite ($\approx$20%) the ion to the $6P_{1/2}(m = -1/2)$ state

(d) Gate the PMTs for a brief window (20 ns) to detect the spontaneously emitted photon

(e) If a photon was detected, then perform state detection on the ion by selectively shelving the $m = -1/2$ ground state and measuring the fluorescence state of the ion, then go back to (a). If no photon was detected go back to (a) without detecting the ion state

(f) Once a sufficient number of events (typically 100-1000) have been recorded at a given set of apparatus parameters ($\lambda/2$ setting, ion basis rotation angle and phase), vary the apparatus parameters and repeat (a-e)

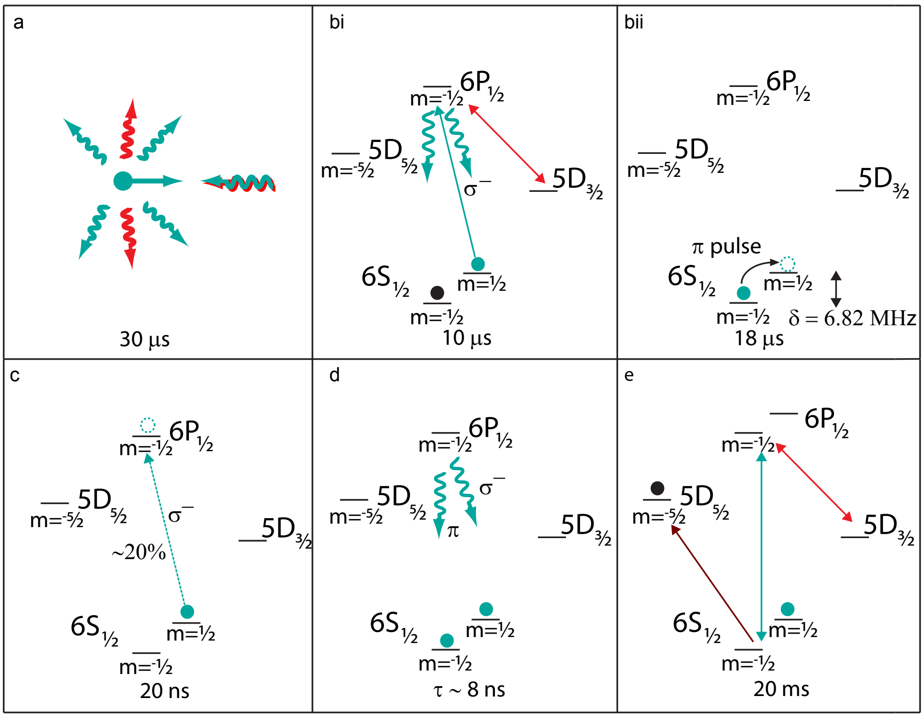

Figure 8.2: Cartoon depiction of the ion-photon entanglement experimental cycle. Letter labels correspond to the list in the main text. First the ion is Doppler cooled, then the state is initialized by optical pumping followed by a ground state π-pulse. The ion is weakly excited with a short pulse from the optical pumping beam, and the PMTs are gated to detect the resulting spontaneously emitted photon. If a photon is detected then the ion state is measured.

In order to ensure that the ion stays cool enough for all the other steps to be performed reliably, we typically set the duration of Doppler cooling to about 50% of the duration of the fast loop. For the results to be presented shortly this means that we Doppler cool for 30 μs. At first glance the state initialization procedure outlined above seems unnecessarily complicated, why not just use optical pumping to initialize the ion in the $m = +1/2$ in the first place? The answer is that if we want to use the same beam for optical pumping and weak excitation, then we had better remove the ion from the dark ground state before we try to excite it. The optical pumping step can be performed in less than 3 μs when the system is well tuned. Here we optically pump for 10 μs to ensure reliability.

As shown in Fig. 8.3, we can acheive a π-time of about 600 ns on the transition between the ground states by applying 50 W of rf to the dedicated electrode near the trap. In the experiment we unfortunately could not take advantage of this fast π-time since something about the application of such a large field with a high repetition rate caused the ion to heat up significantly[3]. Therefore we reduced the applied rf field amplitude slowing the π-time to 18 μs.

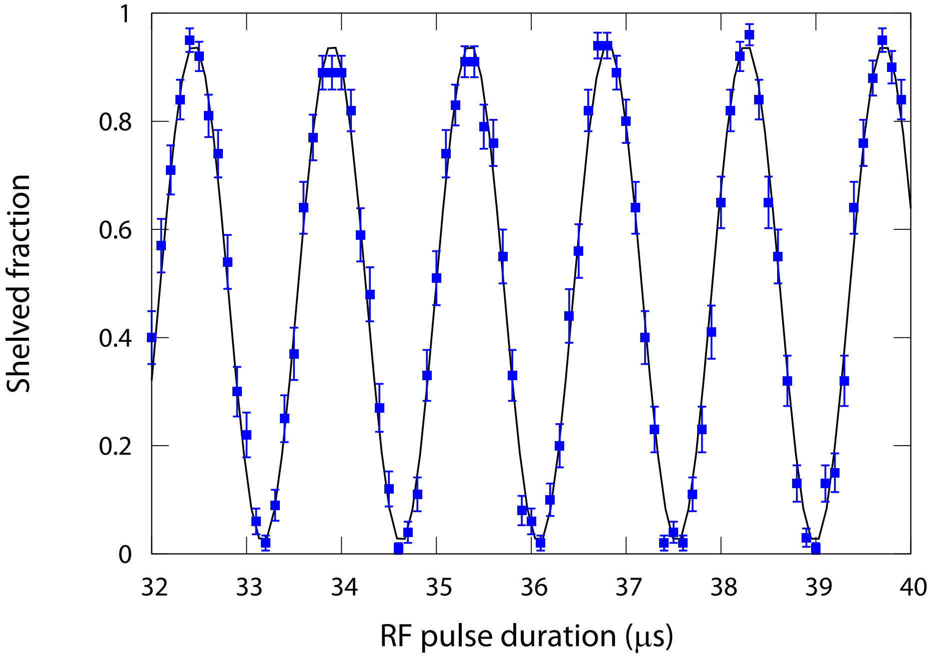

Figure 8.3: Rabi oscillation between the ground Zeeman sublevels. After initialization to a single Zeeman sublevel of the ground state, 50 W of rf is applied to a dedicated wire near the trap driving transitions between ground states in about 600 ns.

The weak excitation pulse is created by sending a brief pulse of rf to the switching AOM in the optical pumping beamline. Gating the PMT detection window is essential for minimizing the occurence of false positive detection events due to scattered room light and

---

[3] To drive ground state transitions an amplified rf voltage is dropped over a 50 ohm rf resistor outside the trap chamber, the resulting current flows through the dedicated wire near the trap to ground. The wire is made of stainless steel and so has a reasonably large resistance on the order of an ohm at dc and a bit higher at rf since the skin depth is only ten microns or so. This means that the ideal situation where only an rf magnetic field is produced is not the situation in reality where an rf electric field is also present. While the ground state splitting is chosen so that it is not near to low order motional resonances, the rf electric field will inevitably excite some motion. This hypothesis suggests that in the future the dedicated spin flip electrode should be made out of a lower resistance material like copper.

PMT dark counts. Care must be taken to ensure that the gating window overlaps well with the arrival of the spontaneously emitted photons. The durations of the weak excitation pulse and the PMT gating window were optimized to maximize the measured fidelity of the entangled state, while still maintaining a reasonable experimental rate. Summing all these contributions, the total duration of the fast loop is about 60 μs corresponding to an experimental repetition rate of 17 kHz. Toward the end of this chapter I will discuss the improvements in the system that can be made, some of which will be relevant to improving this repetition rate.

Before attempting an experiment like this it is a good idea to estimate the rate of successful events to ensure that the data acquisition will be completed in a time short compared to the average duration of a graduate student career. Here the entanglement generation rate, R, depends on the experimental repetition rate, $R_{\text{rep}} = 17$ kHz, discussed above and the probability that we will detect the photon that our ion spontaneously emits. This probability is composed of several factors. First, the excitation probability, P_{excite}, is set to about 0.2 to limit the chance of double excitations, which will diminish the entangled state fidelity. The $6P_{1/2}$ level has a branching ratio of $f \approx 0.75$ for decay to the ground states. We collect about $\frac{\Delta\Omega}{4\pi} \approx 0.02$ of the total solid angle of emission with our imaging optics. The transmission through our imaging optics is about $T \approx 0.3$, which includes a 493 nm interference filter with roughly 50% transmission and a microscope objective with just under 90% transmission. The quantum efficiency of the PMTs is $\eta \approx 0.2$ and finally $f_{\text{gate}} \approx 0.8$ of the spontaneously emitted photons are emitted within the 20 ns PMT gate window. Putting this all together, we expect an entanglement rate of

$$\begin{aligned} R_{\text{ion,photon}} &= R_{\text{rep}} \times P_{\text{success}} \\ &= R_{\text{rep}} \times P_{\text{excite}} \times f \times \tfrac{\Delta\Omega}{4\pi} \times T \times \eta \times f_{\text{gate}} \\ &= (17\text{ kHz})\,(0.2)\,(0.75)(0.02)(0.3)(0.2)\,(0.8) = 2.5\text{ Hz}. \end{aligned} \tag{8.9}$$

This expected rate suggested that the data acquisition would certainly be feasible and turned out to agree well with the entanglement rate we observe.

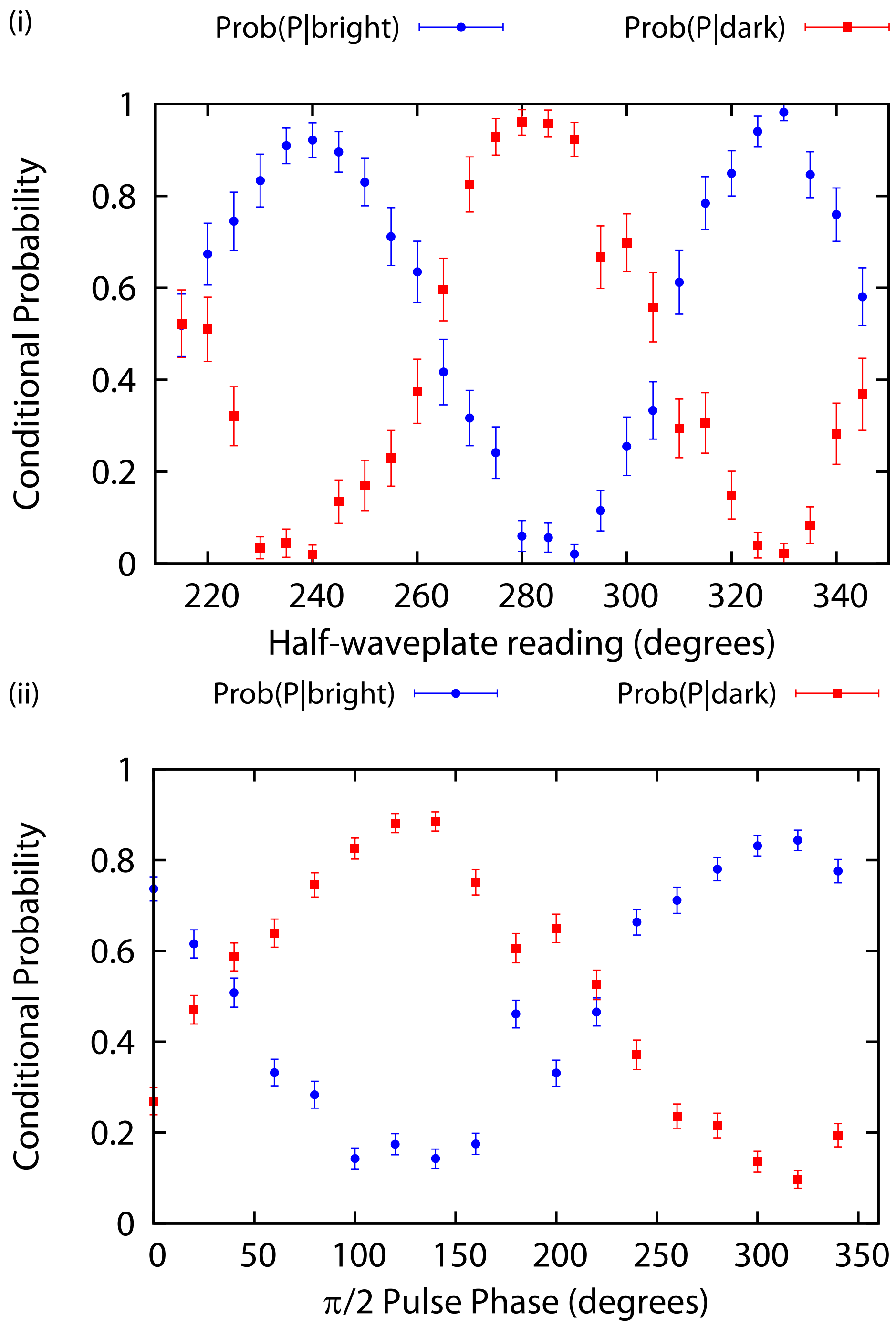

Figure 8.4: Calibration measurement data necessary for ion-photon entanglement verification. (i) The upper plot shows the conditional probability that the photon was measured to have P polarization given each possible measured ion state as a function of the photon measurement basis rotation when no rotation was applied to the ion basis. This data allows us to read off the $\lambda/2$ wave plate settings that give maximum ion-photon state correlation. (ii) The lower plot shows correlation data taken with the $\lambda/2$ set to 307 degrees (corresponding to a $\pi/2$ photon rotation) as a function of the phase an applied $\pi/2$ ion rotation. This data allows us to read off the applied rf phase that corresponds to a zero relative phase between the ion and photon measurement basis rotations.

Now that we know the measurements we must make and have an idea of the experimental cycle that will make those measurements possible, it is time to discuss the results. Since we do not know initially the precise alignment of the $\lambda/2$ wave plate fast axis with the quantization axis of the ion, nor the relative alignment of the polarizing beamsplitter, we must calibrate by measuring the ion-photon correlations as a function of the $\lambda/2$ rotation angle. In order to do this we perform the experimental procedure outlined above (with no rotation applied to the ion measurement basis) until we have detected 100 entanglement events at a given $\lambda/2$ setting, then we vary the setting and repeat until we have traced out a full oscillation in the correlations. The data acquired by this procedure is shown in the top plot of Fig. 8.4, which shows two related correlations: the probability that the polarization state of the photon was measured to be P given that the ion was bright and the probability to measure P polarization given that the ion state was dark. This data allows us to see what $\lambda/2$ wave plate settings correspond to maximum ion-photon state correlation. We chose to use a setting of 285 degrees to define the initial photon measurement basis for entanglement verification so we acquired data at that setting until we detected a total of 1000 entanglement events for better statistics. From that data we can extract all the diagonal entries in the unrotated ion-photon density matrix.

To complete the entanglement verification we need to measure the populations in the ion-photon density matrix following a rotation of both qubits by $\pi/2$. To this end we changed the $\lambda/2$ wave plate setting to 307 degrees[4] and looked at the ion-photon state correlations as a function of the phase, ϕ_{ion}, of a $\pi/2$ ground state rotation of the ion. To maximize the correlations the relative phase of the photon and ion rotations must be an integer multiple of π. This relative phase is given by $\phi = \delta t + \phi_{\text{ion}}$, where δ is the ground state splitting of 6.82 MHz and t is the time delay between the emission of the photon and the application of the ion ground state rotation. The experiment is carefully clocked so that the time between the weak excitation pulse and the ion rotation is held constant to

---

[4] You may be surprised that this number wasn't $285 + 22.5 = 307.5$ but if you look carefully at the data in Fig. 8.4 you will notice that the fast and slow axes of the $\lambda/2$ wave plate are not quite orthogonal. Judging by other wave plates in the lab, this fact is not unusual. The 307 degree setting was chosen by fitting Fig. 8.4 and rounding the resulting value to the nearest half degree, since that is the best precision reliably reproduced by the optomechanics.

better than 1 ns. However, since the weak excitation pulse is longer in duration than the excited state lifetime, the photon emission time is not fully constrained. Therefore, there will be an effective jitter in t equal to the 20 ns duration of the weak excitation. As we saw in Chapter 7, we have magnetic field fluctuations on the order of ten kilohertz over the period of the ac power line. For the obvious reason that a 120 Hz repetition rate is unacceptable for this experiment, we are unable to use a line trigger here. Thus δ suffers fluctuations of ± 4 kHz. For the purposes of the constancy of δt this fluctuation is unimportant, but it is not negligible when considering the fidelity of the $\pi/2$ rotation effected by the rf field, which here has a Rabi frequency of only 28 kHz. More on this point later, for now it is sufficient to say that, to the extent that δt may be considered a constant, the relative phase can be controlled by varying the phase of the applied rf. This is acheived by use of a direct digital synthesizer (DDS) as the oscillator providing the rf that will drive the ground state rotations. The lower plot in Fig. 8.4 shows the result, where again the probability of detecting P polarized photons given the measured ion state is shown as a function of the phase of the ion $\pi/2$ rotation. 500 entanglement events were detected at each phase, followed by an additional 1500 events at the phase corresponding to maximum correlation for better statistics on the entanglement fidelity bound. From this data we can extract the diagonal entries in the rotated ion-photon density matrix and so are able to put bounds on the entanglement fidelity as calculated by Eqs. 8.8 and 8.6. The maximal measured correlations were $P(\mathrm{P}|\mathrm{bright})=0.05(1)$, $P(\mathrm{P}|\mathrm{dark})=0.95(1)$, $P(\mathrm{S}|\mathrm{bright})=0.97(1)$, and $P(\mathrm{S}|\mathrm{dark})=0.03(1)$ for the unrotated bases and $P(\mathrm{P}|\mathrm{bright})=0.12(1)$, $P(\mathrm{P}|\mathrm{dark})=0.88(1)$, $P(\mathrm{S}|\mathrm{bright})=0.88(1)$, and $P(\mathrm{S}|\mathrm{dark})=0.12(1)$ for the rotated bases where the quoted errors are statistical. The correlations in the rotated basis are weaker due to the effective timing jitter and magnetic field fluctuations as mentioned above. These correlation measurements allow us to bound the entanglement fidelity

$$0.84(1) \leq F \leq 0.96(1), \tag{8.10}$$

which exceeds the limit of $F > 0.5$ for bipartite entanglement by many standard deviations [58].

Chapter 3 discussed the CHSH Bell signal in general terms, but the application to our system is quite direct since both the ion and photon qubits can be considered as pseudo-spins. For reference, here is Eq. 3.8 again

$$S(a, a', b, b') \equiv \left|P(a, b) - P(a, b')\right| + P(a', b) + P(a', b') \leq 2. \tag{8.11}$$

So in order to measure the CHSH Bell signal we simply need to measure ion-photon state correlations given a variety of different measurement bases. As noted in Chapter 3, for our Bell state, maximal violation of the CHSH inequality occurs for measurement basis rotations of $\{a, a', b, b'\} = \{0, \pi/2, \pi/4, 3\pi/4\}$ (with a relative phase of zero). From the data in Fig. 8.4 we know how to set the relative phase of the qubit rotations to zero, so we must set the correct apparatus parameters and measure the correlations. To ensure that nothing unexpected would happen we measured the CHSH inequality in two ways, first using rotations a and a' for the ion and then swapping to use those settings for the photon measurement. At each set of parameters we detected 2000 entanglement events, giving us a CHSH Bell signal of S=2.293(36) for the first case and S=2.303(36) for the second, where again the errors are statistical. We find that our system exceeds the classically allowed CHSH Bell signal of 2 by more than eight standard deviations. The CHSH measurements are summarized in Table 8.1.

A variety of experimental imperfections reduce the measured entanglement fidelity and CHSH Bell signal from their ideal values. Table 8.2 appears at the end of the chapter and contains a list of the known issues along with estimates of the fractional reduction in the signals that they produce and suggestions for how they will be mitigated by intended improvements to future experiments.

8.1 Conclusions and outlook

Now that we have demonstrated that we have produced an entangled ion-photon state and can use it to show violation of the CHSH inequality, let's look forward to the future prospects of this project. The goal of this research is to use entanglement swapping to produce a remotely entangled pair of $^{138}\text{Ba}^{+}$ from a pair of ion-photon entanglements like that demonstrated here by doing a partial Bell state measurement on the photons. If the ions are separated by a sufficient distance it should be possible to close both loopholes to

θ_{ion}	θ_{photon}	$P(\theta_{ion}, \theta_{photon})$
0	$\frac{\pi}{4}$	0.549
0	$\frac{3\pi}{4}$	-0.607
$\frac{\pi}{2}$	$\frac{\pi}{4}$	0.621
$\frac{\pi}{2}$	$\frac{3\pi}{4}$	0.516
	$S = 2.293 \pm 0.036$	
$\frac{\pi}{4}$	0	0.654
$\frac{3\pi}{4}$	0	-0.579
$\frac{\pi}{4}$	$\frac{\pi}{2}$	0.542
$\frac{3\pi}{4}$	$\frac{\pi}{2}$	0.528
	$S = 2.303 \pm 0.036$	

Table 8.1: Correlation function measurements and calculated Bell Signals.

Bell inequality violation experiments simultaneously. The loopholes and the proposal [61] to close them in such an experiment were outlined at the end of Chapter 3. Here I will discuss the feasibility of performing the experiment with our system.

There are two major considerations in determining the feasibility of the long-distance remote ion-ion entanglement based loophole free Bell inequality violation experiment: that the entanglement generation rate be sufficiently high that data acquisition can reasonably be completed and that sufficiently high-fidelity detection can be performed within the time constraint imposed by the locality loophole. The remote ion-ion entanglement experiment will consist of two high collection efficiency "tack" ion traps [13] separated by roughly 1 km. The fluorescence from each ion trap will be fiber coupled and brought via an estimated 1.5 km of optical fiber to an intermediate location (probably next to one of the traps for convenience) where the spontaneously emitted photon pairs will be submitted to an apparatus that detects the photonic anti-symmetric Bell state (referred to as a Bell state analyzer). The detection of such a two-photon state will collapse the ions into a singlet-like state. Some short time after the Bell state detection, we perform measurement on each ion in a randomly selected basis. Given a favorable conclusion to the feasibility estimates that follow, this procedure should allow us to verify the violation of the CHSH Bell inequality with both loopholes closed.

First let us consider the remote ion-ion entanglement rate. This consideration will contain many of the same factors as the ion-photon entanglement rate estimation discussed earlier in this chapter. The experimental fast loop will consist of: Doppler cooling (5-10 μs), ion state initialization (3 μs), ultrafast pulsed excitation (negligible), emitted photon propagation time (5 μs), Bell state analysis of the emitted photons (negligible), propagation of a synchronization signal after the Bell state analysis (5 μs). This implies that the repetition rate will be something like 50 kHz. The probability that we see a coincidence detection at the photon Bell state analyzer (heralding that the ions are in a singlet-like entangled state) depends on the ion excitation probability ($P_{\text{excite}} \sim 1$), branching ratio for decay to the ground state ($f = 0.75$), solid angle of light collection ($\frac{\Delta\Omega}{4\pi} \approx 0.4$), transmission through imaging optics ($T \approx 0.8$), fluorescence fiber coupling efficiency ($\xi \approx 0.8$), transmission of one photon over ~1.5 km of optical fiber ($T_{\text{fiber}} \approx 10^{-3*1.5}$), probability for the photons to be in the Bell state that will yield a coincidence detection ($P_{\Psi^-} = 0.25$), and the photon detection quantum efficiency ($\eta \approx 0.6$). Most of these factors enter twice since they must simultaneously be successful for both ions, with the notable exception of the fiber transmission. The 40% solid angle of light collection has been demonstrated in the "tack" parabolic mirror trap in our group [13]. The transmission through the imaging optics has been improved through the acquisition of a more efficient interference filter. The estimated fiber coupling efficiency is based on results for a similar system in the Monroe group in Maryland. The optical fiber transmission assumes the (hopefully) worst case scenario that we must lay 1.5 km of fiber to connect traps situated 1 km apart and a fiber loss of 30 dB/km. The quoted photon detection quantum efficiency assumes the use of APDs rather than PMTs. Putting all of these factors together, the remote ion-ion entanglement rate should realistically be

$$\begin{aligned} R_{\text{ion,ion}} &= R_{\text{rep}} \times P_{\Psi^-} \times T_{\text{fiber}} \Big[P_{\text{excite}} \times f \times \tfrac{\Delta\Omega}{4\pi} \times T \times \xi \times \eta \Big]^2 \\ &= (50\text{kHz})(0.25)(10^{-3*1.5}) \Big[(1)(0.75)(0.4)(0.8)(0.8)(0.6) \Big]^2 \approx 20 \text{ events/hour.} \end{aligned} \tag{8.12}$$

The fact that this experiment must only be performed once to fulfill its function makes this rate sufficient, if still somewhat painful for the graduate student(s) involved, to make the loophole free Bell inequality violation test feasible.

The second consideration is whether sufficiently high-fidelity detection can be performed within the time it takes for light to travel between the distant ion traps. Assuming that the ion traps are located 1 km apart (as the neutrino flies), detection must be completed within roughly 3 μs. For the loophole free test, ion state detection in our system consists of four steps. First, randomly choose the basis in which the ion state will be measured. This choice starts the clock for closing the locality loophole. Second, rotate to the chosen basis. As seen in Fig. 8.3, the largest rotation required by the CHSH test, $3\pi/4$, can be completed in less than half a microsecond. Third, one of the ground states must be transferred to the shelved state. This is currently performed using about one milliwatt of light at 1.76 μm, from which the shortest π-time we have achieved is 5 μs as shown in Fig. 8.1. It seems unlikely that the necessary π-time of one microsecond or so can be achieved given the available laser power. A trio of solutions present themselves. First and most simply, one could acquire a higher power laser source at 1.76 μm. Second, the laser we have could be amplified using a fiber amplifier or diode. Third, the shelving transition could be driven by a Raman process as in [14]. Given any of these choices the shelving transition can likely be driven in under one microsecond. This leaves about two microseconds for the final ion state detection step: fluorescence detection. The upper limit on the fluorescence detection rate is $R_{\text{fluor,max}} = \frac{\Gamma}{2} \times f \times \frac{\Delta\Omega}{4\pi} \times T \times \eta$, where $\Gamma = 1/\tau$ and $\tau = 8$ ns is the $6P_{1/2}$ lifetime and the other symbols have been defined previously. Numerically this corresponds to a limit of nine photons per microsecond. If we can detect just three photons on average during the roughly two microseconds we have for fluorescence detection (a factor of six below the ideal limit), we will have a detection fidelity of about 0.95 and will easily beat the detection loophole for the expected infidelity in the ion-ion entangled state. There is no doubt that the loophole free Bell test will be challenging to achieve in this (or any) system, but given these considerations it seems to be within the realm of plausibility.

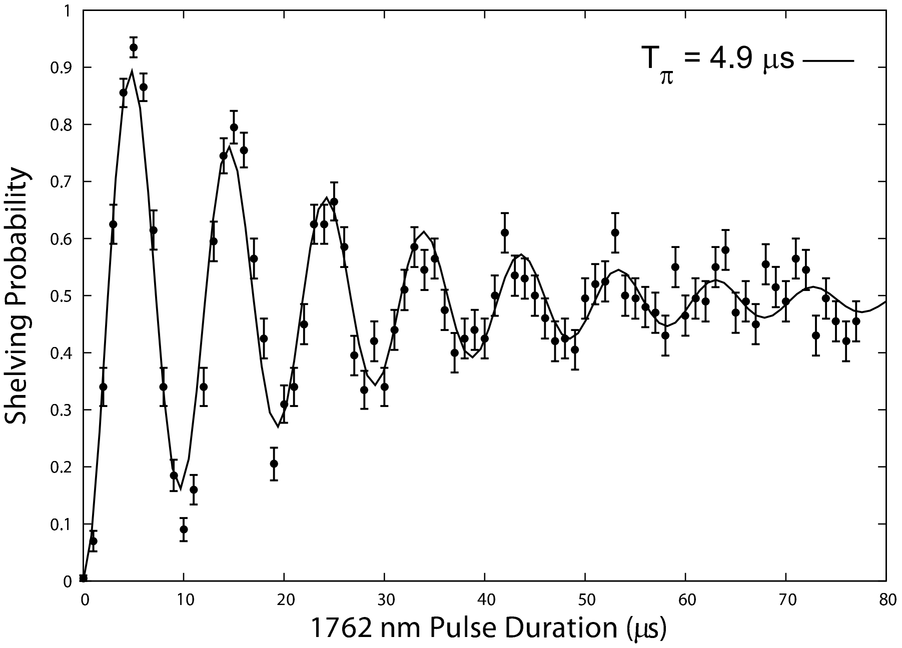

Figure 8.5: Rabi oscillation on the 1.76 μm transition with an optimized π-time of 5 μs. Care was taken to minimize the π-time given the available laser power, though tuning the laser polarization and aligning the focus on to the ion. The fit is to the ion temperature model discussed in Chapter 5 and suggests an $\bar{n}$ of about one hundred. Since the axial frequency at the time was only 340 kHz this corresponds to an ion temperature of roughly 2 mK. With the laser addressing the ion along the radial direction (which has a much higher motional frequency and therefore smaller associated Lamb-Dicke parameter) the transfer efficiency can approach unity at this ion temperature.

Error type	Error	Description	Fix
Multiple excitations	.05	Due to the (relatively) long duration of the weak excitation pulse. If we detect the first of the two spontaneously emitted photons, then the resulting ion ground state may not match the expectation.	Future experiments should employ picosecond pulses of sufficient intensity to transfer all ion population to the excited state.
Timing jitter	.03	Photons may be emitted at any time during the 20 ns PMT gate window, leading to an effective phase jitter in the application of the ion qubit rotation.	Using picosecond pulses for ion excitation.
Polarization mixing	.005	Only precisely perpendicular to the quantization axis are π and σ polarizations orthogonal. Non-zero solid angle of light collection introduces error.	Use σ^+ and σ^- polarizations along the quantization axis where the mode of the π polarization will cause it to be rejected by the optical fiber.
Background PMT counts	.04	Largely due to PMT dark counts rather than true background	Ion-ion entanglement experiment relies on coincident detection on a pair of PMTs
Imperfect PBS and wave plate	.04	Melles Griot polarizing beam cube has very pure transmitted polarization, but reflected output is less pure	No PBS necessary in ion-ion experiment
Magnetic field fluctuation	.06	60 Hz magnetic field from ac line reduces fidelity of the ion rotations	Using lower resistance wire for ground state rotation rf will allow using larger power without heating the ion. The increased Rabi frequency will greatly reduce sensitivity to magnetic field fluctuations.

Table 8.2: Experimental imperfections reducing the fidelity of the entangled ion-photon state.

Appendices

Appendix 1

CAVITY TEMPERATURE CONTROL

My first task in the lab was to design a temperature control circuit for stabilizing the temperature of the optical cavities we intended to use for frequency stabilization of our lasers. Typically we use $1''$ OD, $0.5''$ ID tubes of super invar as spacers for our optical cavities. Super invar 32-5 is an austenitic alloy of iron containing roughly 32% nickel and 5% cobalt [68]. It is optimized to have a low coefficient of thermal expansion in a temperature range around room temperature. Various sources will quote its coefficient of thermal expansion at $\alpha \approx .5 - 2$ ppm/°C. The magnitude of the frequency drift, δf of the cavity is related to the length drift, δL of the spacer (assuming the mirrors are rigidly attached to the spacer) due to a temperature drift, δT, by

$$\frac{\delta f}{f} = \frac{\delta L}{L} = \alpha\, \delta T, \tag{A.1}$$

where f is the laser frequency and L is the nominal cavity length. Therefore, if we want to limit the laser frequency drift to 1 MHz, we must limit the temperature drift to $\sim$1MHz/(500THz $\times\, 10^{-6}$/°C) = 2 mK.

To achieve this level of stability, we place a 10 kΩ thermistor with $\beta = 3950$ in a pocket in the middle of the spacer so that we can read out spacer temperature and apply feedback. Our temperature feedback is provided by applying a current to $\sim$10 Ω of resistive wire wrapped uniformly around the spacer. Since we can only heat using the wire, we must rely on dissipation of heat to the environment for cooling. This means that we must stabilize our cavities several degrees above room temperature. The cavity mirrors are epoxied to the spacer and then Torr Seal® is applied to ensure that the inner volume is not subject to the pressure changes in the room. This whole assembly is then packed in thermal insulation. The circuit shown in Fig. A.1 reads in the thermistor voltage and generates the feedback for the resistive heater. It is largely based on a design in [20], which in turn is largely based on a design in [32]. The schematic and corresponding board layout can be found on the computer named Barium9. An example of the performance of the temperature controller is shown in Fig. 5.1 in Chapter 5.

All inputs and outputs to the circuit are made through a nine pin DB connector. A stable reference voltage is provided by an AD420. This reference voltage is dropped both over a temperature set point potentiometer and a voltage divider consisting of the thermistor and a reference resistor with a low thermal coefficient. The resulting set point voltage and thermistor divider voltage are compared by an AD620 instrumentation amplifier with variable gain. The output from the AD620 passes through a proportional and integral gain stage and ultimately determines the current that flows through the heater. Note that, despite the use of a Wheatstone bridge configuration for comparing the set point and the thermistor voltage it is still important to use a very stable voltage reference since the the voltage across the thermistor shouldn't be allowed to change independently from real temperature variation. This is because the thermistor will resistively dissipate heat and even though this amount of heat is small, it is being deposited directly on the thermally sensitive element.

The board layout and IC package choices were informed by the idea that it might be useful to regulate the temperature of the critical components of the temperature controller itself. Thus the reference resistor, the AD420, and the AD620 are all surface mount components localized to one area of the board which has only bare ground plane on the backside. This would make it relatively easy to mount a Peltier and stabilize the temperature of the board against changes in the room temperature.

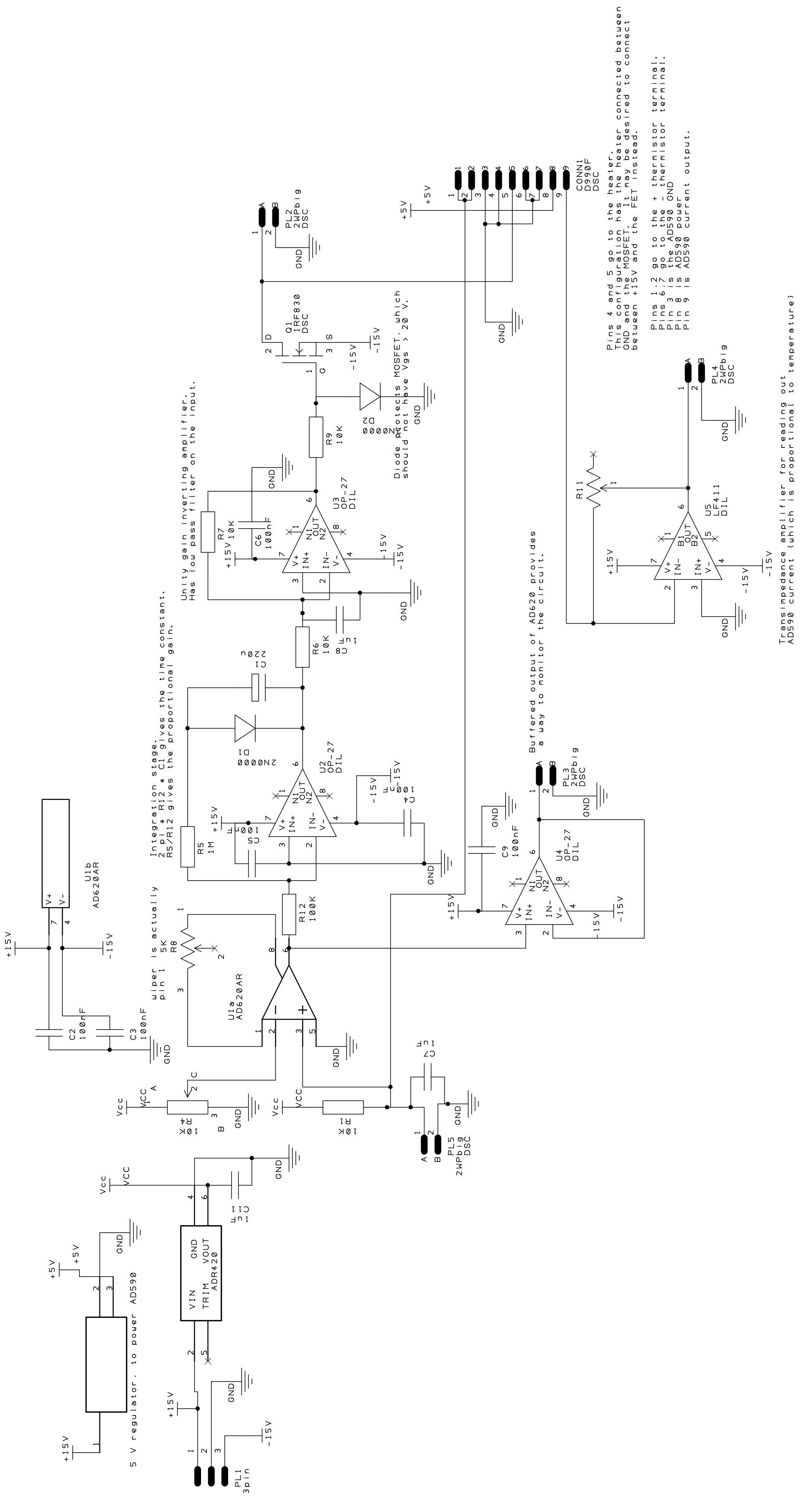

Figure A.1: Schematic of a temperature control circuit for cavity stabilization.

Appendix 2

LASER FREQUENCY STABILIZATION

Laser frequency stabilization is a ubiquitous task in modern atomic physics. Here we are primarily interested in stabilizing drifts in the frequency of the diode lasers used for Doppler cooling and neutral barium ionization, tasks for which the laser linewidth need not be particularly narrow. To this end we prepared a set of super invar spaced temperature stabilized (see Appendix A) optical cavities to use as frequency references. Typically we use cavities of fairly low finesse ($\mathcal{F} \sim 100$) since short timescale linewidth narrowing is not our goal. Fig. B.1 shows a block diagram of the laser locking system. When I joined the lab, first attempts at making such a system were under way. The first solution (for the part of the system inside the blue dashed line) consisted of a set of five separate pieces of electronics. Two were homebuilt: the transimpedance amplifier for the photodiode and the PI box that generated feedback based on the error signal. The oscillator was an HP function generator, several other elements were contained in a lock-in amplifier, and the frequency modulated rf for the AOM was produced by an HP8640 signal generator. My idea was to replace these five (somewhat expensive) boxes by a single inexpensive one.

What follows is an overview of the laser locking system. Usually a wedged partial reflector is placed in the output of the diode laser, one reflection is sent to a wavemeter for frequency monitoring and the other is the path shown in Fig. B.1 that goes to a cavity for frequency stabilization. This path passes through a double-passed AOM which is being driven by a signal from the frequency lock box that is the subject of this appendix. The AOM fulfills two purposes, first, it places a variable frequency shift on to the laser and second it applies the frequency modulation signal that the lock box will use to create its error signal[1]. The frequency modulated and shifted laser beam is the sent through an

---

[1] Typically the useful bandwidth of a 200 MHz center frequency AOM is about 50 MHz. Since the AOM is double-passed we get twice this bandwidth in laser tunability, and, what is more, the output direction of the frequency shifted beam has very little dependence on the frequency shift so the laser can be smoothly

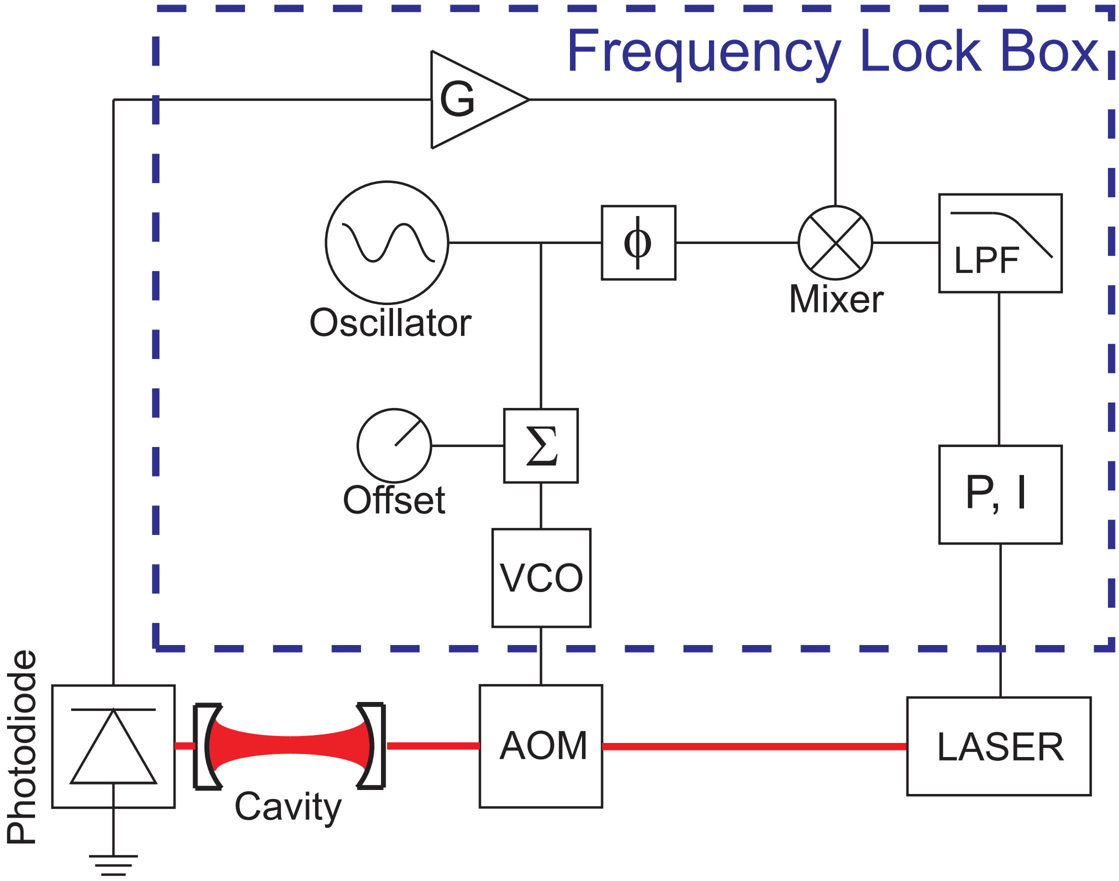

Figure B.1: Block diagram of the cavity transmission laser frequency locking system.

optical cavity and on to a photodiode. The photodiode must be sufficiently fast to track the modulation signal at 20 kHz, not particularly challenging, but something to keep in mind.

From here the discussion of the laser locking system centers on what happens inside of the blue dashed box that indicates the contents of the frequency lock box of my design. The signal from the photodiode is applied to a set discrete, switchable inverting gain stages with amplification factors of 3, 10, and 100. This amplified signal is sent into one of the input ports of an AD633 analog multiplier chip. The other input port of the multiplier receives a local oscillator signal created by an ICL8038 chip that has been passed through

---

tuned while remaining mode-matched to the cavity downstream.

a set of phase shifting stages to allow full 2π control of the oscillator phase. Since the laser has been frequency modulated by the same oscillator signal, there will be a laser frequency dependent signal at the oscillator frequency on the photodiode signal. This means that the mixer will have output components at dc and at twice the frequency of the local oscillator. A pair of switchable single pole RC low pass filters leave only the dc component which is the error signal, for reasons we will discuss shortly. The error signal is passed to a circuit with proportional and integral gain and finally the feedback generated in this way is sent to the piezoelectric transducer attached to the external cavity of the diode laser. The last function of the frequency lock box is to generate the signal that drives the AOM. For this purpose a variably attenuated fraction of the local oscillator is split and summed with a variable dc voltage derived from a stable voltage reference. The sum is sent to a Minicircuits VCO, which generates a frequency modulated rf signal that is subsequently amplified (not shown) and sent to the AOM.

Now we should address the question of why such a system will produce a useful error signal. Fig. B.2 attempts to explain the answer to this question diagrammatically. It shows how the amplitude modulation of the cavity output intensity is related to the laser frequency modulation at three different laser center frequencies: red detuned by roughly a half cavity linewidth, resonant, and blue detuned by roughly a half cavity linewidth. The important point to notice is that the phases of the amplitude modulation when the laser is red vs. blue detuned are different by π, while the frequency of the amplitude modulation becomes dominantly twice that of the local oscillator when the laser is resonant with the cavity. Thus, if we set the phase of the local oscillator input to the analog multiplier to match the phase of the amplitude modulation when the laser is red detuned, the output of the multiplier will contain a dc component proportional to the green dashed error signal curve, as well as signals at the local oscillator frequency and its harmonics. After the low pass filter removes these ac components we are left with a useful error signal that will tell the diode laser's piezo to increase the laser frequency when its frequency has fallen below the cavity resonance and to decrease the laser frequency when it drifts above [47].

The complete schematic of the circuit as well as the board layout can be found on the computer named Barium9. Some technical notes about the usage of the circuit can be found in the first pages of the first MUSIQC lab notebook.

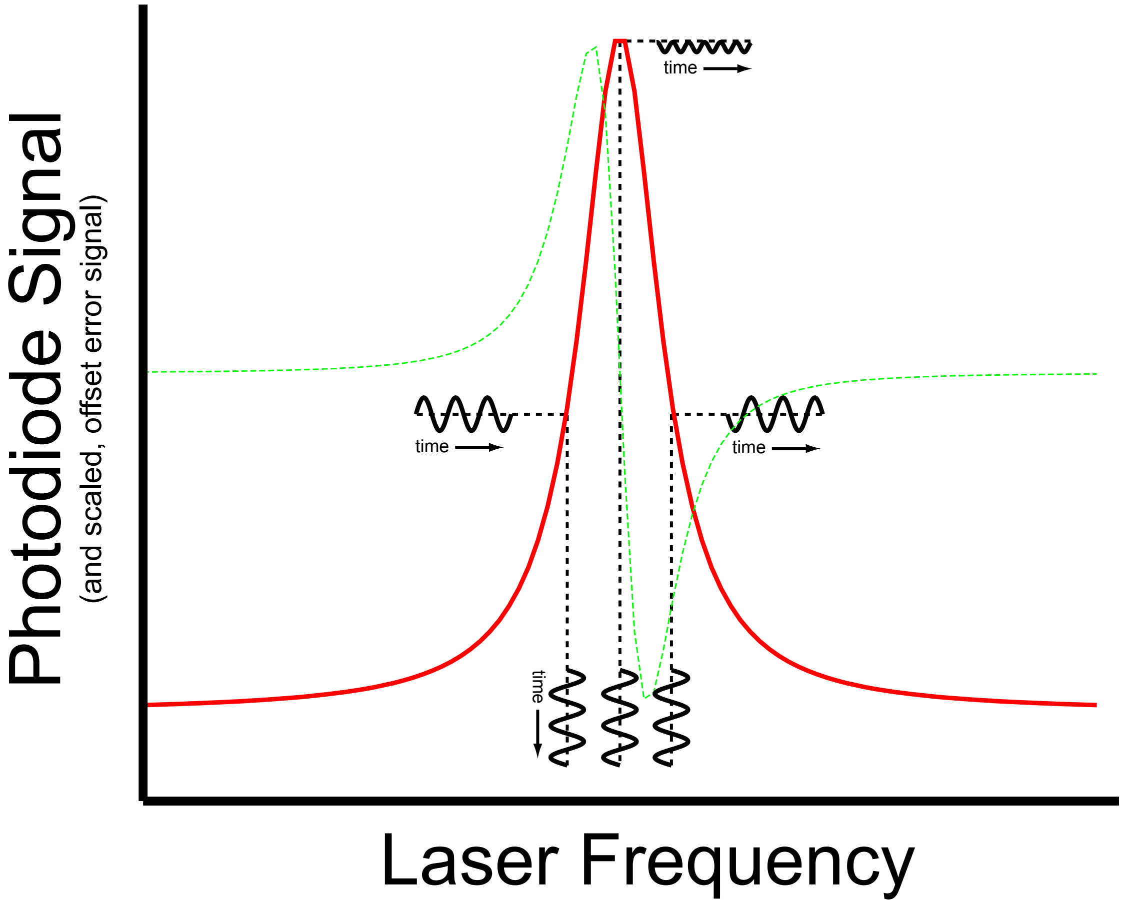

Figure B.2: Diagrammatic representation of the production of the error signal by the laser frequency locking system. When the laser frequency is on opposite slopes of the cavity resonance the amplitude modulation of the photodiode signal resulting from the laser frequency modulation has the opposite phase. When the laser is resonant with the cavity the amplitude modulation has twice the frequency of the frequency modulation. After applying phase sensitive detection to the photodiode signal, an error signal proportional to the green dashed curve is produced. Note that the error signal in the figure has an offset to make it fit nicely on the plot, in reality the zero level of the error signal corresponds to its value when the laser is resonant with the cavity (which is the same as the value approached as the laser is far off resonant with the cavity).

BIBLIOGRAPHY

[1] L Allen and JH Eberly. *Optical Resonance, Two-Level Atoms.* Dover, New York, 1975.

[2] Markus Ansmann, H. Wang, Radoslaw C. Bialczak, Max Hofheinz, Erik Lucero, M. Neeley, A. D. O'Connell, D. Sank, M. Weides, J. Wenner, A. N. Cleland, and John M. Martinis. Violation of bell's inequality in josephson phase qubits. *Nature*, 461:504–506, Sep 2009.

[3] Alain Aspect, Jean Dalibard, and Gérard Roger. Experimental test of bell's inequalities using time- varying analyzers. *Phys. Rev. Lett.*, 49:1804–1807, Dec 1982.

[4] Carolyn Auchter, Chen-Kuan Chou, Thomas W. Noel, and Boris B. Blinov. Ion photon entanglement and bell inequality violation with 138ba+. *J. Opt. Soc. Am. B*, 31(7):1568–1572, Jul 2014.

[5] J. S. Bell. On the einstein podolsky rosen paradox. *Physics*, 1(3):195, Nov 1964.

[6] Michael J. Biercuk, Hermann Uys, Aaron P. Vandevender, Nobuyasu Shiga, Wayne M. Itano, and John J. Bollinger. High-fidelity quantum control using ion crystals in a penning trap. *Quantum Info. Comput.*, 9(11):920–949, November 2009.

[7] R. Blatt and G. Werth. Precision determination of the ground-state hyperfine splitting in $^{137}\mathrm{Ba}^{+}$ using the ion-storage technique. *Phys. Rev. A*, 25:1476–1482, Mar 1982.

[8] Albert Bramon and Marek Nowakowski. Bell inequalities for entangled pairs of neutral kaons. *Phys. Rev. Lett.*, 83:1–5, Jul 1999.

[9] Joseph W. Britton, Brian C. Sawyer, Adam C. Keith, C.-C. Joseph Wang, James K. Freericks, Hermann Uys, Michael J. Biercuk, and John J. Bollinger. Engineered two-dimensional ising interactions in a trapped-ion quantum simulator with hundreds of spins. *Nature*, 484:489–492, 2012.

[10] Lowell S. Brown and Gerald Gabrielse. Geonium theory: Physics of a single electron or ion in a penning trap. *Rev. Mod. Phys.*, 58:233–311, Jan 1986.

[11] Nicolas Brunner, Daniel Cavalcanti, Stefano Pironio, Valerio Scarani, and Stephanie Wehner. Bell nonlocality. *Rev. Mod. Phys.*, 86:419–478, Apr 2014.

[12] D. D. Caussyn, Ya. S. Derbenev, T. J. P. Ellison, S. Y. Lee, T. Rinckel, P. Schwandt, F. Sperisen, E. J. Stephenson, B. von Przewoski, B. B. Blinov, C. M. Chu, E. D. Courant, D. A. Crandell, W. A. Kaufman, A. D. Krisch, T. S. Nurushev, R. A. Phelps, L. G. Ratner, V. K. Wong, and C. Ohmori. Spin flipping a stored polarized proton beam. *Phys. Rev. Lett.*, 73(21):2857–2859, Nov 1994.

[13] Chen-Kuan Chou, Gang Shu, Thomas Noel, John Wright, Richard Graham, and Boris Blinov. Trapping ions in a 2-pi parabolic mirror. *Bull. Am. Phys. Soc.*, 58:157, Jun 2013.

[14] Boon Leng Chuah, Nicholas C. Lewty, and Murray D. Barrett. State detection using coherent raman repumping and two-color raman transfers. *Phys. Rev. A*, 84:013411, Jul 2011.

[15] John F. Clauser, Michael A. Horne, Abner Shimony, and Richard A. Holt. Proposed experiment to test local hidden-variable theories. *Phys. Rev. Lett.*, 23:880–884, Oct 1969.

[16] Taunia L. L. Closson and Marc R. Roussel. The flattening phase transition in systems of trapped ions. *Canadian Journal of Chemistry*, 87(10):1425–1435, 2009, http://www.nrcresearchpress.com/doi/pdf/10.1139/V09-116.

[17] Claude Cohen-Tannoudji. *Atom-Photon Interactions: Basic Processes and Applications.* Wiley, New York, 1992.

[18] W. Demtröder. *Atoms, Molecules, and Photons.* Springer, 2006.

[19] M. R. Dietrich, N. Kurz, T. Noel, G. Shu, and B. B. Blinov. Hyperfine and optical barium ion qubits. *Phys. Rev. A*, 81(5):052328, May 2010.

[20] Matthew R. Dietrich. *Barium ions for quantum computation.* PhD thesis, University of Washington, Seattle, WA 98195, 2009.

[21] Daniel H. E. Dubin. Theory of structural phase transitions in a trapped coulomb crystal. *Phys. Rev. Lett.*, 71:2753–2756, Oct 1993.

[22] Philippe H. Eberhard. Background level and counter efficiencies required for a loophole-free einstein-podolsky-rosen experiment. *Phys. Rev. A*, 47:R747–R750, Feb 1993.

[23] A. Einstein, B. Podolsky, and N. Rosen. Can quantum-mechanical description of physical reality be considered complete? *Phys. Rev.*, 47:777–780, May 1935.

[24] Christopher J. Foot. *Atomic Physics.* Oxford University Press, New York, NY, 2005.

[25] Stuart J. Freedman and John F. Clauser. Experimental test of local hidden-variable theories. *Phys. Rev. Lett.*, 28:938–941, Apr 1972.

[26] R. Ghosh, C. K. Hong, Z. Y. Ou, and L. Mandel. Interference of two photons in parametric down conversion. *Phys. Rev. A*, 34:3962–3968, Nov 1986.

[27] D. Grischkowsky. Coherent excitation, incoherent excitation, and adiabatic states. *Phys. Rev. A*, 14(2):802–812, Aug 1976.

[28] Stephan Timo Gulde. *Experimental realization of quantum gates and the Deutsch-Jozsa algorithm with trapped* $^{40}\mathrm{Ca}^{+}$ *ions.* PhD thesis, University of Innsbruck, Innsbruck, 2003.

[29] D. Hanneke, S. Fogwell, and G. Gabrielse. New measurement of the electron magnetic moment and the fine structure constant. *Phys. Rev. Lett.*, 100:120801, Mar 2008.

[30] F. T. Hioe. Solution of bloch equations involving amplitude and frequency modulations. *Phys. Rev. A*, 30:2100–2103, Oct 1984.

[31] Matthew R. Hoffman, Thomas W. Noel, Carolyn Auchter, Anupriya Jayakumar, Spencer R. Williams, Boris B. Blinov, and E. N. Fortson. Radio-frequency-spectroscopy measurement of the Landé g_j factor of the $5D_{5/2}$ state of Ba^{+} with a single trapped ion. *Phys. Rev. A*, 88:025401, Aug 2013.

[32] Paul Horowitz and Winfield Hill. *The Art of Electronics.* Cambrdige University Press, Cambridge, UK, 1989.

[33] Hans Karlsson and Ulf Litzn. Revised ba i and ba ii wavelengths and energy levels derived by fourier transform spectroscopy. *Physica Scripta*, 60(4):321, 1999.

[34] H. Knab, K.H. Knll, F. Scheerer, and G. Werth. Experimental ground state g_j-factor of Ba^{+} in a Penning ion trap. *Zeitschrift fr Physik D Atoms, Molecules and Clusters*, 25(3):205–208, 1993.

[35] K. H. Knöll, G. Marx, K. Hübner, F. Schweikert, S. Stahl, Ch. Weber, and G. Werth. Experimental g_j factor in the metastable $5D_{3/2}$ level of Ba^{+}. *Phys. Rev. A*, 54:1199–1205, Aug 1996.

[36] N. Kurz, M. R. Dietrich, Gang Shu, T. Noel, and B. B. Blinov. Measurement of the Landé g factor of the $5D_{5/2}$ state of Ba ii with a single trapped ion. *Phys. Rev. A*, 82:030501, Sep 2010.

[37] Nathan Kurz. *Experiments in remote entanglement using single barium ions.* PhD thesis, University of Washington, Seattle, WA 98195, 2010.

[38] X. Lacour, S. Guérin, L. P. Yatsenko, N. V. Vitanov, and H. R. Jauslin. Uniform analytic description of dephasing effects in two-state transitions. *Phys. Rev. A*, 75(3):033417, Mar 2007.

[39] M. Lamehi-Rachti and W. Mittig. Quantum mechanics and hidden variables: A test of bell's inequality by the measurement of the spin correlation in low-energy proton-proton scattering. *Phys. Rev. D*, 14:2543–2555, Nov 1976.

[40] D. Leibfried, R. Blatt, C. Monroe, and D. Wineland. Quantum dynamics of single trapped ions. *Rev. Mod. Phys.*, 75:281–324, Mar 2003.

[41] Tongcang Li, Zhe-Xuan Gong, Zhang-Qi Yin, H. T. Quan, Xiaobo Yin, Peng Zhang, L.-M. Duan, and Xiang Zhang. Space-time crystals of trapped ions. *Phys. Rev. Lett.*, 109:163001, Oct 2012.

[42] Michael M. T. Loy. Observation of population inversion by optical adiabatic rapid passage. *Phys. Rev. Lett.*, 32(15):814–817, Apr 1974.

[43] A. A. Madej and J. D. Sankey. Quantum jumps and the single trapped barium ion: Determination of collisional quenching rates for the $5d_{5/2}$ level. *Phys. Rev. A*, 41:2621–2630, Mar 1990.

[44] I. Marzoli, J. I. Cirac, R. Blatt, and P. Zoller. Laser cooling of trapped three-level ions: Designing two-level systems for sideband cooling. *Phys. Rev. A*, 49:2771–2779, Apr 1994.

[45] Harold J. Metcalf and Peter van der Straten. *Laser Cooling and Trapping.* Springer, 2001.

[46] D. L. Moehring, M. J. Madsen, B. B. Blinov, and C. Monroe. Experimental bell inequality violation with an atom and a photon. *Phys. Rev. Lett.*, 93:090410, Aug 2004.

[47] Warren Nagourney. *Quantum Electronics for Atomic Physics.* Oxford University Press, New York, 2010.

[48] W Neuhauser, M Hohenstatt, P Toschek, and H Dehmelt. Optical-sideband cooling of visible atom cloud confined in parabolic well. *Physical Review Letters*, 41(4):233–236, 1978.

[49] T. Noel, M. R. Dietrich, N. Kurz, G. Shu, J. Wright, and B. B. Blinov. Adiabatic passage in the presence of noise. *Phys. Rev. A*, 85:023401, Feb 2012.

[50] Hilmar Oberst. *Resonance fluorescence of single barium ions.* PhD thesis, Universität Innsbruck, A-6020 Innsbruck, Austria, 1999.

[51] Z. Y. Ou and L. Mandel. Violation of bell's inequality and classical probability in a two-photon correlation experiment. *Phys. Rev. Lett.*, 61:50–53, Jul 1988.

[52] W. Pfaff, B. Hensen, H. Bernien, S. B. van Dam, M. S. Blok, T. H. Taminiau, M. J. Tiggelman, R. N. Schouten, M. Markham, D. J. Twitchen, and R. Hanson. Unconditional quantum teleportation between distant solid-state quantum bits. *Science*, 2014, http://www.sciencemag.org/content/early/2014/05/28/science.1253512.full.pdf.

[53] Wolfgang Pfaff, Tim H. Taminiau, Lucio Robledo, Hannes Bernien, Matthew Markham, Daniel J. Twitchen, and Ronald Hanson. Demonstration of entanglement-by-measurement of solid-state qubits. *Nature*, 9:29–33, Jan 2013.

[54] D. Porras and J. I. Cirac. Quantum manipulation of trapped ions in two dimensional coulomb crystals. *Phys. Rev. Lett.*, 96:250501, Jun 2006.

[55] U G Poschinger, G Huber, F Ziesel, M Deiß, M Hettrich, S A Schulz, K Singer, G Poulsen, M Drewsen, R J Hendricks, and F Schmidt-Kaler. Coherent manipulation of a $^{40}\mathrm{Ca}^{+}$ spin qubit in a micro ion trap. *Journal of Physics B: Atomic, Molecular and Optical Physics*, 42(15):154013, 2009.

[56] M. G. Raizen, J. M. Gilligan, J. C. Bergquist, W. M. Itano, and D. J. Wineland. Ionic crystals in a linear paul trap. *Phys. Rev. A*, 45:6493–6501, May 1992.

[57] M. A. Rowe, D. Kielpinski, V. Meyer, C. A. Sackett, W. M. Itano, C. Monroe, and D. J. Wineland. Experimental violation of a bell's inequality with efficient detection. *Nature*, 409:791–794, Feb 2001.

[58] C. A. Sackett, D. Kielpinski, B. E. King, C. Langer, V. Meyer, C. J. Myatt, M. Rowe, Q. A. Turchette, W. M. Itano, D. J. Wineland, and C. Monroe. Experimental entanglement of four particles. *Nature*, 404:256, Mar 2000.

[59] Ralf Schützhold, Michael Uhlmann, Lutz Petersen, Hector Schmitz, Axel Friedenauer, and Tobias Schätz. Analogue of cosmological particle creation in an ion trap. *Phys. Rev. Lett.*, 99:201301, Nov 2007.

[60] Bruce W. Shore. *The Theory of Coherent Atomic Excitation*, volume 2. Wiley-Interscience, New York, NY, 1990.

[61] Christoph Simon and William T. M. Irvine. Robust long-distance entanglement and a loophole-free bell test with ions and photons. *Phys. Rev. Lett.*, 91:110405, Sep 2003.

[62] Nikolay V Vitanov, Thomas Halfmann, Bruce W Shore, and Klass Bergmann. Laser-induced population transfer by adiabatic passage techniques. *Ann. Rev. of Phys. Chem.*, 52:763–809, 2001.

[63] D. J. Wineland and Wayne M. Itano. Laser cooling of atoms. *Phys. Rev. A*, 20:1521–1540, Oct 1979.

[64] DJ Wineland, C Monroe, WM Itano, D Leibfried, BE King, and DM Meekhof. Experimental issues in coherent quantum-state manipulation of trapped atomic ions. *Journal of Research of the National Institute of Standards and Technology*, 103(3), 1998.

[65] Curt Wittig. The landauzener formula. *The Journal of Physical Chemistry B*, 109(17):8428–8430, 2005, http://pubs.acs.org/doi/pdf/10.1021/jp040627u. PMID: 16851989.

[66] Chr. Wunderlich, Th. Hannemann, T. Körber, H. Häffner, Ch. Roos, W. Hänsel, R. Blatt, and F. Schmidt-Kaler. Robust state preparation of a single trapped ion by adiabatic passage. *J. Mod. Opt.*, Sep 2007.

[67] N. Yu, W. Nagourney, and H. Dehmelt. Radiative lifetime measurement of the Ba^+ metastable $D_{3/2}$ state. *Phys. Rev. Lett.*, 78:4898–4901, Jun 1997.

[68] A.I. Zakharov, A.M. Perepelkina, and A.N. Shiryaeva. Effect of alloying on thermal expansion of superinvar alloy. *Metal Science and Heat Treatment*, 14(6):539–541, 1972.

[69] Clarence Zener. Non-adiabatic crossing of energy levels. *Proc. Roy. Soc. London Ser. A*, 137:pp. 696–702, 1932.

VITA

Thomas William Noel was born on September 1st, 1986 in West Allis, Wisconsin to Diane and Dale Noel. He attended the University of Wisconsin, graduating with a Bachelor of Science degree in Physics in 2009 and gained some experience in and excitement about experimental atomic physics as a research assistant in Mark Saffman's group. After a brief summer's escape from science, he joined the University of Washington as a graduate student in the Physics department. He immediately joined Boris Blinov's trapped ion quantum computing group to work on building part of the infrastructure and developing methods for the long-distance remote entanglement experiment. Five years later, he graduated. So it goes.